Phase Behavior and Structure of Binary Colloidal Mixtures

Inaugural–Dissertation
zur
Erlangung des Doktorgrades der
Mathematisch-Naturwissenschaftlichen Fakultät
der Heinrich-Heine-Universität Düsseldorf

vorgelegt von

JOACHIM DZUBIELLA

aus Sensburg

Düsseldorf, 28. Januar 2002

Gedruckt mit Genehmigung der
Mathematisch-Naturwissenschaftlichen Fakultät
der Heinrich-Heine-Universität Düsseldorf

Referent: Prof. Dr. H. Löwen
Koreferenten: HSDoz. C. N. Likos, Ph.D.
Prof. J.-P. Hansen, Ph.D.

Tag der mündlichen Prüfung: 21. Oktober 2002

©Joachim Dzubiella 2002
All Rights Reserved.

This thesis is based on the following original papers:

Chapter 2:

A. Jusufi, J. Dzubiella, C. N. Likos, C. von Ferber, and H. Löwen,
Effective interactions between star polymers and colloidal particles,
Journal of Physics: Condensed Matter **13**, 6177-6194 (2001).

Chapter 3:

J. Dzubiella, A. Jusufi, C. N. Likos, C. von Ferber, H. Löwen, J. Stellbrink, J. Allgaier,
D. Richter, A. B. Schofield, P. A. Smith, W. C. K. Poon, and P. N. Pusey,
Phase separation in star polymer-colloid mixtures,
Physical Review E **64**, 010401(R)(1-4) (2001).

J. Dzubiella, C. N. Likos, and H. Löwen,
Star-polymers as depleting agents of colloidal hard spheres,
Europhysics Letters **58**, 133-139 (2002).

J. Dzubiella, C. N. Likos, and H. Löwen,
Phase behavior of star polymer–colloid mixtures,
Journal of Chemical Physics **116**, 9518 (2002).

Chapter 4:

J. Dzubiella, G. P. Hoffmann, and H. Löwen,
Lane formation in colloidal mixtures driven by an external field,
Physical Review E **65**, 021402(1-8) (2002).

J. Dzubiella and H. Löwen,
Pattern formation in colloidal mixtures under external driving fields,
Journal of Physics: Condensed Matter, **14**, 9383-9395 (2002).

Abstract

In this work, we present recently achieved progress in the physics of binary colloidal mixtures in equilibrium and nonequilibrium. The work consists of two parts. In the first part we study a mixture of star polymers and hard spherical colloids as a model for a binary colloidal system in equilibrium. Tuning the arm number of the star polymers provides a natural bridge between the well-known borderline models of colloid-polymer and binary hard sphere mixtures. Using monomer-resolved Molecular Dynamics simulations and theoretical arguments we systematically investigate the effective interactions between hard, colloidal particles and star polymers in a good solvent. We establish analytical forms for the star-colloid interaction which are in excellent agreement with simulation results. A new expression for the star-star interaction for low functionalities is also introduced. Using these effective interactions in a full two-component description we examine the demixing transition in the fluid phase in star-polymer–colloid mixtures for different star arm numbers and star-colloid size ratios. The demixing binodals are calculated and found to be consistent with experimental observations. Further we examine the whole phase behavior of star-polymer–colloid mixtures for star-to-colloid size ratios smaller than unity and different arm numbers by canonically tracing out the star-polymers and deriving accurate effective depletion potentials between the colloids. We find stable fluid-fluid demixing transitions for low arm numbers above a critical value of the size ratio below preempted by a fcc-solid. By increasing the arm number and the size ratio, the region of stability of the demixing transition with respect to crystallization of the colloids shrinks. A comparison between the one- and two-component descriptions that demonstrates the consistency between the two routes is also carried out.

In the second part we focus on nonequilibrium phase transitions. The influence of an external field acting differently on the two constituents of a binary colloidal mixture performing Brownian dynamics is investigated by computer simulations and a simple theory. If the external forces are parallel and the field-free state is a mixed fluid, the simulations show a nonequilibrium first order phase transition involving lanes of particles of the same type which are sliding against each other in the direction of the external forces. We further show that pattern formation also occurs in a time-dependent oscillatory field. If the frequency of the external field exceeds a critical value, however, the system exhibits a transition back to the disordered state. For nonparallel forces, lane formation is also observed but with an orientation *tilted* with respect to the external forces. If the field-free state is crystalline, a continuous increase of the parallel external forces yields a novel *reentrant freezing* behavior: the crystal first melts mechanically via the external force and then recrystallizes into demixed crystalline lanes sliding against each other. Our results can be experimentally verified in binary colloidal suspensions exposed to external fields under non-equilibrium conditions.

Zusammenfassung

Die vorliegende Arbeit untersucht die Physik von binären kolloidalen Mischungen im Gleichgewicht und Nichtgleichgewicht. Ein interessantes und umfassendes Modell für binäre Systeme im Gleichgewicht ist eine Mischung aus Sternpolymeren und harten sphärischen Kolloiden. Durch Veränderung der Anzahl der Arme eines Sternpolymers ist es möglich zwischen den wohlbekannten Kolloid-Polymer und binären Hartkugel Mischungen zu interpolieren. Die effektive Wechselwirkung zwischen den Sternpolymeren und Kolloiden wird systematisch untersucht und analytische Ausdrücke eingeführt. Zusätzlich präsentieren wir ein Paarpotential für die effektive Wechselwirkung zwischen Sternpolymeren für kleine Armzahlen, welches eine leichte Modifizierung des bekannten Ausdrucks für größere Armzahlen ist. Durch Verwendung dieser Wechselwirkungen in Flüssig-Integralgleichungen wird die Entmischung der Kolloide in der fluiden Phase für verschiedene Armzahlen und Größenverhältnisse zwischen Sternen und Kolloiden untersucht. Die Koexistenzkurven werden konstruiert und zeigen quantitative Übereinstimmung mit experimentellen Messungen. Im Anschluß berechnen wir das komplette Phasendiagram von Sternpolymer-Kolloid Mischungen für einen weiten Bereich von Armzahlen und Größenverhältnissen, indem wir die Sternpolymere aus dem binären System kanonisch herausintegrieren und effektive Wechselwirkungen zwischen den Kolloiden in einem nunmehr einkomponentigen System verwenden. Für kleine Armzahlen finden wir stabile fluid-fluid Entmischungen der Kolloide ab einem kritischen Größenverhältnis. Die systematische Untersuchung der Phasendiagramme zeigt, daß die Entmischung in der fluiden Phase bei Erniedrigung des Größenverhältnisses und bei Erhöhung der Armzahl instabil gegenüber dem Einfrieren der Kolloide wird. Dies ist in Konsistenz mit den Phasendiagrammen der beiden Grenzfälle von Kolloid-Polymer und binären Hartkugel Mischungen. Ein Vergleich der zweikomponentigen und der effektiven einkomponentigen Beschreibung rechtfertigt die angewandten statistischen Methoden und Ergebnisse im Rahmen des Modells.

Als einfaches Modell für binäre kolloidale Mischungen im Nichtgleichgewicht betrachten wir Kolloide mit Yukawa-Wechselwirkung, welche einer Brownschen Dynamik unterliegen. Es wird angenommen, daß externe Felder unterschiedlich auf die beiden Konstituenten der Mischung wirken. Computersimulationen zeigen für parallele äußere Kräfte einen Nichtgleichgewichtsübergang erster Ordnung, der zu einer Strukturbildung in der Flüssigkeit führt. Teilchen gleichen Typs sammeln sich in Streifen parallel zu den äußeren Feldern und wandern kollektiv mit gleicher Driftgeschwindigkeit. Der Übergang geschieht bei genügend großer betraglicher Differenz der externen Kräfte und bei ausreichend kleiner Frequenz und wird mit Computersimulation und einfacher Theorie quantitativ untersucht. Eine experimentelle Verifizierung sind bidisperse kolloidale Systeme unter Sedimentation. Wir zeigen weiter, daß der Übergang auch bei nicht parallelen Kräften auftritt und zu ungewöhnlich verdrehten Streifen führt. Ist das kräftefreie System ein Festkörper, beobachten wir ein neuartiges *reentrant-freezing* Verhalten: bei Erhöhung der äußeren Kräfte schmilzt das System, um dann nach dem Übergang in die strukturierte Phase innerhalb der wandernden Domänen wieder einzufrieren.

Contents

Chapter 1

Introduction

Typical soft matter systems, such as polymers and colloids, almost always occur in the form of mixtures. It is the central goal of soft matter physics to offer insights into their generic phase behavior which does not depend on the detailed chemical structure of their constituents.

Multicomponent mixtures in thermodynamic equilibrium display an enormously richer phase behavior than one-component systems. A typical pure substance consisting of spherically symmetric molecules without internal degrees of freedom displays a generic phase behavior on the temperature-pressure plane that features three phases: a gaseous and a liquid one (if sufficiently strong attractions between the molecules are present) and a crystal [1]. Moreover, the Gibbs phase rule [2] asserts that there is only one point in the phase diagram at which these three can be found in simultaneous coexistence with one another. Consequently, investigations of the bulk thermodynamics of one-component systems focus on the calculation of the freezing- and liquid-gas coexistence curves, as well as on the properties in the neighborhood of the critical point associated with the latter. In multicomponent mixtures, the additional freedom provided by the flexibility of changing the concentration of any of the constituent species at will, opens up the possibility of various types of phase transitions, such as, e.g., vapor-liquid, demixing, crystallization of any of the number of the components, alloy formation etc. Thereby, new topological features in the phase diagram, including regions of multi-phase coexistence, lines of critical points and critical end points show up. It is therefore not much of a surprise that the structure and thermodynamics of multicomponent mixtures are studied in much less detail than those of pure substances.

In soft matter physics, on the other hand, mixtures are the rule, not the exception. To complicate matters even further, typical soft matter systems include components with a vast separation of length scales, a feature that makes a true, multicomponent description of real systems infeasible [3]. One possibility is to consider simple *model* mixtures: Two examples that have been intensively investigated in the recent past [4] are mixtures of hard spheres (colloids) and free, nonadsorbing chains on the one hand, and the binary hard sphere mixture (BHS) of two species with a variable size ratio on the other. The theoretical investigations of the colloid-polymer (CP) mixture have been based mostly on an *effective, one-component* description of the hard colloids, for which an additional, attractive depletion potential is introduced after the polymer has been integrated out. This is the well-known Asakura-Oosawa (AO) model [5, 6], in which the polymers are figured as penetrable spheres experiencing an additional hard-sphere (HS) interaction with the colloids. A number of theoretical investigations on the AO model [7, 8, 9, 10, 11] have revealed that the system displays a demixing transition that accompanies the freezing of the hard colloids. However, the former becomes *metastable* with respect to the latter [9] for polymer-to-colloid size ratios $q \leq q_{\rm c} \cong 0.45$. For size ratios $q > q_{\rm c}$, the system displays three phases: a colloid-poor/polymer-rich and colloid-rich/polymer-poor fluid, as well as a solid phase, in which the colloids form a fcc-crystalline arrangement with the polymers diffusing in it. However, for $q < q_{\rm c}$, a single, mixed fluid and a crystal phase exist. These findings are in semi-quantitative agreement with experimental results [12, 8, 13]. In the BHS system, the first indication of a demixing transition in the fluid phase was offered in the work of Biben and Hansen [14]. Two-component simulations [15, 16] have shown that the demixing transition in the fluid phase is either metastable with respect to crystallization or it is completely absent, depending on the size ratio [17]. We note that in all cases mentioned above, freezing refers to the large hard spheres only: the crystallization of both components and the associated formation of binary alloys takes place at size ratios close to unity and its investigation by theoretical methods is highly nontrivial [18, 19, 20].

A theoretical understanding of the (meta)stability of the demixing transition in two-component mixtures is provided by the *depletion potential* that effectively acts between the larger components of the mixture when the smaller ones are thermodynamically traced out [21]. Depletion is caused by the fact that the small components have more free space available to them when two large particles are brought close to contact than when they are far apart. The effective interactions arising in the AO model are purely attractive; in the BHS-case, correlation effects cause the depletion potential to develop also repulsive parts and an oscillatory behavior [22, 23]. Hence, free polymers are *more efficient* depleting agents for hard spheres than smaller hard spheres themselves. The procedure of tracing out the small components facilitates the theoretical studies but it is subject to two strong constraints arising from the definition of the effective interaction [21], namely: (i) the overall thermodynamics of the mixture must, evidently, remain invariant in switching from one description to the other and (ii) the correlation functions of the large component should also be the same in both descriptions.

It is desirable to consider systems that interpolate between the AO and the BHS models, in order to systematically investigate the evolution of the phase behavior as we move from one extreme case to the other. Mixtures of colloids and nonadsorbing *star polymers* in a good solvent are such a natural bridge. Star polymers are synthesized by covalently attaching f polymeric chains on a common center. In this way, hybrid particles between polymers and colloids can be constructed, which naturally bridge the gap between these two common states of soft matter. The number of arms f, also known as *functionality* of the stars, allows us to go from free chains ($f = 1, 2$) to stiff, spherical particles ($f \gg 1$) [24, 25, 26]. Effective interactions between star polymers in good [25] and Θ-solvents [27] have been recently derived and the validity of the former has been confirmed through extensive comparisons with experiments [25, 28, 29] and simulations [26, 30]. Extensions to polydisperse stars [31] as well as to many-body forces in dense star polymer solutions [32] have also been recently carried out.

One purpose of this work is to examine mixtures of colloids with star polymers of variable arm number f, which provide a natural bridge between the CP-mixture (corresponding to linear chains, $f = 1$ and $f = 2$) and to the BHS (formally $f \to \infty$). To this end, we derive depletion potentials between the colloids that, depending on f, interpolate between interactions similar as in the AO-model and the BHS-depletion interaction [22, 23]. We systematically investigate the consistency between the one- and two-component descriptions, since our starting point are the three interaction potentials acting between the two components. We trace out the phase diagrams of the mixture for various combinations of star arm numbers f and star-colloid size ratios.

Let us now review what is known about colloidal mixtures in nonequilibrium. While equilibrium bulk phase transitions are by now well understood both by computer simulations [33, 34] and by statistical theories [34, 35, 36], nonequilibrium situations may induce a much richer scenario of phase transformations. In the last years an emphasis was placed onto such transitions in driven diffusive systems, [37, 38, 39] which were extensively studied by theory and simulation within lattice and off-lattice models and constant and oscillatory fields [40, 41, 42]. In particular, models of identical particles were studied, which couple with a different sign to an external uniform field (so-called "plus and minus charge"particles) [43]. In the symmetric case where half of the particles are "plus-charge"and half of them are "minus-charge"particles, a blocking transition was obtained if the field strength exceeded a critical value. The particles then form stripes perpendicular to the field direction [44, 45, 46]. This transition has been put forward recently as a concept of panic theory applied to pedestrian zones [47]. Interestingly enough in a two-dimensional off-lattice system confined onto a strip, the blocking transition was found to be generated by increasing the temperature which is opposite to what one would expect from the equilibrium freezing transition that occurs by lowering the temperature.

In this work, we focus on another kind of nonequilibrium phase transition in such a driven diffusive off-lattice model with two particle species, which is associated to *lane formation*. Lanes are formed by bundles of particles of the same kind due to a nonequilibrium "slipstream"effect. While such a transition towards lane formation is absent in a square-lattice model with nearest-neighbor hopping and in pure one-component systems, it was recently found in off-lattice simulations of a confined two-dimensional system as a intermediate state between the disordered and the blocked state [47]. We investigate this lane formation in more detail and map a whole phase diagram as a function of the field strength and the range of the interparticle interaction. Experimental evidence for such an instability has been accumulated in sedimentation dynamics of bidisperse suspensions [48, 49, 50, 51].

As the occurrence of lane formation appears to be very general, this nonequilibrium transition could be experimentally verified in many other systems. One example are ionic conductors in an electric field [38]. Another less common example concerns pedestrian (or any other traffic) dynamics where lane formation is an intuitive phenomenon [52]. A further application which we put forward is that of mesoscopically sized *colloidal suspensions*, which perform diffusive Brownian dynamics in a molecular solvent. Colloidal samples have served as excellent model systems to detect equilibrium phase transitions such as freezing [3] or fluid-fluid phase separation [53]. They have also played a key role for experimental verification of kinetic mode-coupling-type theories describing the (nonequilibrium) kinetic glass transition [54]. Indeed, well-characterized colloidal suspensions may also be subjected to external fields resulting in nonequilibrium structure formation. The striking advantage of colloidal samples is that the external field can systematically be controlled and tailored [55]. As possible examples which realize the Brownian model used in the present study, we mention binary colloids under sedimentation, linear or oscillating shear, and charge-bidisperse colloidal mixtures in electric fields. Another possibility to control colloidal suspensions are external laser-optical or magnetic fields which couples to the different dielectric or magnetic permeabilities of the solvent and the colloid material, respectively. We further mention that two-dimensional systems for which most of the theoretical studies were done, can also be realized by squeezing colloids between glass plates [56] or confining them across a water-air interface [57, 58] and these can be subjected to external fields as well.

The outline of the thesis is as follows. In chapter 2 we introduce the effective interactions in star-polymer–colloid mixtures. For the interaction between the colloids we use the well known hard-sphere interaction. The pair potential of star polymers was recently derived for arm numbers larger than $f \approx 10$. The purpose of this chapter is to review these interactions and derive the effective interactions between star polymers and hard spherical colloids, as well as the interaction between star polymers with low arm numbers. Based on the effective interactions introduced in chapter 2, the phase behavior and structure of star-polymer–colloid mixtures is systematically explored in chapter 3. We solve the full two-component problem to obtain phase boundaries for the fluid-fluid demixing transition. A mapping onto an effective one-component system is performed by deriving depletion potentials for the colloids. The resulting phase diagrams are compared to the binodals of the full two-component description and the consistency is checked. In chapter 4 we turn to nonequilibrium phase transitions in driven binary colloidal mixtures. In our simple model we observe first order nonequilibrium transitions to pattern formation above a critical external force. The phase behavior is systematically investigated by computer simulations and simple theories. In chapter 5 we finally conclude with a summary and an outlook.

Chapter 2

Effective interactions in star-polymer–colloid mixtures

The study of the structural and thermodynamic properties of the polymeric state of matter has a long history in physics, which started with the pioneering work of Flory [59, 60, 61]. In the traditional, "polymeric approaches" to the matter, the chain nature of the macromolecules involved is in the foreground. However, in the last few years, alternative, complementary considerations have emerged that can loosely be called "colloidal approaches". Here, one envisions the polymer chains as diffuse, spherical objects and the chain nature of the molecules does not explicitly appear in the formalism. Instead, in a first step, almost all of the monomeric degrees of freedom are thermodynamically traced out of the problem [21]. Thereby, the polymers are replaced either by their centers of mass or by one of the monomers along their backbone, typically the end- or the central monomer. In this way, effective interactions between the polymers naturally arise [21], which implicitly include the effects of the traced-out monomers and typically have the range of the chain radius of gyration R_{g}. The earliest such approach dates back to the work of Asakura and Oosawa [62, 5], and Vrij [6], who modeled polymer chains as penetrable spheres. These models pertain mostly to Gaussian, i.e., ideal chains and are semi-quantitative. More systematic approaches have appeared in the recent years, in which self-avoiding chains are modeled and effective interactions among them are derived by means of simulations [63] or theory [64]. The gain from adopting such an alternative view is twofold: on the one hand, one has the possibility of looking at the same problem from a different angle; on the other hand, tracing out the monomers reduces the complexity of the problem by a factor N, the degree of polymerization of the chains [65]. In this chapter, we wish to carry these considerations one step further by looking at a *two-component* system of star polymers in good solvent conditions and hard, spherical, colloidal particles.

Though the star-star interaction is readily available and the colloids can be modeled as hard spheres, the effective cross interaction between star polymers and colloids is still missing. The main purpose of this chapter is to present theoretical and simulation results and to furnish analytic expressions for the force and/or the effective interaction acting between a star polymer and a spherical, colloidal particle for a large range of size ratios between the two. The theoretical approach is inspired by the earlier considerations of Pincus [66] regarding the force acting between a star and a flat wall but are made more precise here and they are also extended to include the effects of curvature. We present the general theoretical approach, both for flat and curved surfaces and derive analytic expressions for the star-colloid force which include a handful of undetermined parameters. We compare those with the results of monomer-resolved Molecular Dynamics simulations and determine the free parameters in order to achieve agreement between theory and simulation results. The effective interaction between star polymers is briefly reviewed and we present a modified version of the star-star potential which is valid for very low arm numbers, $f \lesssim 10$.

2.1 Effective interaction between star polymers and hard-sphere colloids

Let us now define the system under consideration and its relevant parameters. We consider a collection of star polymers with arm number or functionality f, and hard, spherical colloidal particles, the interaction between the latter species being modeled through the hard sphere (HS) potential

$$V_{\mathrm{cc}}(r) = \begin{cases} \infty & \text{for } r \leq \sigma_{\mathrm{c}}; \\ 0 & \text{else.} \end{cases} \tag{2.1}$$

By considering two isolated members of each species, i.e., one star and one colloid, our goal is to derive the effective interaction between the two. The colloids have a radius R_{c}, which is a well-defined length scale.

The stars, on the other hand, are soft, hairy balls without a sharply defined boundary and this leads to some freedom in defining length scales characterizing their spatial extent. The experimentally measurable length scale that naturally arises from small-angle neutron- or X-ray-scattering experiments (SANS or SAXS) is the radius of gyration R_{g} of the stars and the associated diameter of gyration $\sigma_{\mathrm{g}} = 2R_{\mathrm{g}}$. For the theoretical investigations on the subject, however, another length scale turns out to be more convenient, namely the so-called corona radius R_{s} of the star or the associated corona diameter $\sigma_{\mathrm{s}} = 2R_{\mathrm{s}}$. The corona radius arises naturally in the blob model for the conformation of isolated stars, introduced by Daoud and Cotton [67]. According to the Daoud-Cotton picture, the bulk of the interior of a star in good solvent conditions (and for sufficiently long arm chains), consists of a region in which the monomer density profile $c(s)$ follows a power-law as a function of the distance s from the star center, namely:

$$c(s) \sim a^{-3} \left(\frac{s}{a}\right)^{-4/3} \bar{v}^{-1/3} f^{2/3}, \tag{2.2}$$

with the monomer length a, the excluded volume parameter v and the reduced excluded volume parameter $\bar{v} \equiv v/a^3$. Outside this scaling region, there exists a diffuse layer of almost freely fluctuating rest chains, in which the scaling behavior of the monomer profile is not any more valid. We define the corona radius R_{s} of the star as the distance from the center up to which the scaling behavior of the monomer density given by Eq. (2.2) above holds true. In what follows, we define the *size ratio* q between the stars and the colloids as:

$$q \equiv \frac{R_{\mathrm{g}}}{R_{\mathrm{c}}}. \tag{2.3}$$

In addition, the interior of the star forms a semi dilute polymer solution in which scaling theory [68] predicts that the osmotic pressure Π scales with the concentration c as $\Pi(c) \sim c^{9/4}$. Combining the latter with Eq. (2.2) above, we obtain for the radial dependence of the osmotic pressure of the star within the scaling regime the relation:

$$\Pi(s) \sim k_B T\, f^{3/2} s^{-3} \qquad\qquad (s \leq R_{\mathrm{s}}). \tag{2.4}$$

No relation for the osmotic pressure $\Pi(s)$ for the diffuse region $s > R_{\mathrm{s}}$ is known to date. It is indeed one of the central points of this chapter to introduce an accurate ansatz for the latter, one that will allow us also to derive closed formulas for the effective force between a star and a hard object. This is the subject we examine below.

2.1.1 A star polymer and a flat wall

We begin by examining the simplest case, in which a star center is brought within a distance z from a hard, flat wall, as depicted in Fig. 2.1. Going back an idea put forward some ten years ago by Pincus [66], we can calculate the force $F_{\mathrm{sw}}(z)$ acting between the polymer and the wall by integrating the normal component of the osmotic pressure $\Pi(s)$ along the area of contact between the star and the wall. In the geometry shown in Fig. 2.1, this takes the form:

$$F_{\mathrm{sw}}(z) = 2\pi \int_{y=0}^{y=\infty} \Pi(s) \cos\vartheta\, y \mathrm{d}y. \tag{2.5}$$

Using $z = s\, \cos\vartheta$ and $y = z\, \tan\vartheta$ we can transform Eq. (2.5) into:

$$F_{\mathrm{sw}}(z) = 2\pi z \int_{z}^{\infty} \Pi(s) \mathrm{d}s. \tag{2.6}$$

Eq. (2.6) above implies immediately that, if the functional form for the force $F_{\mathrm{sw}}(z)$ were to be known, then the corresponding functional form for the osmotic pressure $\Pi(z)$ could be obtained through:

$$\Pi(z) \propto -\frac{\mathrm{d}}{\mathrm{d}z}\left(\frac{F_{\mathrm{sw}}(z)}{z}\right). \tag{2.7}$$

To this end, we now refer to known, exact results regarding the force acting between a flat wall and a *single, ideal chain* whose one end is held at a distance z from a flat wall [69].

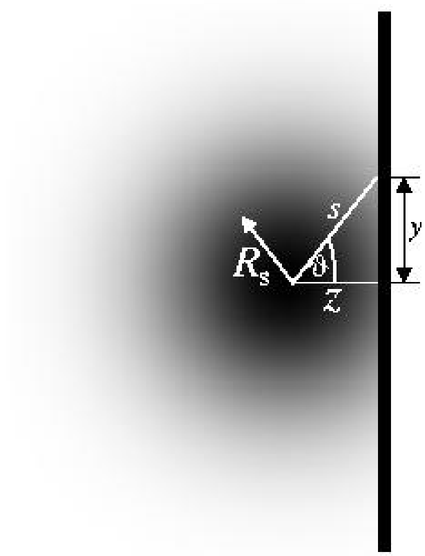

Figure 2.1: Star polymer (black-shadowed particle) interacting with a flat wall. The star polymer consists of a inner core region, where the scaling behavior is dominant, whereas the outer regime is shadowed and indicates the exponential decay of the osmotic pressure.

There, it has been established that the force $F_{\rm sw}^{\rm (id)}(z)$ is given by the relation:

$$F_{\rm sw}^{\rm (id)}(z) = k_BT\frac{\partial}{\partial z}\ln\left[\mathrm{erf}\left(\frac{z}{L}\right)\right], \tag{2.8}$$

where $\mathrm{erf}(x) = 2/\sqrt{\pi}\int_0^x e^{-t^2}\mathrm{d}t$ denotes the error function and L is some length scale of the order of the radius of gyration of the polymer. Carrying out the derivative and setting erf(x) $\cong 1$ for $x \gg 1$, we obtain a Gaussian form for the chain-wall force at large separations:

$$F_{\rm sw}^{\rm (id)}(z) \cong \frac{k_BT}{L}\exp\left(-\frac{z^2}{L^2}\right) \qquad (z \gg L). \tag{2.9}$$

We now imagine a star composed of ideal chains. As the latter do not interact with each other ("ghost chains") the result of Eq. (2.9) holds for the star as well. Going now to self-avoiding chains, we assert that, as the main effect giving rise to the star-wall force is the volume which the wall excludes to the chains, rather than the excluded volume interactions between the chains themselves, a relation of the form (2.9) must also hold for the force $F_{\rm sw}(z)$ between a wall and a *real* star, but with the length scale L replaced by the radius of gyration or the corona radius of the latter and with an additional, f-dependent prefactor for taking into account the stretching effects of the f grafted polymeric chains. From Eqs. (2.7) and (2.9) it now follows that

$$\Pi(s) \propto \frac{k_B T}{L}\left(\frac{1}{s^2}+\frac{2}{L^2}\right)\exp\left(-\frac{s^2}{L^2}\right) \qquad (s \gg L). \tag{2.10}$$

The full expression for $\Pi(s)$ now follows by combining Eq. (2.4), valid for $s \leq R_{\rm s}$, with Eq. (2.10), valid for $s \gg L \cong R_{\rm s}$, and matching them at $s = R_{\rm s}$. The local osmotic pressure $\Pi(s)$ is the interior of a star polymer, as a function of the distance s from its center has hence the functional form:

$$\Pi(s) = \Lambda f^{3/2} k_B T \begin{cases} s^{-3} & \text{for } s \leq R_{\rm s}; \\ \left(\frac{1}{s^2}+2\kappa^2\right)\frac{\xi}{R_{\rm s}}\exp\left[-\kappa^2\left(s^2-R_{\rm s}^2\right)\right] & \text{for } s > R_{\rm s}, \end{cases} \tag{2.11}$$

where Λ and $\kappa = L^{-1}$ are free parameters; it is to be expected that $\kappa = O(R_{\rm g}^{-1})$, as we will verify shortly. On the other hand, ξ must be chosen to guarantee that $\Pi(s)$ is continuous at $s = R_{\rm s}$, resulting into the value:

$$\xi = \frac{1}{1+2\kappa^2 R_{\rm s}^2}. \tag{2.12}$$

Eq. (2.11) above concerns the radial distribution of the osmotic pressure of an isolated star. The question therefore arises, whether this functional form for the osmotic pressure can be used in order to calculate the force between a star and a flat wall also in situations where the star-wall separation is smaller than the radius of gyration of the star, in which case it is intuitively expected that the presence of the wall will seriously disturb the monomer distribution around the center and hence also the osmotic pressure. In fact, it is to be expected the osmotic pressure is a function of *both* the star-wall separation z and the radial distance s, whereas in what follows we are going to be using Eq. (2.6) together with Eq. (2.11), in which $\Pi(s)$ has no z-dependence itself. However, it turns out that this is an excellent approximation. On the one hand, it is physically plausible for large star-wall separations, where the presence of the wall has little effect on the segment density profile around the star center and the ensuing osmotic pressure profile. On the other hand, also at very small star-wall separations, the scaling form $\Pi(s) \sim s^{-3}$ continues to be valid. To corroborate this claim, we proceed with some arguments to this effect.

First, we refer once more to known, exact results concerning the radial distribution of the pressure on a hard wall arising from an ideal chain grafted on it [70], a situation similar to holding one end of a chain at a distance very close to the wall surface. The pressure $\Pi_{\rm id}(s)$ reads as [70]:

$$\Pi_{\rm id}(s) = \frac{1}{2\pi}\frac{1}{(s^2+a^2)^{3/2}}\left(1+\frac{s^2+a^2}{2R_{\rm g}^2}\right)\exp\left[-\frac{s^2+a^2}{4R_{\rm g}^2}\right], \tag{2.13}$$

with the segment length a, indicating that in the regime $a \ll s \ll R_{\rm g}$ indeed the scaling $\Pi_{\rm id}(s) \sim s^{-3}$ holds.

Second, we can employ a scaling argument, asserting that, on dimensional grounds, the osmotic pressure exerted by a star on a nearby flat wall and held at a distance z from it, must

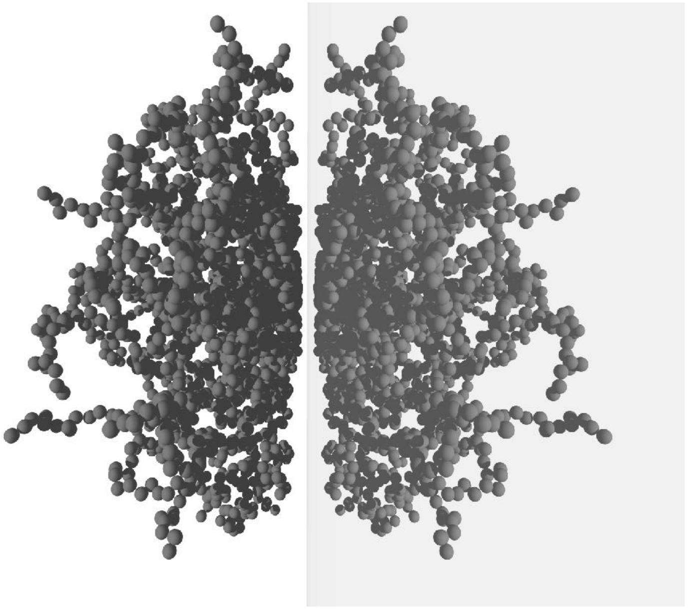

Figure 2.2: Snapshot of a simulation showing a star polymer interacting with a flat wall, at a small center-to-surface distance. The mirror-reflected image of the star, on the right, helps demonstrate that the configuration is similar to that of an isolated star with twice as many arms.

be of the form $\Pi(s,z) = k_BTR_{\mathrm{g}}^{-3}\, h(s/R_{\mathrm{g}}, z/R_{\mathrm{g}})$, with some scaling function $h(x,y)$; universality arguments dictate that the segment length a should not appear in the dimensional analysis and hence s, z and R_{g} are the only relevant length scales for this problem. Now, for small star-wall separations, $z \ll R_{\mathrm{g}}$, we replace the second argument of this function by zero. Moreover, we assert that, as the dominant contribution to the osmotic pressure for distances $s < R_{\mathrm{g}}$ comes from the first few monomers along the chains colliding with the wall, the degree of polymerization N of the chains should be irrelevant if the chains are long. Hence, all R_{g}-dependence of the pressure should drop out, with the implication $h(x,0) \sim x^{-3}$ for $x \ll 1$ and hence $\Pi(s) \sim s^{-3}$ in this regime. Third, we point out that bringing a star with f arms at a small distance to a flat wall, creates a conformation which is very similar to one of an isolated star with $2f$-arms, as shown in Fig. 2.2. Hence, it is not surprising that at small star-wall separations, one recovers for the radial dependence osmotic pressure the scaling laws pertinent to an isolated star.

Finally, by inserting Eq. (2.11) into Eq. (2.6) and carrying out the integration, we find that for small star-wall distances, $z \ll R_{\mathrm{s}}$, the force scales as $F_{\mathrm{sw}}(z) \sim (k_BT)/z$, thus giving rise to a logarithmic effective star-wall potential $V_{\mathrm{sw}}(z) \sim -k_BT\ln(z/R_{\mathrm{s}})$. The latter is indeed in full agreement with predictions from scaling arguments arising in polymer theory [66, 71, 72]. This is a universal result, in the sense that it also holds for single chains, be it real or ideal, as it can also be read off from the exact result, Eq. (2.8), using the property $\mathrm{erf}(x) \sim x$ for $x \to 0$. Thus, the proposed functional form for the osmotic pressure, Eq.

(2.11), combined with Eq. (2.6) for the calculation of the effective force, has the following remarkable property: it yields the correct result both at small and at large star-wall distances and therefore appears to be a reliable analytical tool for the calculation of the effective force at *all* star-wall distances. At the same time, it contains two free parameters, Λ and κ which allow some fine tuning when the predictions of the theory are to be compared with simulation results, as we will do below. Yet, we emphasize that this freedom is *not* unlimited: on physical grounds, κ must be of the order of R_{g}^{-1} and Λ must be a number of order unity for all functionalities f, as the dominant, $f^{3/2}$-dependence of the osmotic pressure prefactor has been already explicitly taken into account in Eq. (2.11).

We are now in a position to write down the full expression for the star-wall force, by using Eqs. (2.6) and (2.11). The result reads as:

$$\frac{R_{\mathrm{s}} F_{\mathrm{sw}}(z)}{k_B T} = \Lambda f^{3/2} \begin{cases} \frac{R_{\mathrm{s}}}{z} + \frac{z}{R_{\mathrm{s}}}(2\xi - 1) & \text{for } z \leq R_{\mathrm{s}}; \\ 2\xi \exp[-\kappa^2 (z^2 - R_{\mathrm{s}}^2)] & \text{for } z > R_{\mathrm{s}}. \end{cases} \tag{2.14}$$

Note the dominant, $\sim 1/z$-dependence for $z \to 0$. Accordingly, the effective interaction potential $V_{\mathrm{sw}}(z)$ between a star and a flat, hard wall held at a center-to-surface distance z from each other reads as:

$$\beta V_{\mathrm{sw}}(z) = \Lambda f^{3/2} \begin{cases} -\ln(\frac{z}{R_{\mathrm{s}}}) - (\frac{z^2}{R_{\mathrm{s}}^2} - 1)(\xi - \frac{1}{2}) + \zeta & \text{for } z \leq R_{\mathrm{s}}; \\ \zeta\, \mathrm{erfc}(\kappa z)/\mathrm{erfc}(\kappa R_{\mathrm{s}}) & \text{for } z > R_{\mathrm{s}}, \end{cases} \tag{2.15}$$

with the inverse temperature $\beta = (k_B T)^{-1}$, the additional constant

$$\zeta = \frac{\sqrt{\pi}\xi}{\kappa R_{\mathrm{s}}} \exp(\kappa^2 R_{\mathrm{s}}^2)\, \mathrm{erfc}(\kappa R_{\mathrm{s}}) \tag{2.16}$$

and the complementary error function $\mathrm{erfc}(x) = 1 - \mathrm{erf}(x)$. This completes our theoretical analysis of the star polymer-wall force and the ensuing effective interaction potential. The comparison with simulation data and the determination of the free parameters in the theory will be discussed in section 2.1.3. We now proceed with the calculation of the effective force between a star and a spherical hard particle, where effects of the colloid curvature become important.

2.1.2 A star polymer and a spherical colloid

We apply the same idea as for the case of the hard wall: the effective force acting at the center of the objects is obtained by integrating the osmotic pressure exerted by the polymer on the surface of the colloid. In Fig. 2.3, the geometrical situation is displayed: within the corona radius of the star polymer $R_{\mathrm{s}} = \sigma_{\mathrm{s}}/2$, the osmotic pressure is determined by scaling laws; the outer regime is shadowed and signifies the Gaussian decay of the osmotic pressure. At center-to-surface distance z (center-to-center distance $r = z + R_{\mathrm{c}}$), the integration of the osmotic pressure is carried out over the contact surface between star and colloid. Taking

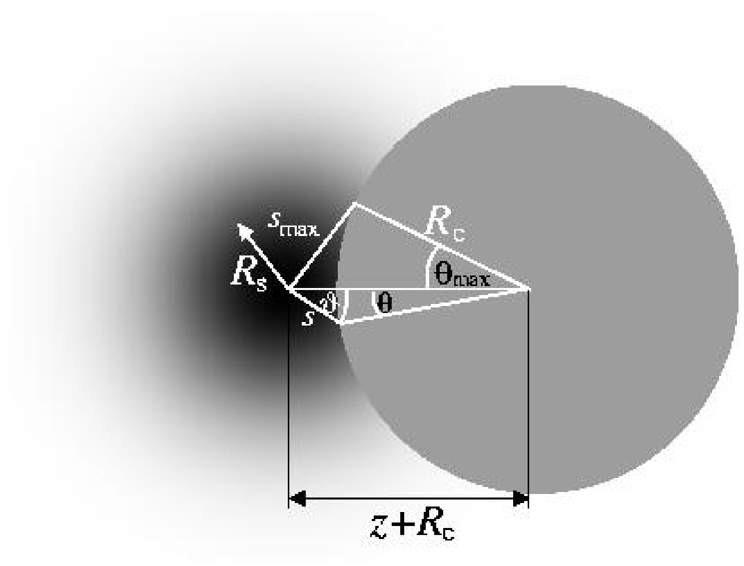

Figure 2.3: Star polymer (black-shadowed particle) interacting with a colloidal particle (grey sphere). The dark and shadowed regions of the star have the same meaning as in Fig. 2.1.

into account the symmetry of the problem, e.g., its independence of the azimuthal angle, we obtain the force $F_{sc}(z)$ between the star and the colloid as:

$$F_{\rm sc}(z) = 2\pi R_{\rm c}^2 \int_0^{\theta_{\max}} {\rm d}\theta \, \sin\theta \, \Pi(s) \cos\vartheta, \tag{2.17}$$

where ϑ and θ are polar angles emanating from the center of the star polymer and the colloid, respectively. The variables ϑ and θ can be eliminated in favor of the variable s, which denotes the distance between the center of the star and an arbitrary point on the surface of the colloid. This elimination is achieved by taking into consideration the geometrical relations (see Fig. 2.3):

$$s \, \sin\vartheta = R_{\rm c} \sin\theta \tag{2.18}$$

and

$$s \, \cos\vartheta + R_{\rm c} \cos\theta = R_{\rm c} + z. \tag{2.19}$$

Eqs. (2.17), (2.18) and (2.19) yield for the star-colloid effective force the transformed integral:

$$F_{\rm sc}(z) = \frac{\pi R_{\rm c}}{(z+R_{\rm c})^2} \int_z^{s_{\max}} {\rm d}s \, \left[(z+R_{\rm c})^2 - R_{\rm c}^2 + s^2\right] \Pi(s) \tag{2.20}$$

The maximum integration distance, $s_{\max}$, depends geometrically on $\theta_{\max}$, as well as on the distance z of the star polymer to the surface of the colloid and on R_{c}. The relation reads as

$$\begin{aligned} s_{\max} &= \sqrt{[z + R_{\mathrm{c}}(1-\cos\theta_{\max})]^2 + (R_{\mathrm{c}}\sin\theta_{\max})^2} \\ &= \frac{1}{q}\sqrt{[qz + R_{\mathrm{g}}(1-\cos\theta_{\max})]^2 + (R_{\mathrm{g}}\sin\theta_{\max})^2}. \end{aligned} \tag{2.21}$$

By introducing Eq. (2.11) into Eq. (2.20), an analytic expression for the effective force follows, which reads as

$$\frac{F_{\mathrm{sc}}(z)}{k_{\mathrm{B}}T} = \frac{\Lambda f^{3/2} R_{\mathrm{c}}}{(z+R_{\mathrm{c}})^2} \begin{cases} [(z+R_{\mathrm{c}})^2 - R_{\mathrm{c}}^2]\left[\frac{1}{2z^2} - \frac{1}{2{R_{\mathrm{s}}}^2} + \Psi_1(R_{\mathrm{s}})\right] - \ln(\frac{z}{R_{\mathrm{s}}}) + \Psi_2(R_{\mathrm{s}}) & \text{for } z \le R_{\mathrm{s}}; \\ [(z+R_{\mathrm{c}})^2 - R_{\mathrm{c}}^2]\,\Psi_1(z) + \Psi_2(z) & \text{for } z > R_{\mathrm{s}}. \end{cases} \tag{2.22}$$

Here, the functions $\Psi_1(x)$ and $\Psi_2(x)$ are given by:

$$\Psi_1(x) = \frac{\xi}{R_{\mathrm{s}}}\exp\left(\kappa^2 R_{\mathrm{s}}^2\right)\left[\frac{1}{x}\exp\left(-\kappa^2 x^2\right) - \frac{1}{s_{\max}}\exp\left(-\kappa^2 s_{\max}^2\right)\right], \tag{2.23}$$

and

$$\Psi_2(x) = \frac{\xi}{R_{\mathrm{s}}}\exp\left(\kappa^2 R_{\mathrm{s}}^2\right)\left[\frac{\sqrt{\pi}}{\kappa}\left[\mathrm{erf}\left(\kappa s_{\max}\right) - \mathrm{erf}\left(\kappa x\right)\right] + x\exp\left(-\kappa^2 x^2\right) - s_{\max}\exp\left(-\kappa^2 s_{\max}^2\right)\right], \tag{2.24}$$

where ξ is given by Eq. (2.12). Note that, for small distances, both regimes of the osmotic pressure contribute to the integral, whereas for larger distances, $z > R_{\mathrm{s}}$, only the Gaussian decay does so. Due to the additional dependence of $s_{\max}$ on the distance z, [see Eq. (2.21)], an analytical expression for the effective potential $V_{\mathrm{sc}}(z)$, analogous to Eq. (2.15) for the flat-wall case, is not possible here.

Some remarks regarding $F_{\mathrm{sc}}(z)$ are necessary. First, for small separations z, the force scales as $F_{\mathrm{sc}}(z) \sim (k_B T)/z$, the same behavior found for the flat-wall case. Once more, we obtain the universal result mentioned above, which has been shown to be also valid for an ideal chain whose one end is held at a distance z from the surface of a hard sphere. Indeed, for this case the force is given by the exact relation [73]:

$$F_{\mathrm{sc}}^{(\mathrm{id})}(z) = k_B T \frac{\partial}{\partial z}\ln\left[1 - \left(\frac{R_{\mathrm{c}}}{z+R_{\mathrm{c}}}\right)\mathrm{erfc}\left(\frac{z}{L}\right)\right], \tag{2.25}$$

with L being a length scale of order R_{g}. Eq. (2.25) above, yields $F_{\mathrm{sc}}^{(\mathrm{id})}(z) \sim (k_B T)/z$ for $z \to 0$.

Second, let us consider the limit of small size ratios $q = R_{\mathrm{g}}/R_{\mathrm{c}}$. As can be seen from Eq. (2.21), the upper integration limit $s_{\max}$ scales as R_{g}/q, whereas the decay parameter κ is of the order R_{g}^{-1}. Hence, $\kappa s_{\max} \sim q^{-1}$, with the implication that for small enough q's, the argument $\kappa s_{\max}$ in the error function and in the Gaussian in Eqs. (2.23) and (2.24) can be replaced by infinity. As we will shortly see, this is an excellent approximation up to $q \lesssim 0.3$, as both $\mathrm{erf}(x)$ and $\exp(-x^2)$ approach their asymptotic values for $x \to \infty$ rapidly. Then, the implicit z-dependence of the force $F_{\mathrm{sc}}(z)$ through $s_{\max}$ drops out and a z-integration of the latter can be analytically carried out to obtain an effective star polymer-colloid potential $V_{\mathrm{sc}}^{\infty}(z)$ which reads as:

$$\beta V_{\mathrm{sc}}^{\infty}(z) = \Lambda f^{3/2} \left(\frac{R_{\mathrm{c}}}{z + R_{\mathrm{c}}}\right) \begin{cases} -\ln(\frac{z}{R_{\mathrm{s}}}) - (\frac{z^2}{R_{\mathrm{s}}^2} - 1)(\xi - \frac{1}{2}) + \zeta & \text{for } z \leq R_{\mathrm{s}}; \\ \zeta\, \mathrm{erfc}(\kappa z)/\mathrm{erfc}(\kappa R_{\mathrm{s}}) & \text{for } z > R_{\mathrm{s}}, \end{cases} \tag{2.26}$$

with the constant ζ given by Eq. (2.16). Clearly, in the limit $R_{\mathrm{c}} \to \infty$ ($q \to 0$), corresponding to a flat wall, Eq. (2.26) reduces to the previously derived result, Eq. (2.15). It is a remarkable feature that all effects of curvature are taken into account by the simple geometrical prefactor $R_{\mathrm{c}}/(z + R_{\mathrm{c}})$, for sufficiently small size ratios q. In this respect, the above result bears close similarity to the well-known Derjaguin approximation [74].

2.1.3 Molecular Dynamics simulation

In order to check the theoretical prediction of the forces at hard objects, we performed a monomer-resolved Molecular Dynamics (MD) simulation [75] and calculated the mean force at the center of the star polymer to compare the data with theory. The model is based on the ideas of simulation methods applied on linear polymers and on a single star [76, 77]. The main features are as follows.

A purely repulsive and truncated Lennard-Jones potential acts between all Nf monomers at distances r:

$$V_{\mathrm{LJ}}(r) = \begin{cases} 4\epsilon \left[\left(\frac{\sigma_{\mathrm{LJ}}}{r}\right)^{12} - \left(\frac{\sigma_{\mathrm{LJ}}}{r}\right)^{6} + \frac{1}{4} \right] & \text{for } r \leq 2^{1/6}\sigma_{\mathrm{LJ}}; \\ 0 & \text{for } r > 2^{1/6}\sigma_{\mathrm{LJ}}. \end{cases} \tag{2.27}$$

Here, σ_{LJ} is the microscopic length scale of the beads and ϵ sets the energy scale. In accordance with previous work [26], we have chosen $T = 1.2\epsilon/k_B$.

An attractive FENE (finite extensible nonlinear elastic) potential additionally acts between neighboring monomers along a chain [76]:

$$V_{\mathrm{FENE}}(r) = \begin{cases} -15\epsilon \left(\frac{R_0}{\sigma_{\mathrm{LJ}}}\right)^2 \ln \left[1 - \left(\frac{r}{R_0}\right)^2\right] & \text{for } r \leq R_0; \\ \infty & \text{for } r > R_0. \end{cases} \tag{2.28}$$

This interaction diverges at $r = R_0$, which determines the maximal relative displacement of two neighboring beads. The energy ϵ is the same as in Eq. (2.27), whereas for the length scale R_0 we have chosen the value $R_0 = 1.5\,\sigma_{\mathrm{LJ}}$.

To accommodate the polymer arms, a hard core with radius R_{d} is introduced at the center of the star; its size depends on the arm number f. Accordingly, the interactions between the monomers and the central particle were introduced. All monomers had a repulsive interaction $V_{\mathrm{LJ}}^{p}(r)$ of the truncated and shifted Lennard-Jones type with the central particle,

$$V_{\mathrm{LJ}}^{p}(r)=\begin{cases}\infty & \text{for } r\leq R_{\mathrm{d}};\\ V_{\mathrm{LJ}}(r-R_{\mathrm{d}}) & \text{for } r>R_{\mathrm{d}},\end{cases} \tag{2.29}$$

whereas the innermost monomers in the chain an additional attractive potential $V_{\mathrm{FENE}}^{p}(r)$ of the FENE type, namely

$$V_{\mathrm{FENE}}^{p}(r)=\begin{cases}\infty & \text{for } r\leq R_{\mathrm{d}};\\ V_{\mathrm{FENE}}(r-R_{\mathrm{d}}) & \text{for } r>R_{\mathrm{d}}.\end{cases} \tag{2.30}$$

Finally, all monomers interact with the colloid or with the wall by a hard potential. We note that exactly this simulation model was already used by Grest *et al.* in their simulations of linear and star polymers in good solvent conditions [76, 77].

The time step is typically $\Delta t = 0.002t^{*}$ with $t^{*}=\sqrt{m\sigma_{\mathrm{LJ}}^{2}/\epsilon}$ being the associated time unit and m the monomer mass. After a long equilibration time (500 000 MD steps), the mean force at the core of the star whose center is held at the position $\boldsymbol{R}$ and its dependence on the arm number f separations, is calculated as the expectation value over all instantaneous forces acting on the star core:

$$\boldsymbol{F}(\boldsymbol{R})=\left\langle-\nabla_{\boldsymbol{R}}\left[\sum_{k=1}^{fN}V_{\mathrm{LJ}}^{p}(|\boldsymbol{r}_k-\boldsymbol{R}|)+\sum_{l=1}^{f}V_{\mathrm{FENE}}^{p}(|\boldsymbol{r}_l-\boldsymbol{R}|)\right]\right\rangle, \tag{2.31}$$

where the first sum is carried over all fN monomers of the star and the second only over the f innermost monomers of its chains. The direct force between the central particle and the wall did not need to be considered, as the center-to-surface distance was always kept at values where this force was vanishingly small. Note that choosing the origin of the coordinate system on the surface of the colloidal particle or wall, at the point of nearest separation between the star center and this surface, and also the z-axis in the direction connecting this origin with the star center, we immediately obtain $R\equiv|\boldsymbol{R}|=z$.

We have carried out simulations for a variety of arm numbers f and size ratios q, allowing us to make systematic predictions for the f- and q-dependencies of all theoretical parameters. In attempting to compare the simulation results with the theoretical predictions, one last obstacle must be removed: in theory, the fundamental length scale characterizing the star is the corona radius R_{s}. The latter, however, is not directly measurable in a simulation in which, instead, we can only assess to the radius of gyration R_{g}. Yet, we have previously found that the ratio between the two remains fixed for all considered arm numbers f, having the value $R_{\mathrm{s}}/R_{\mathrm{g}}\simeq 0.66$ [26]. We now proceed with the presentation of our MD results.

We consider at first a star polymer near a hard wall. The theoretical prediction of the effective interaction force is given in Eq. (2.14). First, we consider the limit of small separations, $z\to 0$, which allows us on the one hand to test the theoretical prediction

f	$R_\mathrm{d}/R_\mathrm{s}$	Λ	κR_s	τR_s
2	0.006	0.46	0.58	1.03
5	0.018	0.35	0.68	1.12
6	0.012	0.34	0.72	1.13
10	0.06	0.30	0.74	1.15
15	0.12	0.28	0.76	-
18	0.09	0.27	0.77	-
30	0.12	0.24	0.83	-
40	0.152	0.24	0.85	-
50	0.152	0.23	0.86	-
80	0.273	0.22	0.88	-
100	0.303	0.22	0.89	-

Table 2.1: The fit parameters arising from the comparison between theory and simulation for the star-colloid interaction and for the star-star interaction for very low arm numbers, see sec. 2.2. The values of R_d shown here are not exactly the same as the input core size; they are just in the same order of magnitude, deviating only slightly from the real input value. They are still corresponding to microscopic length, and are thus irrelevant at length scales $r \sim \sigma_\mathrm{s}$. Λ is the overall prefactor and κ the inverse Gaussian decay length, both used in the star-wall and star-colloid interaction Eqs. (2.22) and (2.26). τ is the inverse Gaussian decay length for the star-star interaction for very low arm numbers. $\sigma_\mathrm{s} = 2R_\mathrm{s} = 0.66\,\sigma_\mathrm{g}$ denotes the corona diameter of the stars, as measured during the simulation.

$F_\mathrm{sw}(z) \cong k_B T \Lambda f^{3/2}/z$ there and on the other hand to fix the value of the prefactor Λ, which is expected to have in general a weak f-dependence. For this prefactor, some semi-quantitative theoretical predictions already exist: For $f = 1, 2$ the prefactor may be calculated from the bulk and the ordinary surface critical exponents ν, γ and γ^o, γ_1^o of the n-vector model. For $n = 0$ this results in $\Lambda(f = 1) = (\gamma - \gamma_1^o)/\nu$ and $2^{3/2}\Lambda(f = 2) = (\gamma - \gamma^o)/\nu = 1/\nu$ [78, 79]. Numerical values for the exponents are known from renormalization group theory and simulation [80, 81] and yield $\Lambda(f = 1) \approx 0.83$ and $\Lambda(f = 2) \approx 0.60$. On the other hand, for very large functionalities, $f \gg 1$, one can make an analogy between a star at distance z from a wall and two star polymers whose centers are kept at distance $r = 2z$ from each other [66]. Indeed, for very large f, the conformations assumed by two stars brought close to each other is one in which the chains of each star retract to the half-space where the center of the star lies, a situation very similar to the star-wall case. Then, one can make the approximation $F_\mathrm{sw}(z) \cong F_\mathrm{ss}(2z)$, where F_ss denotes the star-star force. For the latter, it is known [25] that it has the form:

$$F_\mathrm{ss}(r) = \frac{5}{18} f^{3/2} \frac{1}{r} \qquad (r \to 0), \tag{2.32}$$

implying for the coefficient Λ the asymptotic behavior:

$$\lim_{f\to\infty}\Lambda(f) \equiv \Lambda_\infty = \frac{5}{36} \cong 0.14. \tag{2.33}$$

Since there is no theory concerning the values of Λ in the intermediate regime of f, Λ is used as fit parameter. Its value can be obtained by plotting the inverse force $1/F_{\rm sw}(z)$ against z for small separations z to the hard wall. The results are shown in Fig. 2.4. Looking first at the inset, we see that, as for the earlier case of star-star interactions [26], the reciprocal force curves do not go through the origin, as a result of the finite core size, $R_{\rm d}$. Once this is subtracted, though, straight lines passing through the origin are obtained, verifying in this way the $1/z$-behavior of the force and the associated logarithmic dependence of the effective potential at small separations. The values for $\Lambda(f)$ can be immediately read off from the slope of the curves and they are summarized in Table 2.1. There and in Fig. 2.5 we see that Λ is indeed a decreasing function of f but the asymptotic value $\Lambda_\infty = 5/36$ is still not achieved at arm numbers as high as $f = 100$.

The decay parameter κ is fixed by looking at the force at larger separations and the obtained are also summarized in Table 2.1 and shown in Fig. 2.5. As expected, κ is of the order $R_{\rm g}^{-1}$, as witnessed by the fact that the product $\kappa R_{\rm s}$ is of order unity. A monotonic increase of $\kappa\sigma_{\rm g}$ with the arm number f is observed, consistent with the view that for large f stars form compact objects with an increasingly small diffuse layer beyond their coronae [25].

With parameters Λ and κ *once and for all fixed* from the star-wall case, we now turn our attention to the interaction of a star polymer at a hard sphere of finite radius $R_{\rm c}$, equivalently size ratios $q \neq 0$. Here, the force is given by the full expressions of Eqs. (2.22), (2.23) and (2.24); for small enough size ratios q, the approximation $\kappa s_{\rm max} \to \infty$ gives rise to a simplified expression for the force and to the analytical formula, Eq. (2.26) for the effective star-colloid potential. Our purpose is twofold: to test the validity of these simplified expressions as a function of q and also to find an economical way to parameterize $s_{\rm max}$ as a function of q for those values of the size ratio for which the approximation $\kappa s_{\rm max} \to \infty$ turns out to be unsatisfactory.

We show representative results for fixed arm number $f = 18$ and varying q in Fig. 2.6; results for different f-values are similar. It can be seen that the simplified result arising from allowing $s_{\rm max} \to \infty$ yields excellent results up to size ratios $q \lesssim 0.3$, see Figs. 2.6(a) and (b). However, above this value, the approximation of integrating the osmotic pressure up to infinitely large distances breaks down, as it produces effective forces that are larger than the simulation results, especially at distances z of order of the radius of gyration $R_{\rm g}$. These are the dashed lines shown in Figs. 2.6(c)-(e). The overestimation of the force is not surprising: as can be seen from Fig. 2.3 and Eq. (2.20), we are integrating a positive quantity beyond the physically allowed limits and this will inadvertently enhance the resulting force. Hence, we have to impose a finite upper limit $s_{\rm max}$ for size ratios $q > 0.3$ in order to truncate the contribution of the Gaussian tail in the integral of the osmotic pressure in Eq. (2.20).

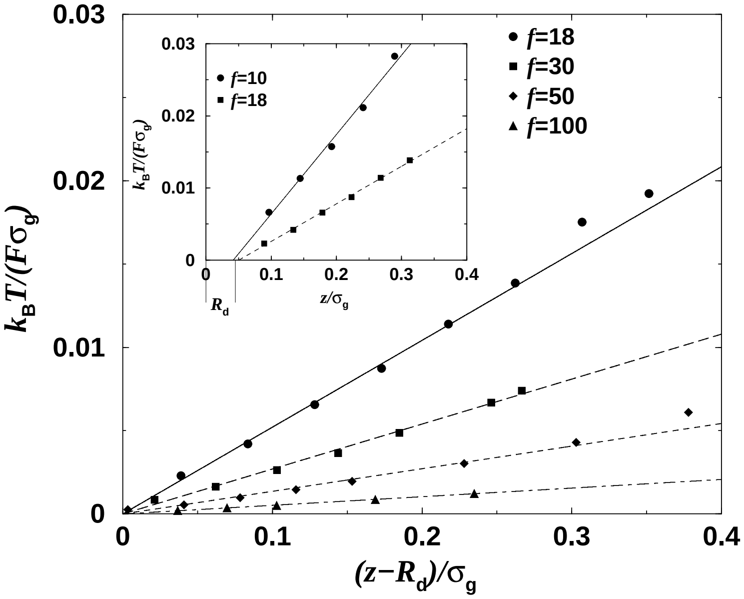

Figure 2.4: Reciprocal effective force between a star polymer and a hard flat wall plotted against the distance z between the star center to the surface of the wall for small z-values. The dependence $F(z) \sim 1/z$ is confirmed by the simulation results (symbols). The prefactor of the potential depends on f and manifests itself in the different slopes of the reciprocal forces. The inserted plot shows the divergence of the force at the distance $z = R_\mathrm{d}$, which is subtracted from z in the outset of the plot, to achieve divergence of the force in the origin.

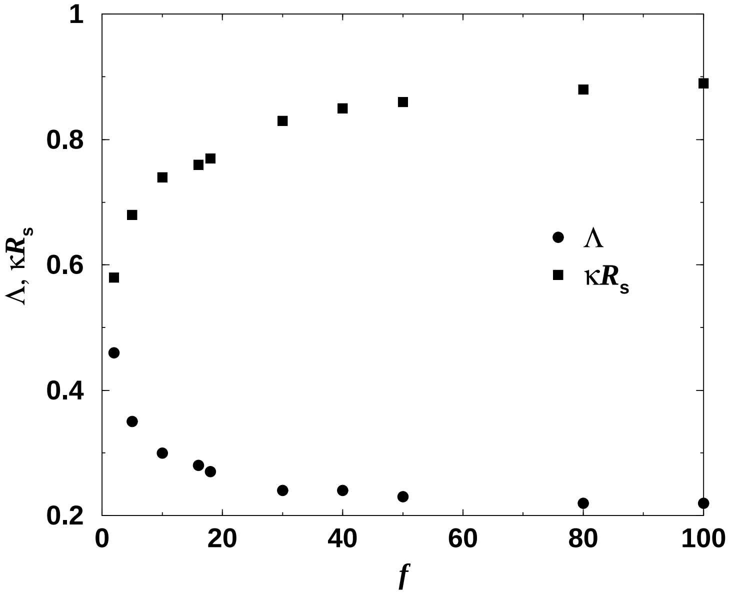

Figure 2.5: The prefactor of Λ and the decay parameter κ of Eq. (2.14) plotted against the functionality f. The value of $\Lambda = 5/36 \approx 0.14$ for $f \gg 1$ is not reached but the simulation data tend to this value very slowly. κ shows a monotonic increase with arm number f.

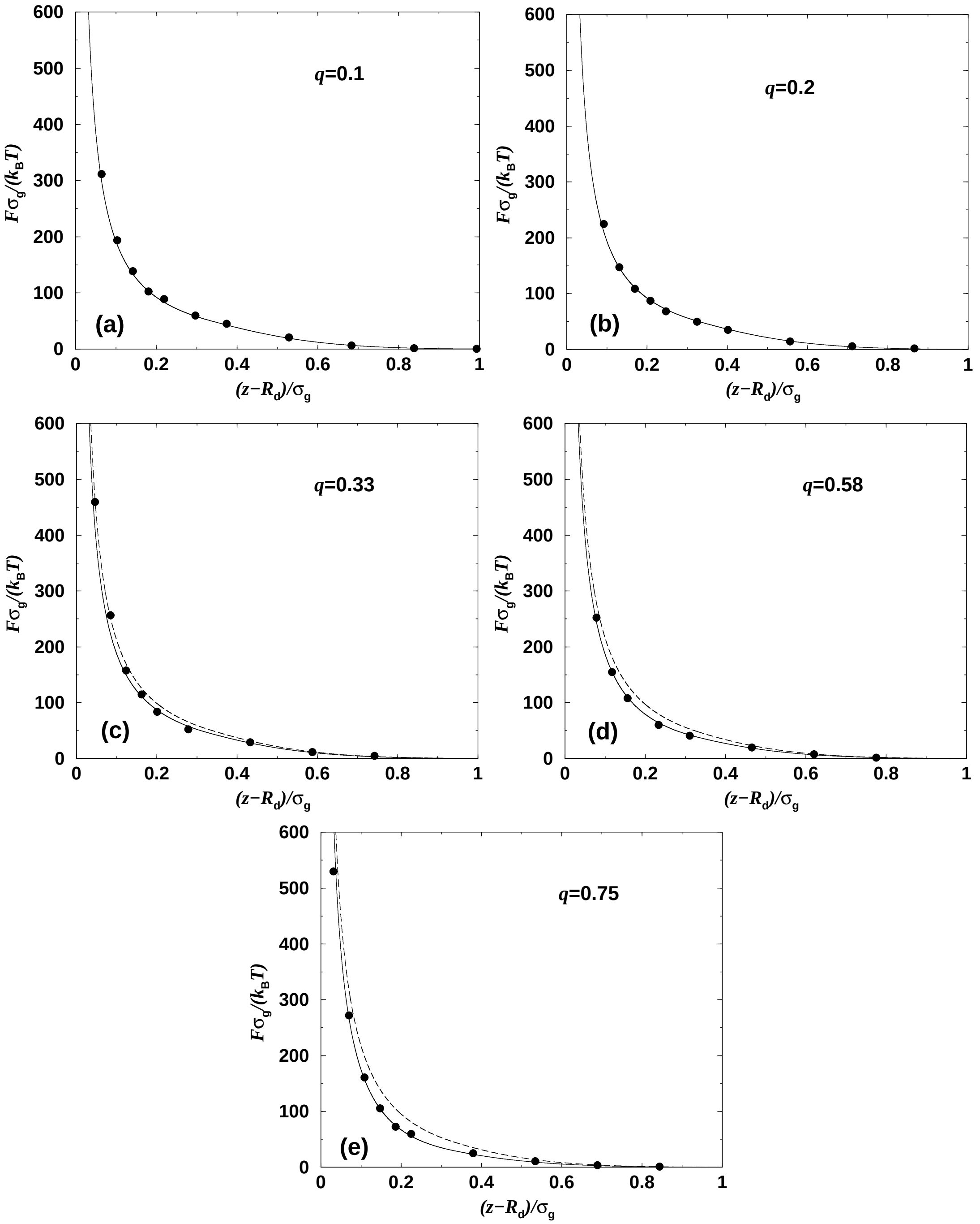

Figure 2.6: Comparison between simulation (symbols) and theoretical (lines) results for the effective force between a star polymer and a colloidal particle for different size ratios q, as a function of the center-to-surface separation z. The arm number here is $f = 18$. The solid lines in (a) and (b) are derived from Eq. (2.22) for $s_{\max} \to \infty$. In (c)-(e) the curves derived by means of this approximation are shown dashed and they increasingly deviate from the simulation results as q grows. Thereby, a finite upper integration limit has to be introduced (see the text), producing the curves denoted by the solid lines in (c)-(e) and bringing about excellent agreement with simulation.

In Fig. 2.7 a typical snapshot of a star polymer at a colloid illustrates the situation. One can see that the main contribution of the osmotic pressure results from in the inner region of the star. The outer region of the chains only interact weakly with the sphere. The question now is how the value of $s_{\max}$ must be chosen. As can be seen from Eq. (2.21), this quantity is dependent on, R_{s}, z and $\theta_{\max}$. (The latter depending on q means that $\theta_{\max}$ and q should not be treated as independent quantities.) It would be indeed most inconvenient if for every combination of these we would have to choose a different upper integration limit. Hence, we have attempted to transfer all dependence of $s_{\max}$ onto the maximum integration angle $\theta_{\max}$. We found that this is indeed possible and, in fact, the angle $\theta_{\max}(q)$ has a very weak q-dependence: starting with a value $\theta_{\max} \approx 45^{\circ}$ at $q = 0.3$, we find that it then quickly saturates into the value $\theta_{\max} \approx 30^{\circ}$ for all $q \gtrsim 0.35$. In this way, we are able to obtain the corrected curves denoted by the solid lines in Figs. 2.6(c)-(e), showing excellent agreement with the simulation results.

We finally turn our attention to the f-dependence of the forces for a fixed value of the size ratio, $q = 0.33$. In Fig. 2.8 we show the simulation results compared with theory for a wide range of arm numbers, $5 \leq f \leq 50$. For the theoretical fits, the values of Λ and κ from Table 2.1 were used, whereas the value of the maximum integration angle was kept fixed at $\theta_{\max} = 30^{\circ}$ for all f-values. The agreement between theory and simulation is very satisfactory.

Thus, our conclusions for the star polymer-colloid interaction read as follows: the general, analytical expression for the *force* between the two is given by Eqs. (2.22), (2.23) and (2.24), supplemented by Eq. (2.21) in which the angle $\theta_{\max}$ has to be chosen as discussed above for $q \gtrsim 0.3$. An analytical formula for the effective *interaction potential* $V_{\mathrm{sc}}(z)$ is not possible for such size ratios. Rather, the results for the effective force have to be integrated numerically in order to obtain $V_{\mathrm{sc}}(z)$. For size ratios $q \lesssim 0.3$ on the other hand, the approximation $s_{\max} \to \infty$ in Eqs. (2.22), (2.23) and (2.24) for the effective force can be made, thereby also allowing us to derive a simple, accurate, and analytic form for the interaction potential between a star polymer and a colloid, given by Eq. (2.26). These results form the basis of the statistical-mechanical treatment of star polymer-colloid mixtures in terms of standard liquid-state theories; the availability of analytical results for the pair interactions greatly facilitates the latter.

As the ultimate goal of the derivation of the interactions we present here is precisely to allow theoretical investigations of star polymer-colloid mixtures, we present in the next section a short account of a revision of the star-star interaction and arguments for a modified interaction for the case of very low arm numbers. In this way, mixtures containing stars with arbitrary arm numbers, ranging from free chains ($f = 1, 2$) to the "colloidal limit" of $f \gg 1$ can be studied in full generality.

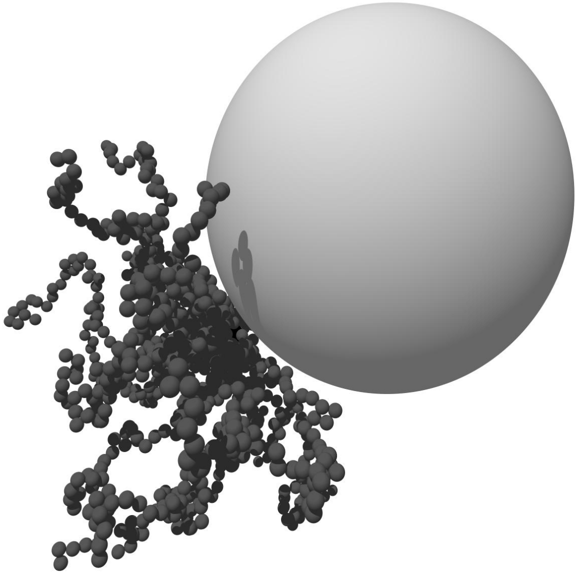

Figure 2.7: Snapshot of a typical configuration of a star polymer with $f = 18$ arms near a colloidal sphere with $q = 0.75$. One should notice that predominantly the inner region of the star interacts with the hard sphere, yielding the main contribution of the inner core regime to the osmotic pressure of a region, determined by $\theta_{\max} \approx 30^o$. Thereby, the upper integration limit $s_{\max}$ in Eq. (2.20) is limited, see also the geometrical aspects of Eq. (2.21) and Fig. 2.3.

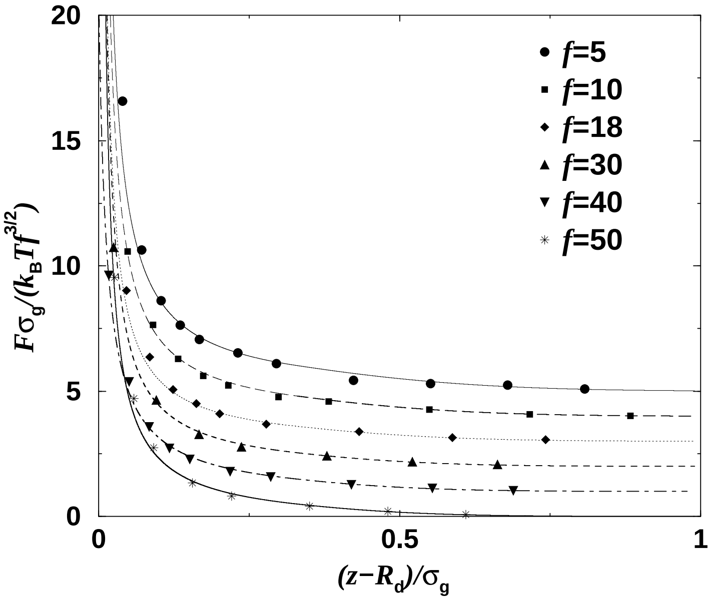

Figure 2.8: The effective force between a star polymer and a colloid for different arm numbers f and $q = 0.33$ plotted against z, the distance of the star center to the surface of the colloid. The lines are the theoretical and the symbols the simulation results. For clarity, the data have been shifted upwards by constants: $f = 10 : 1$, $f = 18 : 2$, $f = 30 : 3$, $f = 40 : 4$, $f = 50 : 5$.

2.2 Effective interactions between star polymers

The effective interaction between two stars in a good solvent was recently derived by theoretical scaling arguments and verified by neutron scattering and molecular simulation [25, 28, 29, 26], leading thereafter to the phase diagram of the system [82, 83]. The pair potential was modeled by an ultrasoft interaction which is logarithmic for an inner core and shows a Yukawa-type exponential decay at larger distances [25, 82]:

$$V_{\mathrm{ss}}(r) = \frac{5}{18} k_{\mathrm{B}} T f^{3/2} \begin{cases} -\ln(\frac{r}{\sigma_{\mathrm{s}}}) + \frac{1}{1+\sqrt{f}/2} & \text{for } r \leq \sigma_{\mathrm{s}}; \\ \frac{\sigma_{\mathrm{s}}/r}{1+\sqrt{f}/2} \exp(-\frac{\sqrt{f}}{2\sigma_{\mathrm{s}}}(r-\sigma_{\mathrm{s}})) & \text{for } r > \sigma_{\mathrm{s}}, \end{cases} \tag{2.34}$$

However, the theoretical approach giving rise to Eq. (2.34) does not hold for arm numbers $f \lesssim 10$, because the Daoud-Cotton model of a star [67], on which the Yukawa decay rests, is not valid for small f. In these cases, the interaction has to a shorter-ranged decay for $r > \sigma_{\mathrm{s}}$. The shortcomings of the blob model can be made evident if one considers the extreme limit $f = 1$, corresponding to free chains. There, the geometrical blob picture and the associated "cone approximation" [84] break down. It is therefore instructive to consider known results about the effective interactions between free chains in order to obtain some insight for the case at hand.

Most of the work done on chain-chain interactions concerns the effective potential between the centers of mass of the chains [63, 65, 85, 86, 87]. Theoretical approaches considering two chains [87], simulations of two chains [85, 86], as well as recent, state-of-the-art simulations of many-chain systems [63, 65] all reach the conclusion that the effective center-of-mass to center-of-mass interaction has a Gaussian form with its range set by the radius of gyration of the chains. Here, we are interested in a slightly different interaction, namely that between the end-monomer of one chain and the end-monomer of the other. However, at distances of the order of R_{g} or larger, whether the centers of mass or the end-monomers choice of the two chains are held fixed should not make much difference. Therefore, we assume a Gaussian decay of the star-star potential for small f-values and center-to-center distances larger than σ_{s}. We emphasize that *only* the large distance decay of the interaction is affected; its form at close approaches has to remain logarithmic [72]. Accordingly, we propose the following star-star pair potential for arm numbers $f < 10$, replacing the Yukawa by a Gaussian decay:

$$V_{\mathrm{ss}}(r) = \frac{5}{18} k_{\mathrm{B}} T f^{3/2} \begin{cases} -\ln(\frac{r}{\sigma_{\mathrm{s}}}) + \frac{1}{2\tau^2\sigma_{\mathrm{s}}^2} & \text{for } r \leq \sigma_{\mathrm{s}}; \\ \frac{1}{2\tau^2\sigma_{\mathrm{s}}^2} \exp\left(-\tau^2(r^2-\sigma_{\mathrm{s}}^2)\right) & \text{for } r > \sigma_{\mathrm{s}}, \end{cases} \tag{2.35}$$

where $\tau(f)$ is a free parameter of the order of $1/R_{\mathrm{g}}$ and is obtained by fitting to computer simulation results, see Fig. 2.9. The values for τ are shown in Table 2.1. For $f = 2$ we obtain the value $\tau = 1.03$ which, together with the potential in Eq. (2.35) above yields for the second virial coefficient of polymer solutions the value $B_2/R_{\mathrm{g}}^3 = 5.59$, in agreement with the estimate $5.5 < B_2/R_{\mathrm{g}}^3 < 5.9$ from renormalization group and simulations [65]. For $f = 5$

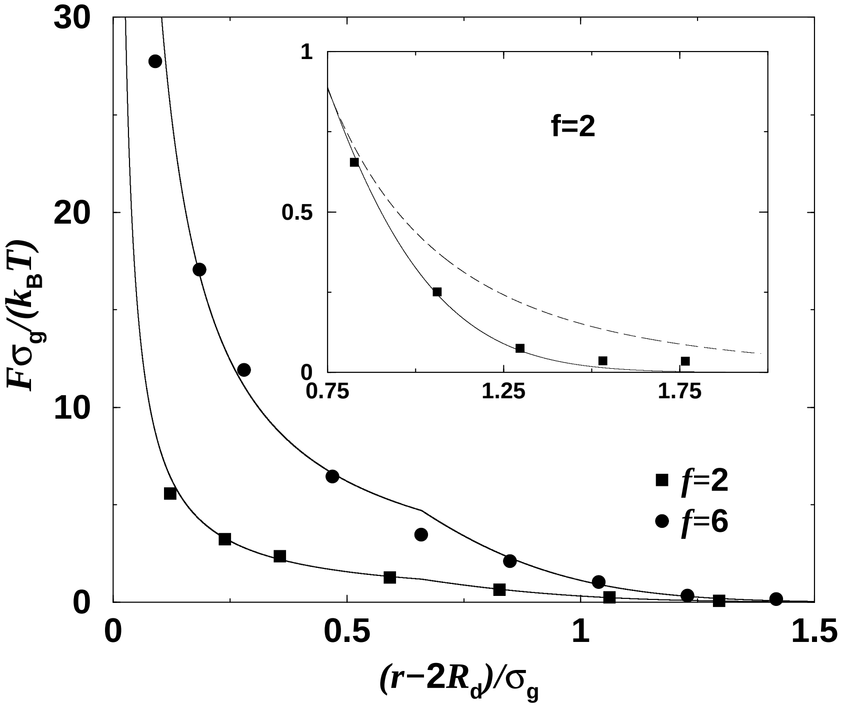

Figure 2.9: Effective force between two star polymers plotted against the center-to-center distance r for arm numbers $f = 2$ and $f = 6$. The simulation data (symbols) coincide with the logarithmic-Gauss expression (solid lines) of Eq. (2.35). In the inset, the outer distance region is enlarged in order to clearly show the validity of the Gaussian decay in this f-regime (solid line), whereas the Yukawa form (dashed line) produces poor agreement there.

we find $\tau = 1.12$, which leads to $B_2/R_g^3 = 11.48$, in accordance with Monte Carlo (MC) simulation results [88, 89].

The very good agreement between the logarithmic-Gauss-potential of Eq. (2.35) and the simulation data for $f < 10$ can be seen in Fig. 2.9. In the inset of this figure, it can also be seen that the Yukawa decay is way too slow there. Hence, the potential of Eq. (2.34), has a longer range than the true interaction for small f, a property that explains the discrepancies between the simulated and theoretical second virial coefficients based on this potential, which have been reported by Rubio and Freire [89] in their numerical study of low-functionality stars. At the same time, with increasing f, the roles of the Gaussian- and Yukawa-decays are reversed: in Fig. 2.10, we show simulation and theory results for $f = 10$. The original, logarithmic-Yukawa potential brings about better agreement now, as already established by earlier studies on stars with high arm numbers [26, 25, 28]. To summarize, we propose two analytic expressions for the effective star-star potential, valid in complementary regimes of the functionality f. The first one concerns the regime $f \lesssim 10$ with the validity of the logarithmic-Gauss-potential of Eq. (2.35) being established; in the second regime, $f \geq 10$,

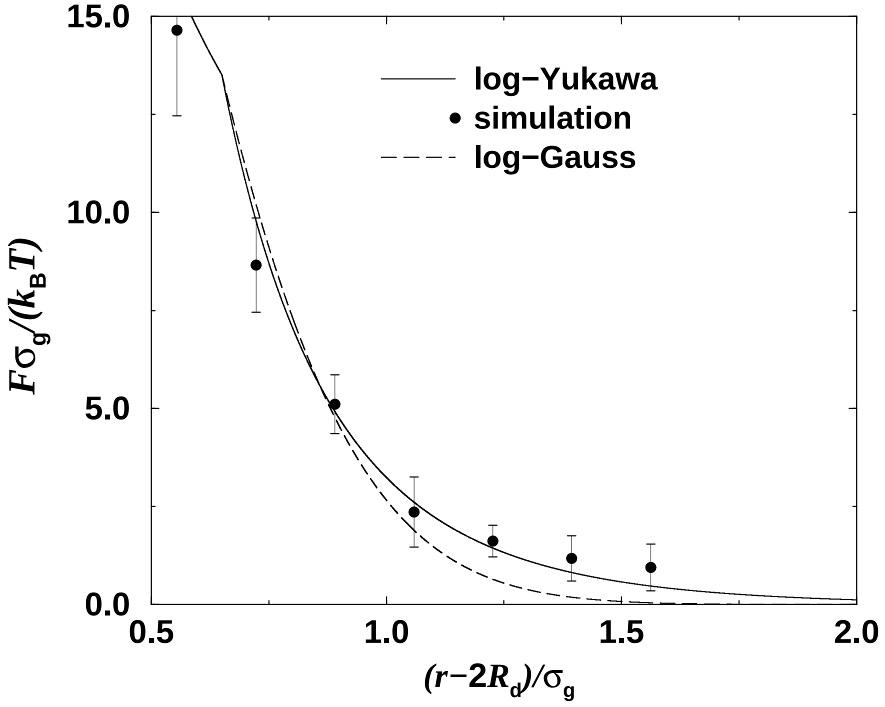

Figure 2.10: Effective force between two star polymers plotted against the center-to-center distance r for arm number $f = 10$. In contrast to Fig. 2.9, here the Yukawa form (solid line) gives an accurate description of the decay of the interaction at large separations, whereas the Gaussian form (dashed line) does not.

the logarithmic-Yukawa-potential of Eq. (2.34) holds. We remark that the ultimative decay of the effective interaction for very long distances is still Gaussian even for very large f, but this is not relevant for B_2 as it occurs for much larger distances than the corona diameter.

2.3 Summary and concluding remarks

In summary, we have presented analytic results for the force between a colloid and a star polymer in a good solvent, accompanied with an analytic expression for the corresponding pair potential which is valid for size ratios $q \lesssim 0.7$. The validity of these expressions was established by direct comparison with Molecular Dynamics simulations. It should be noted that our theoretical approach is in principle generalizable to arbitrary geometrical shapes for the hard particle, thus opening up the possibility for studying effective forces between stars and hard ellipsoids, platelets etc. Further, a revised form for the star-star interaction for small functionalities has been presented, while at the same time the logarithmic-Yukawa form of this interaction remains valid for functionalities $f \gtrsim 10$.

In our considerations we limited ourselves to the case where the star is smaller than the colloid, i.e., $q < 1$. The study of the inverse case may be possible by applying the ideas presented here, however additional complications arise through the possibility of the star to "surround" the smaller, colloidal particle, in which case one part of each arm acts to bring about a repulsion with the colloid and another causes an effective attraction between the two. Furthermore, a pair potential picture for the many-body system become more and more questionable for larger q as effective many-body forces [32] will play a more dominant role in this case.

The present results now enable us to study the structural and thermodynamic properties of concentrated star polymer-colloid mixtures. This is the topic of the next chapter, where the calculation of the structure and the phase behavior of star-polymer–colloid mixtures is presented for a wide range of arm numbers and size ratios.

Chapter 3

Phase behavior of star-polymer–colloid mixtures

Having derived and presented the effective interactions in star-polymer–colloid mixtures in the previous chapter we now proceed with the calculation of their thermodynamic properties using the relevant pair potentials as input. In the first part we present a full two-component description of the mixture yielding binodals for the fluid-fluid demixing transition and a comparison with experimental results. Further, different methods of mapping onto an effective one-component system are discussed and compared to eventually obtain depletion potentials between the colloids. Using these we trace out the complete phase diagrams of the mixture for various combinations of star arm numbers f and star-colloid size ratios q. The resulting phase diagrams are presented and a comparison between the two- and one-component descriptions is made. We systematically investigate the consistency between the one- and two-component descriptions, since our starting point are the three interaction potentials acting between the two components.

3.1 Two-component description

We start with the description of the full two-component mixture of star-polymers and hard spherical colloids using the effective interactions introduced and derived in the previous chapter. We consider a binary system with N_c colloidal spheres of diameter σ_c (radius R_c) and N_s star polymers, characterized by a diameter of gyration σ_g (radius of gyration R_g) and an arm number f. The total particle number is $N = N_\mathrm{c} + N_\mathrm{s}$. Let $q \equiv \sigma_\mathrm{g}/\sigma_\mathrm{c}$ be the size ratio and $\rho_\mathrm{c} \equiv N_\mathrm{c}/V$ and $\rho_\mathrm{s} \equiv N_\mathrm{s}/V$ the number densities of the colloids and stars, respectively. We now define the packing fractions

$$\eta_\mathrm{c} = \frac{\pi}{6}\rho_\mathrm{c}\sigma_\mathrm{c}^3 \tag{3.1}$$

of the colloids, and

$$\eta_\mathrm{s} = \frac{\pi}{6}\rho_\mathrm{s}\sigma_\mathrm{g}^3 \tag{3.2}$$

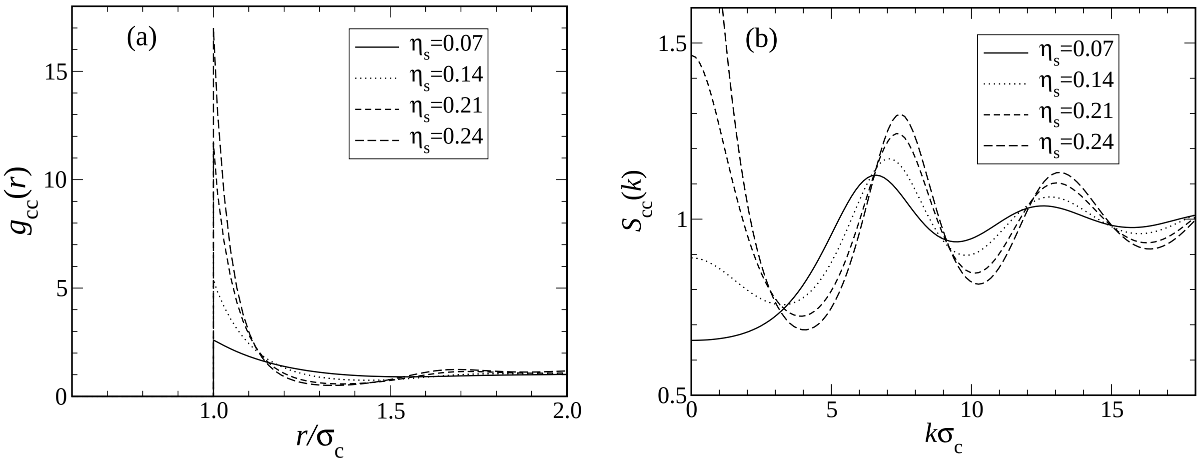

Figure 3.1: (a) Radial distribution functions and (b) static structure factors for the colloids, obtained by the OZ-equations for binary mixtures closed with the RY-closure. Shown are examples for arm number $f = 32$, size ratio $q = 0.5$ and a fixed colloid packing fraction $\eta_c = 0.1$, while the star polymer packing fraction η_s is increased. For η_s the system is in the immediate vicinity of the spinodal line marked by the divergence of the $k \to 0$ limit of the corresponding structure factor.

of the stars in the volume V.

Access to the thermodynamics of the mixture is obtained by solving the Ornstein-Zernike (OZ) equations for binary mixtures using the two-component Rogers-Young (RY) closure. The RY form is reliable for the one component star polymer system [83] and shows a spinodal instability in highly asymmetric hard sphere mixtures [90]. A brief outline regarding integral equation theories for multicomponent mixtures is given in Appendix A. The RY-closure [Eqs. (A.2) - (A.6)] for the two-component mixture, using the interactions given by Eqs. (2.1), (2.26), (2.34), and (2.35) as inputs, was numerically solved by using the Picard-method. Monte Carlo simulations using the same interactions as inputs and measuring the structure factors at selected thermodynamics points, yielded excellent agreement with the RY closure. In our work the thermodynamic consistency of the RY closure was enforced with a single adjustable parameter α; a simple scaling of the form $\alpha_{ij} = \alpha/\sigma_{ij}$, $(i, j = \mathrm{c}, \mathrm{s})$ with $\sigma_{ij} = (\sigma_i + \sigma_j)/2$ showed only small differences compared to the unscaled form.

The structure of the binary mixture is described by the three partial static structure factors $S_{ij}(k) = \delta_{ij} + \sqrt{\rho_i \rho_j}\tilde{h}_{ij}(k)$, with $i, j = \mathrm{c}, \mathrm{s}$. Indication of a demixing transition is the divergence of all structure factors at the long wavelength limit $k \to 0$, marking the *spinodal line* of the system. An example of a diverging structure factor is plotted in Fig. 3.1 together with the corresponding radial density distribution $g_{\mathrm{cc}}(r)$. For a fixed arm number $f = 32$, size ratio $q = 0.5$ and colloid density $\eta_c = 0.1$ we plot the colloid correlation functions for increasing star polymer packing fraction. As can be seen in Fig. 3.1(a), the rising contact value $g_{\mathrm{cc}}(\sigma_c)$ signals an effective attraction between the colloids, induced by the star polymers. This is a signature of the depletion effect, to be discussed in detail below. Further increasing of the star-density, forces the system to develop long-range fluctuations and eventually to demix, as witnessed by the divergence of the low k-values in of the structure factor in Fig. 3.1(b).

In order to calculate the binodal lines, it is more convenient to consider the concentration structure factor, $S_{\text{con}}(k)$, which is a linear combination of the three partial structure factors. The concentration structure factor is defined as

$$S_{\text{con}}(k) = x_{\text{s}}^2 S_{\text{cc}}(k) + x_{\text{c}}^2 S_{\text{ss}}(k) - 2x_{\text{c}} x_{\text{s}} S_{\text{cs}}(k), \tag{3.3}$$

with the concentrations $x_i = N_i/N$, $(i = \text{c}, \text{s})$. The approach to thermodynamics is then given through the sum rule [90, 91]:

$$\lim_{k \to 0} S_{\text{con}}(k) = k_{\text{B}} T \left[\frac{\partial^2 g(x_{\text{s}}, P, T)}{\partial x_{\text{s}}^2} \right]^{-1}, \tag{3.4}$$

where $g(x_{\text{c}}, P, T) = G(x_{\text{c}}, N, P, T)/N$ is the Gibbs free energy $G(x_{\text{c}}, N, P, T)$ per particle and P denotes the pressure of the mixture. In order to simplify the notation, we set $x \equiv x_{\text{s}}$; clearly, $x_{\text{c}} = 1 - x$. We solved the OZ-equations for different combinations of the parameters f and q covering a wide range in the density plane $(\eta_{\text{c}}, \eta_{\text{s}})$. Once the concentration structure factor, Eq. (3.4), is known as function of x for a fixed pressure the Gibbs free energy can be calculated by two simple integrations. In Fig. 3.2(a), an example for the second derivative $g''(x)$ is plotted for constant pressure $\bar{P} \equiv \beta P \sigma_{\text{c}}^3 = 28$, arm number $f = 2$ and size ratio $q = 0.5$. The Gibbs free energy is then obtained by integrating $g''(x)$ along isobars. If $g(x)$ has concave parts, (i.e., if $g''(x) < 0$ for some x-region), the system phase-separates and the boundaries are calculated by the common tangent construction on the $g(x)$ vs. x curves. This common-tangent construction guarantees that partial chemical potentials of every component have the same value on both coexisting phases. As it is performed on an isobar, and for fixed temperature, the pressure and temperature are also the same between two phases and all conditions for phase coexistence are fulfilled.

The constants of integration for the calculation of $g(x)$ through the differential equation (3.4) are determined by formulating a boundary-value problem as follows. Since the Gibbs free energy is an extensive function but in its list of natural variables (N, P, x, T) only one extensive variable (N) appears, Euler's theorem asserts that the function $g = G/N$ must have the form [2]:

$$g(x) = (1 - x)\, \mu_{\text{c}}(x) + x\, \mu_{\text{s}}(x), \tag{3.5}$$

where we omitted P and T from the argument list, as we are working at fixed T along an isobar. If no stars are present in the system $(x = 0)$ the Gibbs energy per particle reduces to the chemical potential of hard spheres at the given pressure P. To determine this, we apply the Carnahan-Starling [92] expressions for the pure hard-sphere equation of state. If no colloids are present $(x = 1)$, the Gibbs free energy per particle is equal to the chemical potential of the stars at the said pressure P. To determine the chemical potential of the stars for a given pressure, we calculated the equation of state of a pure star-polymer system with the one-component OZ-equation closed with RY. For $f = 2$, where the star-star interaction potential is ultrasoft, it is accurate to employ a mean-field approximation [93, 94, 95, 96, 97] (MFA) for the direct correlation function of the polymers, $c_{\rm ss}(r) = -\beta V_{\rm ss}(r)$, where $\beta = (k_B T)^{-1}$. For larger arm numbers the MFA becomes less accurate. In the MFA, use of the compressibility sum rule leads to the simple, quadratic expression for the excess Helmholtz free energy $F_{\rm ex}$ of the star-polymer system [96]:

$$f_{\rm ex} \equiv \frac{\beta F_{\rm ex}}{V} = \frac{\rho_{\rm s}^2}{2} \int \beta V_{\rm ss}(r)\, {\rm d}^3 r \equiv \frac{1}{2} \beta \tilde{V}_{\rm ss}(0) \rho_{\rm s}^2, \tag{3.6}$$

with the Fourier transform $\tilde{V}_{\rm ss}(k)$ of the function $V_{\rm ss}(r)$. From Eq. (3.6) above, we obtain the excess star chemical potential $\beta\mu_{\rm s,ex} = \partial f_{\rm ex}/\partial\rho_{\rm s} = \beta\tilde{V}_{\rm ss}(0)\rho_{\rm s}$ and the total star chemical potential in the MFA as

$$\beta\mu_{\rm s} = \ln\left(\rho_{\rm s}\sigma_{\rm g}^3\right) + \beta\tilde{V}_{\rm ss}(0)\rho_{\rm s}. \tag{3.7}$$

Through the procedure described above, the boundaries $g(x = 0)$ and $g(x = 1)$ are known for every pressure P and an accurate integration of $g''(x)$ can be performed. Once the exact free energy is known, all other quantities of interest can be calculated, for instance the partial chemical potentials $\mu_{\rm c}(x)$ and $\mu_{\rm s}(x)$ of colloids and stars, respectively, which are needed to perform the mapping of the phase diagrams from the two-component to the one-component description in section 3.2. Examples of so-determined partial chemical potentials are shown in Fig. 3.2(b). Some technical details on the solution of the differential equation (3.4) are presented in Appendix B.

Inside the spinodal line, the limits $S_{ij}(k \to 0)$ attain nonphysical, negative values associated with the physical instability of the mixture against phase separation. Consequently, a solution of the integral equations is not possible there, and above the critical pressure P^*, the concentration structure factor $S_{\rm con}(x, k = 0)$ is unknown in some interval $\Delta x(P)$. In the example of Fig. 3.2(a), the interval is $0.9 < x < 0.95$. Thus, it is necessary to interpolate $S_{\rm con}(x, k = 0)$ to obtain the second derivative $g''(x)$ for all x, and this is shown as a solid line in in Fig. 3.2(a). This way, the integration of Eq. (3.4) can be performed. We emphasize that the interpolation is simply done in order to facilitate the integration. The resulting binodal lines are independent of the precise interpolation scheme, as long as the integral equation theories are capable of reaching the precise spinodal, i.e., the points in which the $k \to 0$-limit of the structure factor diverges. Since this is not strictly the case, and sometimes we have to stop slightly before the spinodal is reached, there are small inaccuracies induced by the interpolation procedure that grow with the width of the interval Δx where no solutions of the integral equation theories can be found. In the vicinity of the critical point $\eta_{\rm c}^* \simeq 0.3$, the missing interval Δx is very small and the interpolation is reliable. Here the binodals should be accurate, while for higher pressures (packing fractions $\eta_{\rm c} < \eta_{\rm c}^*$ and $\eta_{\rm c} > \eta_{\rm c}^*$) the binodals are more approximate but show reasonable behavior. For highly asymmetric systems ($q \lesssim 0.18$) it becomes more and more difficult to get solutions of the integral equations in the vicinity of the spinodal line and the calculation of binodals is not possible.

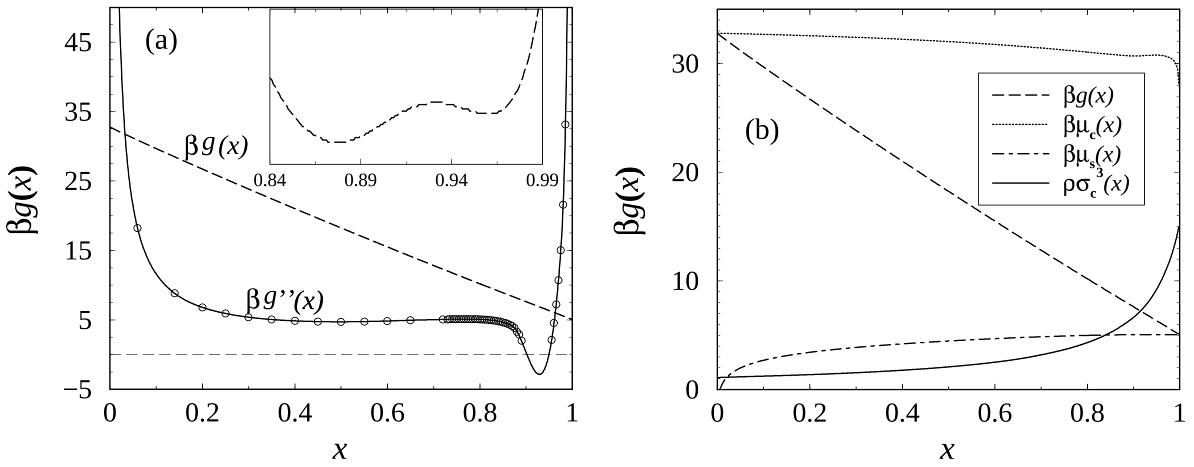

Figure 3.2: (a) Example of the Gibbs free energy $g(x)$ (dashed line) plotted against the star polymer concentration $x = x_{\mathrm{s}}$ in star-polymer colloid mixtures for $f = 2$, size ratio $q = 0.5$ and a fixed pressure $\bar{P} = 28$. $g(x)$ is obtained from integration of the differential equation (3.4), where $S_{\mathrm{con}}(k = 0, x)$ is calculated from the OZ-equations (circles). The second derivative $g''(x)$ is interpolated by a cubic spline interpolation (solid line). The inset shows $g(x)$ after subtracting a linear function, and demonstrates the convex/concave parts of this function. (b) Partial chemical potentials of the colloids $\mu_{\mathrm{c}}(x)$ and of the stars $\mu_{\mathrm{s}}(x)$, plotted against the star concentration x for the same parameters as in (a). At the boundaries of $x = 0$ and $x = 1$, $g(x)$ (dashed line) is equal to the chemical potentials of colloids and stars, respectively. In (b), the total density $\rho\sigma_{\mathrm{c}}^3(x)$ along the isobar is plotted as well.

Let us give a brief outline of the experimental framework used to measure the phase boundaries of the demixing transition in the fluid phase. The experimentalists [98] studied two sets of star polymer-colloid mixtures consisting of poly (methylmethacrylate) (PMMA) particles and poly(butadiene) (PB) star polymers with size ratios $q \approx 0.49$ and $q \approx 0.18$, respectively. PMMA particles were synthesized following a standard procedure [99]. Stock suspensions were prepared either in cis-decahydronaphthalene (cis-decalin) or cis-decalin/tetrahydronaphthalene (tetralin) mixture as an index-matched solvent. These systems have been established as hard sphere models [12]. The volume fraction η_{c} was calibrated using the onset of the hard sphere freezing transition, taken to be at $\eta_{\mathrm{c}} = 0.494$ and observed as the nucleation of iridescent colloidal crystals. The PB star polymers were prepared by anionic polymerization following an established procedure [100, 101]. Star arms were synthesized by polymerizing butadiene with secondary butyl lithium as initiator. The resulting living polymer chains were coupled to the chlorosilane linking agent having ideally 6, 16 and 32 Si-Cl-groups. The molecular weights M_{w} of the PB arms were adjusted to give star polymers with values of $\langle R_{\mathrm{g}}^2\rangle^{1/2} = 0.0172 M_{\mathrm{w}}^{0.609} f^{-0.403}$ [102] as close to 50 nm as possible. A linear

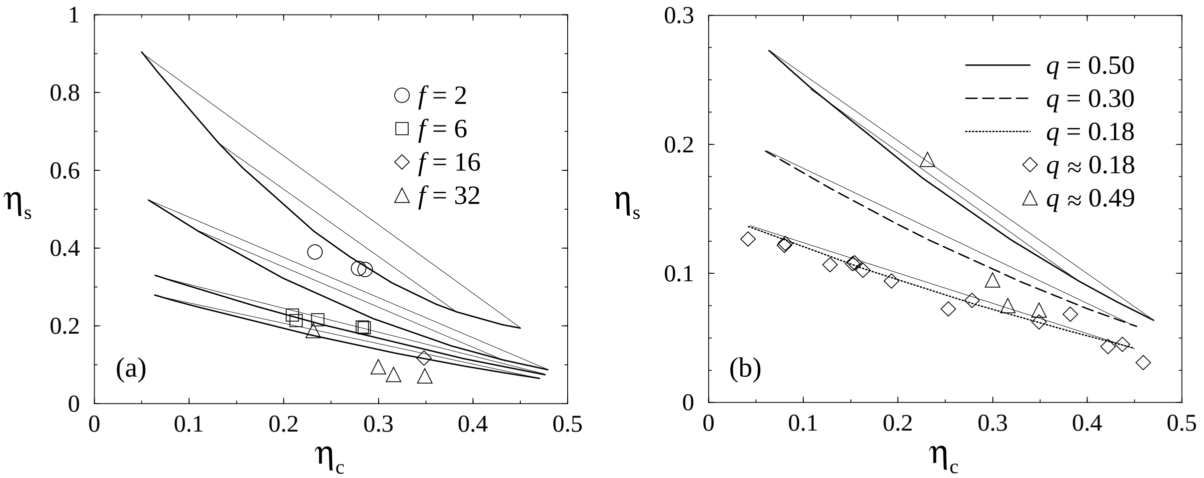

Figure 3.3: (a) Binodals for the mixing-demixing transition in star polymer-colloid mixtures for different arm numbers $f = 2, 6, 16, 32$ (from top to bottom) and size ratio $q \approx 0.49$. Symbols mark experimental results compared with theory (lines) for $q = 0.50$. The thin straight lines are tielines. (b) Same as in (a) for an arm number $f = 32$ and different size ratios q.

PB polymer ($f = 2$) was prepared as a reference system. The particles and star polymers were characterized using light and small angle neutron scattering (SANS) [103]. The results are summarized in Table 3.1. Samples were prepared by mixing PMMA suspensions with PB stock solutions. Each sample was homogenized by prolonged tumbling and allowed to equilibrate and observed by eye at room temperature $T = 25\,^\circ\mathrm{C}$ [104]. In all samples with $q \approx 0.49$, addition of polymer to suspensions with $\eta_c \sim 0.1 - 0.4$ brought about, successively, phase separation into colloidal gas and liquid (or demixing), triple coexistence of gas, liquid and crystal, and gas-crystal coexistence. In samples with $q \approx 0.18$, addition of polymer first led to fluid-crystal coexistence; a metastable gas-liquid binodal buried inside the equilibrium fluid-crystal coexistence region was encountered at higher polymer concentrations [105]. In all cases, demixing started within several hours, crystallization within two days.

The results in Figs. 3.3(a) and (b) show that theory and experiment are in good agreement. This is brought about *without* the use of any free parameters in the former, that would allow for a rescaling of sizes or densities. In particular, the same trends are found as functions of the system parameters f and q. By increasing f at fixed q (Fig. 3.3(a)), the demixing transition moves to lower star packing fractions η_s and the curves become flat. The most important observation from the results shown in Fig. 3.3(a) is that the $f = 2$ and $f = 32$ mixtures show qualitatively the same phase behavior, i.e., a phase diagram with gas-liquid coexistence. From this point of view, a colloid + 32-arm star mixture still resembles a simple colloid polymer mixture rather than BHS. However, it is surprising that the phase boundary *drops* with increasing star functionality. Apparently, therefore, 32-arm

Monomer	f	$M_\mathrm{w} \cdot 10^{-6}$[g/Mol]$^{a)}$	R_c[nm]$^{b)}$	R_g[nm]$^{a)}$
PMMA	-	-	104.0± 2.5	-
PMMA	-	-	289.0± 4.5	-
PB	2	0.86 ± 0.36	-	51.0 ± 3.5
PB	6	1.51 ± 0.06	-	52.1 ± 0.6
PB	16	3.45 ± 0.27	-	51.1 ± 0.5
PB	32	5.11 ± 0.39	-	51.4 ± 0.5

$^{a)}$ small angle neutron scattering (SANS)
$^{b)}$ static light scattering (SLS)

Table 3.1: Molecular characteristics of PMMA particles and PB star polymers.

stars are more efficient depletants than linear polymers.

When q is decreased but f remains fixed (Fig. 3.3(b)), again a motion of the binodals to lower η_s is observed. This trend is *opposite* to the one predicted by the AO model (see Figs. 2(e)-(f) in Ref. [12].) The phase separation is not a simple hybrid between the AO and the hard sphere mixture but show a novel behavior which one could trace back to non-additivity. A careful mapping of the current system into a nonadditive mixture would therefore be of interest. Yet, in view of the fact that the star-star and the cross interactions display soft tails, such a mapping is not straightforward and attempts in this direction are the subject of current investigations. The absolute thermodynamic stability of the liquid phase will be influenced by the competing crystal phases that may preempt the demixing transition. Here, the exciting possibility opens up, that for size ratios $q \gtrsim 0.5$ and $f > 32$, colloid-star superlattices similar to those seen in the BHS may be stable, whereas for smaller size ratios and/or functionalities the crystals would be of the 'sublattice-melt' type. In this context, it may be significant that stars crystallize only when $f > 34$ [82].

Since the chemical potential of the stars in both coexisting phases is the same, it is possible to imagine now that both are brought into partial contact with a reservoir of stars, in which the stars have this common value of the chemical potential. The word 'partial' here means that the contact is assumed to materialize through a semi-permeable membrane that allows the passage of star-polymers but not of colloids through it. Let $\eta_\mathrm{s}^\mathrm{r}$ be the packing fraction of the star-polymers in the reservoir. Since the reservoir *and* the two coexisting phases all have the same value for the partial chemical potential μ_s, it follows that a representation of the phase diagram in the $(\eta_\mathrm{c}, \eta_\mathrm{s})$-plane can be transformed, without loss of information, into the $(\eta_\mathrm{c}, \mu_\mathrm{s})$- or, equivalently, the $(\eta_\mathrm{c}, \eta_\mathrm{s}^\mathrm{r})$-plane. A comparison to the effective one-component description results where the phase diagrams are plotted in the $(\eta_\mathrm{c}, \eta_\mathrm{s}^\mathrm{r})$-plane will be shown in the next section.

3.2 Mapping onto an effective one-component system

In this section we proceed with a mapping of the two-component mixture onto an effective one-component system of colloids only, in which the star-polymers have been traced out. The result of this integration is an effective colloid-colloid interaction in which the bare, hard-sphere potential of Eq. (2.1) is 'dressed' by a depletion interaction that has its origins on the star polymers. The star-star and star-colloid interactions enforce spatial correlations of the latter when they are brought close to two colloidal hard spheres held at separation $\boldsymbol{R}_{12}$ from one another, and it is precisely these correlations that determine the form of the depletion potential. We thus present different methods in obtaining the depletion potential and compare between those.

3.2.1 Monte Carlo Simulation

The most accurate way to calculate the effective interaction between two colloids in presence of the star polymers is to employ direct computer simulations [106, 107, 108, 109, 110]. To this end, we placed two colloidal particles with coordinates $\boldsymbol{R}_1$ and $\boldsymbol{R}_2$ along the body diagonal of a cubic simulation box of volume V, symmetrically around their center of mass that coincided with the cube center. Thus $\boldsymbol{R}_{12} = \boldsymbol{R}_2 - \boldsymbol{R}_1$ is the vector connecting the sphere centers and $R_{12} = |\boldsymbol{R}_{12}|$ is the mutual separation distance of the colloids. In addition, we introduced $N_{\rm s}$ star polymers in the same box. As there are only two colloidal spheres, we are dealing with the limit $\rho_{\rm c} \to 0$, therefore the packing fraction $\eta_{\rm s} = (\pi/6)(N_{\rm s}/V)\sigma_{\rm g}^3$ of the stars in the box can be identified with the reservoir packing fraction $\eta_{\rm s}^{\rm r}$ introduced in the preceding section.

We performed standard NVT-Monte-Carlo simulations [75], holding the positions of the colloidal spheres fixed and taking statistics on the stars, for various different separations R_{12} between the colloids. We employed the pair potentials given by Eqs. (2.34) and (2.35) for the interaction between the stars (depending on their arm number) and by Eq. (2.26) for the interaction between stars and colloids. Due to the second colloid, the radial symmetry of the density distribution of the stars around one colloid is broken. A nonvanishing force is now acting on each of the colloid in direction of their connecting vector $\boldsymbol{R}_{12} = \boldsymbol{R}_2 - \boldsymbol{R}_1$, because of depletion or aggregation of the stars between the colloids, dependent of the distance R_{12} between them. The resulting force in directions perpendicular to their connecting vector remains zero. After a sufficiently long equilibration time, the force $\boldsymbol{F}_1$ acting on one of the colloids has been measured by performing the statistical average

$$\boldsymbol{F}_1(R_{12}) = \left\langle - \sum_{j=1}^{N_{\rm s}} \nabla_{\boldsymbol{R}_1} V_{\rm sc}(|\boldsymbol{R}_1 - \boldsymbol{r}_j|) \right\rangle_{\boldsymbol{R}_{12}} . \tag{3.8}$$

In Eq. (3.8) above, $\boldsymbol{r}_j$, $j = 1, 2, \ldots, N_{\rm s}$, stand for the positions of the star polymers, whereas the symbol $\langle \ldots \rangle_{\boldsymbol{R}_{12}}$ denotes a constrained statistical average over the star polymers only, when the two colloids are held at separation $\boldsymbol{R}_{12}$. Due to symmetry, for the force on the second colloid it holds $\boldsymbol{F}_2(R_{12}) = -\boldsymbol{F}_1(R_{12})$ and the magnitude of the depletion force, $F_{\text{dep}}(R_{12})$, is given by:

$$F_{\text{dep}}(R_{12}) = \frac{\boldsymbol{R}_1 - \boldsymbol{R}_2}{R_{12}} \cdot \boldsymbol{F}_1(R_{12}). \tag{3.9}$$

The depletion force acts for distances $R_{12} > \sigma_{\text{c}}$ only; for closer approaches, the bare, HS-interaction takes over. $F_{\text{dep}}(R_{12}) < 0$ denotes attractions between the colloids, mediated by the stars. Indeed, for colloid separations $R_{12} \cong \sigma_{\text{c}}$ such attractions are expected to show up, as in this case the two colloids are hit asymmetrically by the stars from the outside, and the unbalanced osmotic pressure of the latter pushes the hard spheres together. The total effective force acting on the first colloid in the presence of the stars is $\boldsymbol{F}_{\text{eff}}(R_{12}) = \boldsymbol{F}_{\text{HS}}(R_{12}) + \boldsymbol{F}_1(R_{12})$ and can be figured as the gradient of an effective potential that is a sum of the bare, hard-sphere interaction and the *depletion potential* $V_{\text{dep}}(R_{12})$:

$$\begin{aligned} \boldsymbol{F}_1(R_{12}) &= -\nabla_{\boldsymbol{R}_1} V_{\text{eff}}(R_{12}) \\ &= -\nabla_{\boldsymbol{R}_1} \left[V_{\text{cc}}(R_{12}) + V_{\text{dep}}(R_{12}) \right]. \end{aligned} \tag{3.10}$$

In Fig. 4.1, we show representative examples for the resulting depletion force $F_{\text{dep}}(R_{12})$ for various different functionalities and size ratios. The figure shows also a comparison with results of the inversion of OZ-equations, see section 3.2.2 and of the superposition approximation, section 3.2.3. The disadvantage of the use of simulations for calculating depletion forces is the need of many long runs for high resolved curves with good statistics. Referring to this figure, we note that for $f = 2$ we recover essentially the Asakura-Oosawa-result [9], with the depletion force being purely attractive, Fig. 4.1(a). Increasing the star functionality, however, leads to an oscillatory behavior of the effective force, which is caused by the increasingly strong correlation effects between the stars, see Figs. 4.1(b) and (c). This characteristic is akin to the features of the depletion force found in binary hard-sphere mixtures [16, 23]. Star polymers act as depleting agents that interpolate between the linear polymer behavior and the hard-sphere one.

3.2.2 Inversion of the Ornstein-Zernike equation for binary mixtures

An alternative route to the depletion potential, which does not require the use of computer simulations, is offered by the so-called inversion of the full, two-component integral-equation theory-results in the limit of low colloid density [111, 112, 113, 114]. Indeed, it follows from exact diagrammatic expansions in the theory of liquids [36] that the radial distribution function $g(r)$ attains in the low-density limit the form $g(r) = \exp[-\beta v(r)]$, with $v(r)$ denoting the pair potential acting between the constituent species of the fluid. Thereby, the effective potential $V_{\text{eff}}(r)$ acting between the colloids and depending parametrically on the star-reservoir packing fraction $\eta_{\text{s}}^{\text{r}}$ can be obtained by solving the two-component Ornstein-Zernike equations with the Rogers-Young closure for given star packing fraction $\eta_{\text{s}}^{\text{r}}$ and at

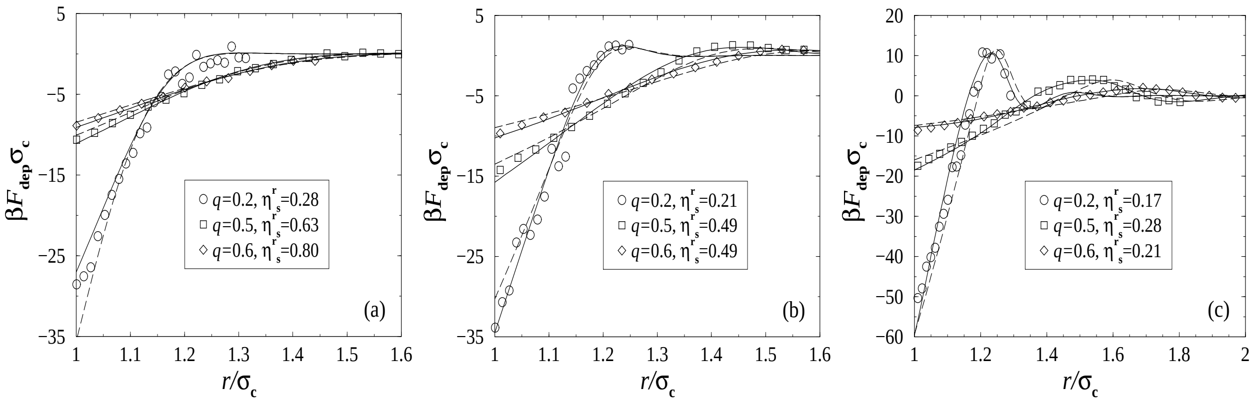

Figure 3.4: Depletion forces for different functionalities f and size ratios q. (a) $f = 2$; (b) $f = 6$; (c) $f = 32$. The symbols denote simulation results, the solid lines the force resulting from the inversion of the RY-closure and the broken lines the results of the superposition approximation. The denoted values of the reservoir star-polymer packing fractions, $\eta_{\rm s}^{\rm r}$, were chosen to be close to the demixing critical point in the fluid phase.

the limit $\eta_{\rm c} \to 0$. The so-obtained colloid-colloid radial distribution function $g_{\rm cc}(r)$ can be then inverted employing the exact relation above and yielding the effective potential as:

$$\beta V_{\rm eff}(r) = -\lim_{\eta_{\rm c}\to 0} \ln[g_{\rm cc}(r;\eta_{\rm c},\eta_{\rm s}^{\rm r})] \tag{3.11}$$

In Fig. 4.1 we show results for the effective force $F_{\rm eff}(r) = -\nabla V_{\rm eff}(r)$ derived from $\beta V_{\rm eff}(r)$ obtained by the procedure outlined above, in comparison with the simulation results of section 3.2.1. Excellent agreement between the two is found, for all (q, f) parameter combinations considered. Small deviations for distances near contact $r \approx \sigma_{\rm c}$ could be corrected by introducing a simple scaling for the consistency parameter $\alpha_{ij} = \alpha/\sigma_{ij}$, $(i, j = {\rm c}, {\rm s})$ with an auxiliary ratio parameter $q' = \sigma_{\rm s}/\sigma_{\rm c} = 0.5$ used for all size ratios q and all arm numbers f.

3.2.3 Superposition approximation

A third way to the depletion potential is offered by the so-called *superposition approximation* (SA) of Attard [115]. If the exact star-polymer density distribution $\rho_s(\boldsymbol{r}_1; \boldsymbol{R}_1, \boldsymbol{R}_2)$ at $\boldsymbol{r}_1$ around two colloids held fixed at positions $\boldsymbol{R}_1$ and $\boldsymbol{R}_2$ were known, then the depletion force in the low-density limit could be calculated by an integration over the contributions of the force between star-polymers and a colloid in direction of $\boldsymbol{R}_{12} = \boldsymbol{R}_2 - \boldsymbol{R}_1$. As a matter of fact, the density $\rho_s(\boldsymbol{r}_1; \boldsymbol{R}_1, \boldsymbol{R}_2)$ is proportional to the three-body, star-colloid-colloid distribution function $g^{(3)}_{\rm scc}(\boldsymbol{r}_1, \boldsymbol{R}_1, \boldsymbol{R}_2)$. Since the latter is in general unknown, in the SA it is factorized as a product of pair distribution functions, as explained below.

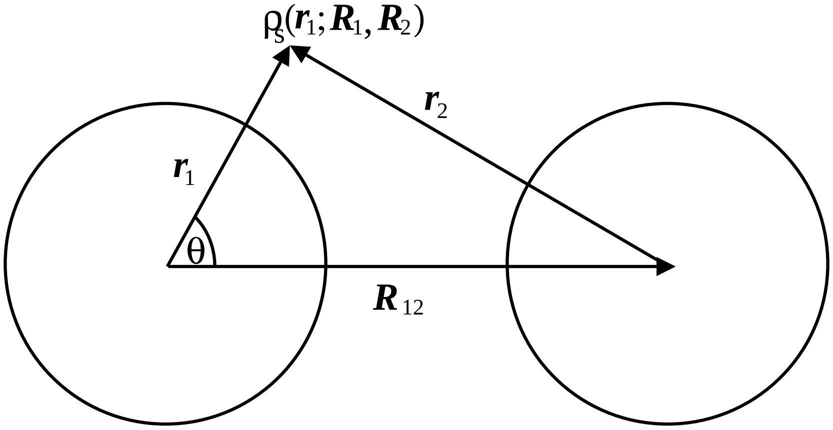

Figure 3.5: A sketch of two colloids in a distance R_{12}. The origin of the coordinates lies in the center of the left sphere. $\rho_\mathrm{s}(\boldsymbol{r}_1;\boldsymbol{R}_1,\boldsymbol{R}_2)$ is the star-polymer density at $\boldsymbol{r}_1$, in the presence of the two colloids at positions $\boldsymbol{R}_1$ and $\boldsymbol{R}_2$.

Let us consider two colloids in a distance R_{12}, as depicted in Fig. 3.5. We put the origin of our coordinate system in the center of one of the two colloids surrounded by star-polymers with density $\rho_s(\boldsymbol{r}_1;\boldsymbol{R}_1,\boldsymbol{R}_2)$. The depletion force acting on the left sphere is given by the general relation, Eq. (3.8). Taking into account that $\nabla_{\boldsymbol{R}_1} V_\mathrm{sc}(|\boldsymbol{R}_1 - \boldsymbol{r}_1|) = -\nabla_{\boldsymbol{r}_1} V_\mathrm{sc}(|\boldsymbol{R}_1 - \boldsymbol{r}_1|)$, setting $\boldsymbol{R}_1 = 0$, performing the statistical average there, and projecting on the $\boldsymbol{R}_{12}$ direction according to Eq. (3.9), we obtain the depletion force as:

$$F_\mathrm{dep}(R_{12}) = -2\pi \int_0^\infty r_1^2 \, \frac{\mathrm{d}V_\mathrm{sc}(r_1)}{\mathrm{d}r_1} \, \mathrm{d}r_1 \int_{-1}^{1} \rho_\mathrm{s}(\boldsymbol{r}_1;\boldsymbol{R}_1,\boldsymbol{R}_2)\, \omega \, \mathrm{d}\omega, \tag{3.12}$$

where $\omega = \cos\theta$.

The superposition approximation amounts to replacing the exact density $\rho_\mathrm{s}(\boldsymbol{r}_1;\boldsymbol{R}_1,\boldsymbol{R}_2)$ of the stars in the presence of the two colloids by the product of the bulk star density $\rho_\mathrm{s}^\mathrm{r}$ times the two radial distribution functions on the stars in the presence of two *isolated* colloids, one with its center at $\boldsymbol{R}_1$ and one with its center at $\boldsymbol{R}_2$. Hence, in the SA one writes:

$$\rho_\mathrm{s}(\boldsymbol{r}_1;\boldsymbol{R}_1,\boldsymbol{R}_2) \approx \rho_\mathrm{s}^\mathrm{r}\, g_\mathrm{cs}(|\boldsymbol{r}_1 - \boldsymbol{R}_1|) g_\mathrm{cs}(|\boldsymbol{r}_1 - \boldsymbol{R}_2|), \tag{3.13}$$

where, evidently, $\rho_\mathrm{s}^\mathrm{r} = (6\eta_\mathrm{s}^\mathrm{r})/(\pi\sigma_\mathrm{s}^3)$ relates the reservoir density and packing fraction. The radial distribution functions $g_\mathrm{cs}(|\boldsymbol{r}_1 - \boldsymbol{R}_i|)$ above relate to a sea of stars in the presence of a single colloid, hence they are readily available by the $\eta_\mathrm{c} \to 0$-limit of the two-component integral equation theories. Noting that $|\boldsymbol{r}_1 - \boldsymbol{R}_2| = |\boldsymbol{r}_2| = \sqrt{R_{12}^2 + r_1^2 - R_{12} r_1 \omega}$, we finally obtain in the SA:

$$F_\mathrm{dep}(R_{12}) = -2\pi\rho_\mathrm{s}^\mathrm{r} \int_0^\infty r_1^2 \frac{\mathrm{d}V_{sc}(r_1)}{\mathrm{d}r_1}\, g_\mathrm{cs}(r_1)\, \mathrm{d}r_1 \int_{-1}^{1} g_\mathrm{cs}\left(\sqrt{R_{12}^2 + r_1^2 - R_{12} r_1 \omega}\right) \omega \, \mathrm{d}\omega. \tag{3.14}$$

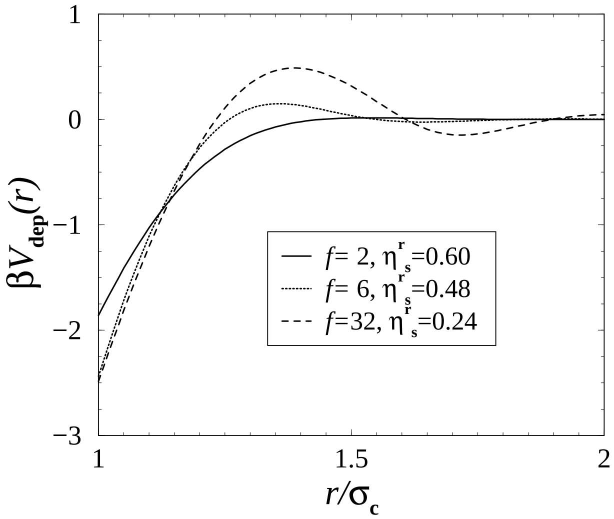

Figure 3.6: Depletion potentials $V_{\mathrm{dep}}(r)$ for the colloids obtained by mapping the two-component system on an effective one-component system by inversion of OZ-equations in the low-density limit. We plot the potential for different arm numbers $f = 2, 6, 32$ for star polymer reservoir packing fractions $\eta_{\mathrm{s}}^{\mathrm{r}}$ near the critical point of fluid demixing. The size ratio is $q = 0.5$.

In Fig. 4.1 we show results obtained from this approximation, in comparison to direct simulation results and to the inversion presented in the preceding subsection. It can be seen that superposition approximation reproduces the simulation results in the linear polymer limit, $f = 2$, very well. In this case, the star polymer are very soft, weakly interacting particles. Thereby, the cross-correlations between them arising from the interaction $V_{\mathrm{ss}}(r)$ are so weak that the superposition approximation is valid: the presence of a second colloid results into a density profile for the stars that is very well approximated by the product of those arising from two isolated colloids. However, for larger functionalities, where the star-star interaction starts causing significant correlation effects between them, the resulting depletion interactions and forces from the SA are less accurate. As expected, the SA underestimates the degree of oscillatory behavior of the force; in addition, the phase of those oscillations is in error. Thus, for large arm numbers, the superposition approximation is not an adequate tool for calculating accurately the effective interaction.

3.2.4 Phase diagrams

Due to the shortcomings of the superposition approximation and the accuracy of the inversion of the RY-results, we have resorted to the latter procedure in order to calculate the depletion potential. Some examples of this potential are plotted in Fig. 3.6 for different arm numbers f and reservoir packing fractions $\eta_{\mathrm{s}}^{\mathrm{r}}$ of the stars. Employing this interaction, we proceed with the calculation of the phase diagrams of selected star-polymer–colloid mixtures. The goal is to establish the limits of stability of the demixing transition with respect to the crystallization of the colloids. Thereby, we limited ourselves to the common, fcc-structure for candidate colloidal crystals, which materializes for colloids in the absence of stars ($\eta_{\mathrm{s}}^{\mathrm{r}} = 0$). Though competing crystal structures cannot be rules out a priori, the quantitative features of the depletion potential render the stability of more open crystal structures, such as the bcc-lattice, improbable. For the calculation of the phase diagrams, we combined simulations and perturbation theory, as explained below.

Simulation

In order to determine phase coexistence, it is necessary to calculate the Helmholtz free energy $F = F(N_{\mathrm{c}}, V, \eta_{\mathrm{s}}^{\mathrm{r}})$. An accurate but computational expensive way is to perform thermodynamical integration of Monte Carlo simulation results, using the hard-sphere system as reference; for a detailed description, see Refs. [9] and [16]. The free energy can be integrated as

$$F(N_{\mathrm{c}}, V, \eta_{\mathrm{s}}^{\mathrm{r}}) = F_0(N_{\mathrm{c}}, V, \eta_{\mathrm{s}}^{\mathrm{r}} = 0) + \int_0^1 \mathrm{d}\lambda \left\langle \sum_{i<j}^{N_{\mathrm{s}}} V_{\mathrm{dep}}(r) \right\rangle_{N_{\mathrm{c}}, V, \eta_{\mathrm{s}}^{\mathrm{r}}, \lambda}, \tag{3.15}$$

while using an auxiliary effective interaction $V_{\mathrm{eff}}^{\lambda}(r)$ between the star-polymers and colloids in the simulation:

$$V_{\mathrm{eff}}^{\lambda}(r) = V_{\mathrm{cc}}(r) + \lambda V_{\mathrm{dep}}(r). \tag{3.16}$$

Here, $0 \leq \lambda \leq 1$ is a dimensionless coupling parameter, interpolating between the hard sphere reference interaction ($\lambda = 0$) and the effective potential $V_{\mathrm{eff}}(r)$. For the free energy of the hard sphere reference system, $F_0(N_{\mathrm{c}}, V, \eta_{\mathrm{s}}^{\mathrm{r}} = 0)$, we use the Carnahan-Starling expression [92] for the fluid, and the equation of state proposed by Hall [116] for the solid phase. The calculation for every point on the free energy curve was performed with $N_{\mathrm{s}} = 108$ particles starting with a face-centered-cubic configuration. After fitting polynomials to the function $f(\rho_{\mathrm{c}}) = F/V$, a common tangent construction was employed to obtain the coexistence curves among all phases.

Perturbation theory

A theoretical understanding of the effects of the depletion potential can be reached within the framework of standard perturbation theory, using the hard-sphere system as reference. To first order in perturbation theory, the Helmholtz free energy of a collection of colloids interacting by the hard-sphere plus depletion potentials is given by [36]:

$$\frac{\beta F}{N_{\mathrm{c}}} = \frac{\beta F_0}{N_{\mathrm{c}}} + \frac{1}{2}\beta\rho_{\mathrm{c}} \int g_0(r)\, \phi(r)\, \mathrm{d}^3 r, \tag{3.17}$$

where F_0 and $g_0(r)$ are the free energy and radial pair correlation function of the reference system, and $\phi(r)$ the perturbing potential, $V_{\mathrm{dep}}(r)$ in this case. Barker and Henderson developed a second order term, including two-body correlations [117], and refining thereby the perturbation theory for the free energy into

$$\frac{\beta F}{N_\mathrm{c}} = \frac{\beta F_0}{N_\mathrm{c}} + \frac{1}{2}\beta\rho_\mathrm{c} \int g_0(r)\,\phi(r)\,\mathrm{d}^3r - \frac{1}{4}\left(\frac{\partial\rho}{\partial p}\right)_0 \beta\rho_\mathrm{c} \int g_0(r)\,\phi^2(r)\,\mathrm{d}^3r. \tag{3.18}$$

In Eq. (3.18) above, $(\partial\rho/\partial p)_0$ is the compressibility of the reference system. For the reference free energy F_0, we used the expressions of Carnahan-Starling and Hall, for the fluid and solid phase, respectively. The pair distribution functions $g_0(r)$ are provided by the parametrizations of Verlet and Weis [118] for the fluid phase and Kincaid and Weis [119] for the solid. Free energy calculations using Eq. (3.18) were performed by Dijkstra *et al.* for the effective Asakura-Oosawa pair potential, modeling colloid-polymer mixtures [9] and for the effective one-component system arising by integrating out the small spheres in a binary hard sphere mixture [16]. It was found there that this approach yields excellent agreement for the fluid-solid boundaries compared to thermodynamical integration results.

Results

As far as the star-polymer–colloid mixtures are concerned, we find from the comparison of the Helmholtz free energy calculated from the two different approaches described above, that the two are in excellent agreement as far as the solid branch of the free energy is concerned. This is consistent with the findings in Refs. [9] and [16]. For the fluid branch, though, only the low density range coincide, for larger densities the free energy of the perturbation approach is always too large. This result is consistent with the fact that the first-order perturbation theory arises from the Gibbs-Bogolyubov inequality and hence the resulting free energy can only by larger than the true one. Moreover, in the fluid phase, the hard-sphere radial distribution function $g_0(r)$ severely underestimates the contact value of the true $g(r)$, thus resulting in an internal energy that is significantly higher than the true one at intermediate and high fluid densities. Thus, the Helmholtz free energy of the fluid is overestimated. In view of the inaccuracy of the perturbation theory for the fluid phase, we resorted to the results of the Monte-Carlo simulation, whereas for the solid we employed the perturbation approach, in order to reduce the computational effort. In Fig. 3.7 we plot the phase diagrams for arm numbers $f = 2$, 6, and 32 and size ratios $q = 0.2$, 0.5, and 0.6. For $f = 2$ we obtain phase diagrams that are very similar to the ones obtained for the AO-model [9]. This is interesting since in this work we are dealing with realistic polymer-polymer as well as polymer-colloid interactions, that go beyond the simple approximations of the AO-model. Apparently, the overall features of such mixtures and, in particular, the (meta)stability of the demixing transition are insensitive to the details of the interaction potentials.

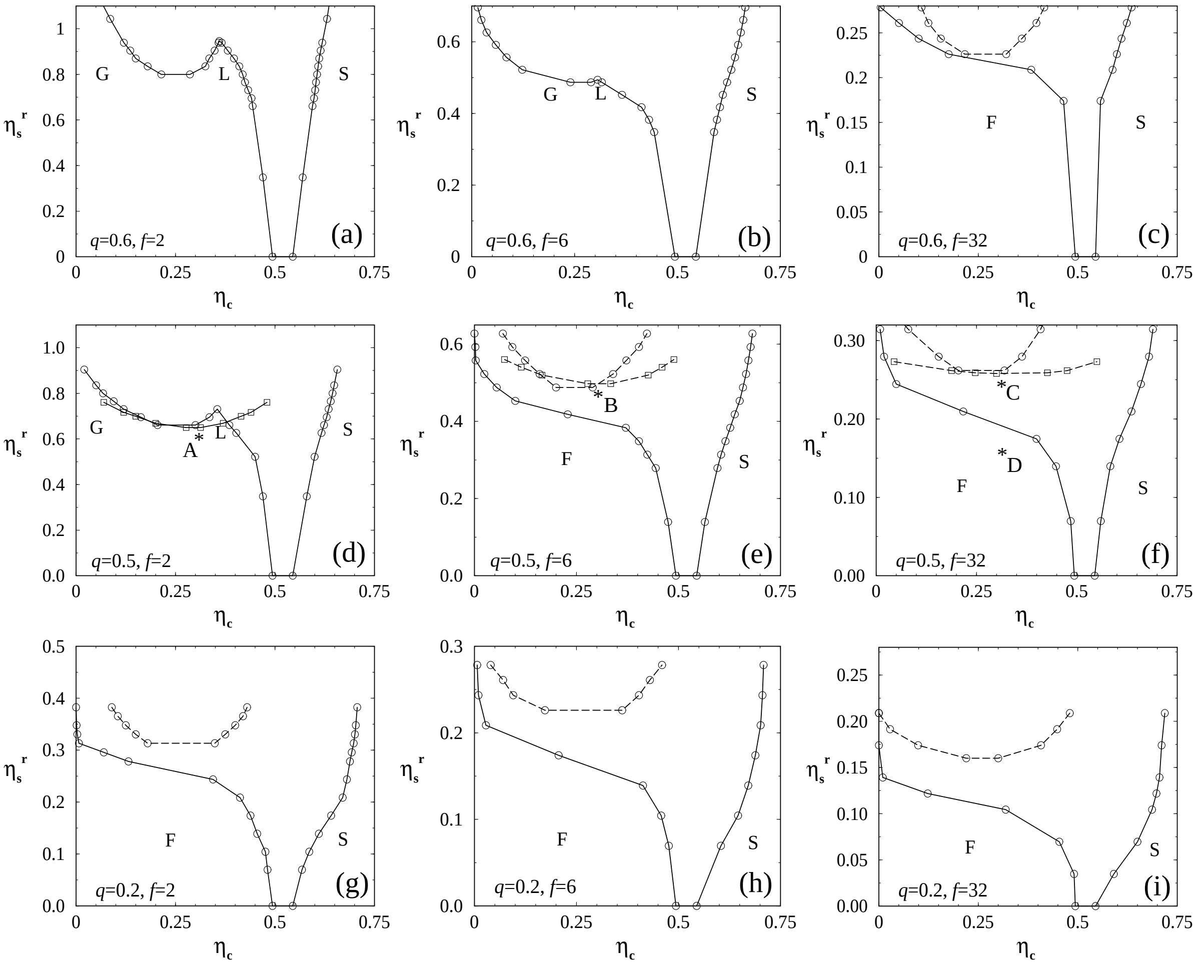

Figure 3.7: Phase diagrams of star-polymer–colloid mixtures for different size ratios and different star functionalities. The circles indicate the calculated phase boundaries from the one-component description, the squares from the full two-component description, see section 3.1. The lines are guide to the eye. The solid lines denote stable phase transitions and the broken ones metastable demixing binodals. The first row shows the phase behavior for a size ratio $q = 0.6$. (a) $f = 2$; (b) $f = 6$; (c) $f = 32$. For $f = 2$ and $f = 6$ the demixing transition in the fluid phase is stable, resulting into three distinct phases: gas (G), liquid (L) and solid (S). For $f = 32$ the freezing transition preempts demixing, resulting into two stable phases: fluid (F) and solid (S). In the second row the phase behavior for $q = 0.5$ is plotted, again the arm number increases from (d) to (f), in analogy to the first row. Now only for $f = 2$ a stable demixing binodal is found. The asterisks denote state points at which pairwise correlation functions were calculated. The last row shows the behavior for $q = 0.2$. No stable fluid-fluid transition is observed for arm numbers $f = 2$ (g), $f = 6$ (h), and $f = 32$ (i).

At size ratio $q = 0.5$, we have a demixing binodal that is only slightly stable, a result in agreement with that of Ref. [9] in which it was found $q_c \cong 0.45$. An increase of the functionality f suppresses the stability of the demixing binodals, a finding which is in line with the general trend that, as f grows, star-polymers become more akin to hard spheres; in a mixture of hard spheres, no demixing takes place [15, 17, 16]. For $f = 6$, a stable demixing binodal appears at larger size ratio, $q = 0.6$, see Fig. 3.7(b). This is to be expected, as for larger f the star-polymers become more akin to hard depletants and hence a depletion force of longer range is necessary in order to bring about phase separation in the fluid phase. For the case $f = 32$ we obtain demixing binodals that are always metastable with respect to freezing, in the domain $q \leq 0.7$ in which the pair potentials are reliable. The results show a clear trend from the AO-type behavior, valid for $f = 2$, to the BHS-behavior, valid for $f = 32$. In view of the fact that the critical value q_c for $f = 6$ seems to lie slightly below 0.6 and is growing with f, we anticipate that star polymers with $f \gtrsim 10$ will not be able to bring about stable demixing transitions in a star-polymer–colloid mixture. For $q = 0.2$, shown in Figs. 3.7(g), (h) and (i), we obtain no stable demixing transitions for any of the three functionalities $f = 2$, 6, and 32 that we checked. At small size ratios, star-polymers are weak depletants, causing an attraction whose range is too short to bring about a thermodynamically stable ‘liquid-gas’ coexistence curve. Our findings are consistent with earlier results on, e.g., the Hard-Sphere-attractive-Yukawa system [120, 121] and other model potentials [122], in which is was found that the liquid disappears when the range of the attractions becomes, roughly, less than 20% of that of the repulsions.

The mapping onto the one-component, depletion-like picture greatly facilitates the calculation of the phase diagrams, in particular in the crystalline state. Nevertheless, performing this mapping remains a matter of convenience: the physics should not depend on the point of view and, in particular, in an exact mapping both the phase boundaries and the correlation functions of the colloids should be identical in both pictures [21]. Since we have employed approximations at various stages, in both the two-component and in the depletion approaches, it is useful to perform a comparison between the two in order to judge their severity. This is the subject of the following section.

3.3 Comparison between the two- and one-component descriptions

The determination of the partial chemical potentials in the full two-component system described in section 3.1 enables us to compare the results obtained there in the (η_c, η_s)- or *system*-representation, with the results obtained in section 3.2.4 in the (η_c, η_s^r)- or *reservoir*-representation. As we can see from Eq. (3.5), the partial chemical potentials of the stars and colloids can be simply obtained by the common tangent construction: the intersection of the tangent with the $x = 0$ or $x = 1$ axis yield the partial chemical potential μ_c or μ_s, respectively. Now, for every two coexistence points in the (η_c, η_s) ensemble we determine

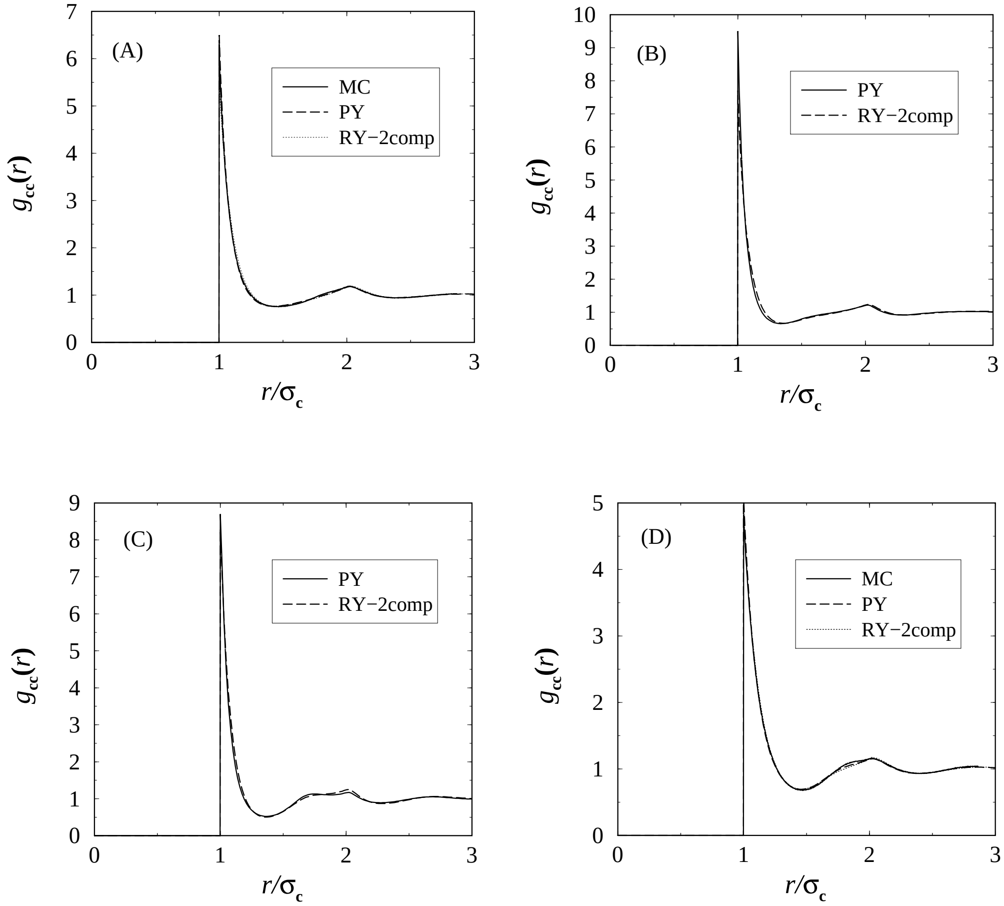

Figure 3.8: Comparison of the pair correlations functions $g_{cc}(r)$ for the colloids at different state points (A)-(D), denoted by the asterisks in the phase diagram for $q = 0.5$ in figure 3.7 (d)-(f). Using the depletion potentials from the one-component description MC simulations (solid lines) are compared to PY results (dashed lines). Dotted lines present RY-results employing the full binary OZ-equations.

the corresponding chemical potential μ_s. The equation of state of the one component star polymer system determined by RY gives us the reservoir packing fraction to every chemical potential. We calculate the transformed curves for a size ration $q = 0.5$ and arm numbers $f = 2$, 6, and 32. The results of the mapping of the coexistence points from the (η_c, η_s)-plane into the (η_c, η_s^r)-plane are shown in Figs. 3.7(d)-(f) together with the fluid-demixing binodals from the one-component approach. Regarding the critical points the agreement is very good. Although many-body terms are neglected in the effective one-component description [9, 21], we find a satisfactory agreement, both for the critical colloid density and for the critical star polymer reservoir density. Away from the critical point, the coexistence lines from the two-component approach are too broad. The farther one is from the critical point, the more difficult it becomes to reach precisely the spinodal of the mixture and then the numerical

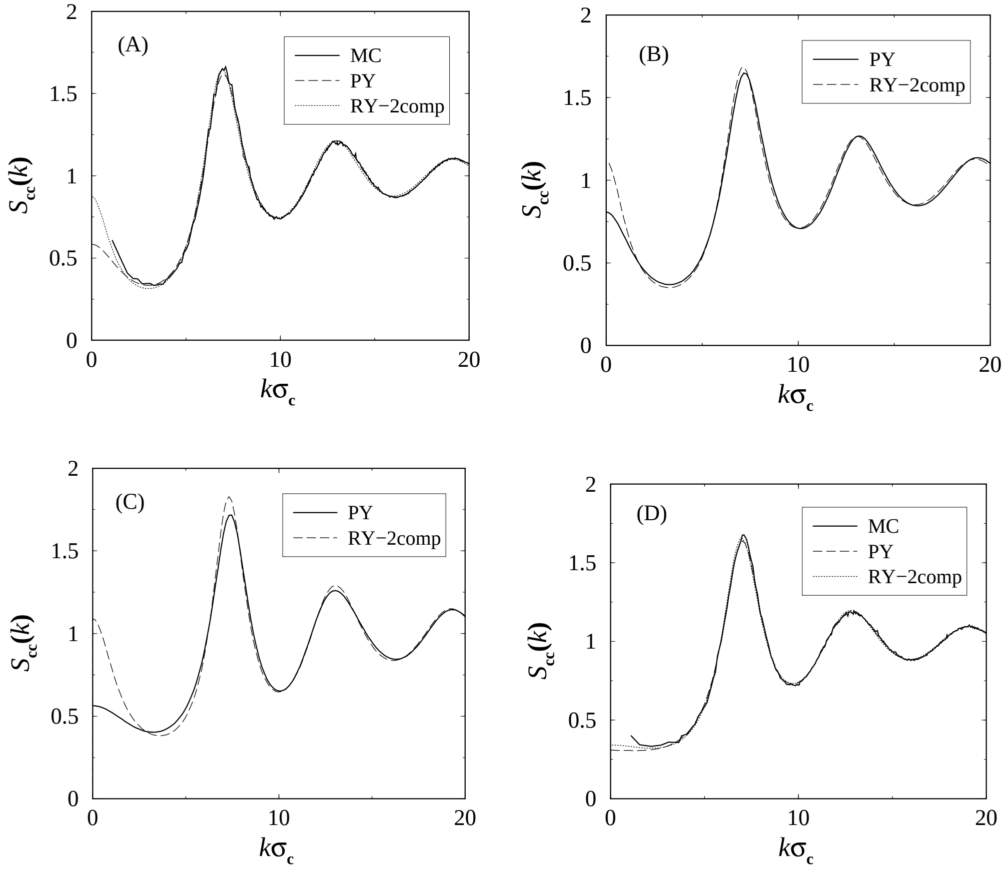

Figure 3.9: Comparison of the static structure factors $S_{\text{cc}}(q)$ for the colloids at different state points (A)-(D), denoted by the asterisks in the phase diagram for $q = 0.5$ in figure 3.7 (d)-(f). Using the depletion potentials from the one-component description MC simulations (solid lines) are compared to PY results (dashed lines). Dotted lines present RY-results employing the full binary OZ-equations.

inaccuracies caused by the interpolation in the neighborhood of the spinodal become more and more relevant.

We now discuss the colloid-colloid correlation functions in the fluid phase. We showed how to translate the star polymer densities on the phase boundaries to the corresponding chemical potentials or reservoir packing fractions. Hence, we are able to compare the structure of the colloids in the one- and two-component description on selected state points of the phase diagrams. In Fig. 3.8 we plot the pair distribution function g_{cc} and in Fig. 3.9 the associated static structure factors $S_{\text{cc}}(k)$ corresponding to four different state points (A)-(D) in the phase diagram Fig. 3.7. The size ratio is $q = 0.5$ and the arm numbers f vary. The state points (A)-(C) are chosen to be close to the fluid-fluid demixing critical point, while point (D) is deep in the stable fluid phase. For the one-component system we use the Percus-Yevick (PY)-closure, which is expected to be accurate for the short-ranged interactions between the colloids. For the two-component case, we use the RY-closure as described in section 3.1. In addition we compute the correlation functions with computer simulations for the state points (A) and (D), where the fluid demixing transition is not preempted by freezing. In the simulations the structure factor was calculated directly, using [36]

$$S_{\mathrm{cc}}(k) = N_{\mathrm{c}}^{-1} \left\langle \rho_{\mathrm{c}}(\boldsymbol{k}) \rho_{\mathrm{c}}(-\boldsymbol{k}) \right\rangle , \tag{3.19}$$

where $\rho_{\mathrm{c}}(\boldsymbol{k})$ is the Fourier transform of the colloid one-particle density operator and is defined as [36]

$$\rho_{\mathrm{c}}(\boldsymbol{k}) = \sum_{i=1}^{N_{\mathrm{c}}} \exp(\mathrm{i}\boldsymbol{k} \cdot \boldsymbol{r}_i), \tag{3.20}$$

with the sum being extended over all positions $\boldsymbol{r}_i$ of the N_c colloidal particles.

The simulations were performed using the same one-component effective interactions as the PY-calculations. First of all, the agreement between PY and simulations data demonstrates that the PY-closure yields very good results for the structure in systems with a hard-sphere interaction dressed with a short-range attraction, as also seen in Refs. [9] and [123]. Further, the $S_{\mathrm{cc}}(k)$'s resulting from the solution of the two-component system (through the RY-closure) are indeed very similar to those arising from the solution of the effective one-component system (through the PY-closure) at the corresponding thermodynamic points. This demonstrates the validity of the mapping procedure and also serves as an indirect proof that higher-order interactions, which have been neglected in the one-component description, are not crucial [124, 125]. The structure factors at the thermodynamic points (A), (B), and (C) show the typical enhancement for low k-values, due to their close distance from the demixing spinodal. The faster divergence of the RY-structure factor is in line with the fact that the demixing binodals of the two-component description are somewhat broader than those arising in the framework of the depletion picture.

3.4 Summary and concluding remarks

Using the effective interactions introduced in the previous chapter we have traced out the phase diagram of star-polymer–colloid mixtures, establishing the limits of stability of the demixing binodals as functions of the star functionality and the size ratio, for the case in which the star-polymers are smaller than the colloids. We have demonstrated the equivalence of a two-component approach with a depletion picture, in which the stars are further traced out. Star polymers have been shown to fulfill their unique role as natural bridging systems between soft polymers (for low f) and colloidal particles (at high f). Hence, they can act as selective depletants between colloidal hard spheres. All our findings can be experimentally checked by carefully preparing mixtures of index-matched hard sphere colloids with monodisperse star-polymers in good solvents [98].

The stability of the demixing with respect to freezing has been recently studied in some generality in the framework of the model of non-additive hard spheres [17, 126, 127]. Whether the present system can also fit within this picture remains to be seen. Our work is limited to star-colloid size ratios smaller than unity, since the star-colloid interactions employed here are derived under the assumption that the star never ‘crawls over’ the colloidal hard sphere, see chapter 2. The investigation of the opposite case, in which the small colloids can fully penetrate into the corona of the star-polymers [128] is problem for the future too.

Chapter 4

Nonequilibrium transitions in driven binary colloidal mixtures

When brought into nonequilibrium, colloidal mixtures may spontaneously exhibit many different kinds of pattern formation (for recent reviews see Refs. [129, 130]) which are much richer than the traditional phase transitions in equilibrium systems. While the latter are by now well-understood by microscopic theories and simulations [33, 34, 35, 36], full microscopic theories operating on a particle-resolved level for nonequilibrium situations still represent a major challenge. In this chapter we present a "microscopic" system designed to model binary colloidal suspensions in an external field which is an off-lattice version [38] of a diffusive system in an external driving field. In our model, we consider an equimolar binary mixture of so-called A and B particles. The particles are identical as far as their mutual interaction is concerned which we model via a Yukawa pair potential having charged colloidal dispersions in mind. The A and B particles, however, respond differently to the external field applied: A particles feel an external force $\vec{F}^{(A)}$ while B-particles are driven by a different force $\vec{F}^{(B)}$. Completely overdamped Brownian dynamics (with hydrodynamic interactions neglected) is assumed [131, 132] for the colloidal motion.

For oppositely oriented external forces we observe that above a critical strength of the external force, the system exhibits a transition towards lane formation. The lanes comprise bundles of particles of the same kind (A or B) and are parallel to the driving field. This nonequilibrium phase separation [133] results from a slip-stream effect caused by the evading colloids acting via repulsive interparticle interactions. The critical force can be theoretically estimated by comparing the external force to a typical interaction force resulting from the pairwise potential $V(r)$ between the particles.

In order to characterize the lane phase we use suitable order parameters. We also find an increase of the particle transport in the field direction induced by lane formation and a drastic reduction of particle transport perpendicular to the field direction, which may serve as dynamical criteria for detecting the lane formation. We further show that lane formation is very general and is thus a generic feature of any two-component driven diffusive system. In fact, using computer simulations we demonstrate that lane formation also occurs in unconfined systems, in three spatial dimensions, and for time-dependent oscillatory fields. In the latter case the system exhibits a transition back to the disordered state upon reaching a critical field frequency. In the next step we present the case where the two external forces $\vec{F}^{(A)}$ and $\vec{F}^{(B)}$ are not parallel, for which lane formation does also occur. The direction of the lanes, however, is tilted with respect to the driving fields. In more detail lanes are directed along the difference vector $\vec{F}^{(B)} - \vec{F}^{(A)}$ of the two external forces. In addition, we describe - for parallel forces - the case where the equilibrium field-free state is crystalline. For a randomly occupied crystal a two-stage transition shows up: first, above a threshold, the external fields melt the solid mechanically. Upon increasing the external field strength further, a reentrant freezing transition is discovered. The resulting crystalline structure involves completely demixed A- and B solids sliding against each other similar to the fluid lane formation.

4.1 The model and simulation technique

In our model, we consider a binary mixture comprising $2N$ Brownian colloidal particles in $d = 2$ or $d = 3$ spatial dimensions. The particles are either in an area S or in a volume Ω with a fixed total number density of $\rho = 2N/S$ and $\rho = 2N/\Omega$, respectively. Half of them are particles of type A, the other half is of type B such that the partial number densities are $\rho_A = \rho_B = \rho/2$. The system is held at fixed temperature T being embedded in a bath of microscopic solvent particles of the same temperature. Two colloidal particles are interacting via an effective pair potential. For simplicity we study the symmetric case $V_{AA}(r) = V_{AB}(r) = V_{BB}(r) \equiv V(r)$ where r is the interparticle distance. We assume an effective screened Coulomb interaction (or Yukawa form)

$$V(r) = V_0\, \sigma \exp\left[-\kappa(r-\sigma)\right]/r, \tag{4.1}$$

where V_0 is an energy scale and σ is the particle diameter as a length scale. This is a valid model for charge-stabilized suspensions both in two [134] and three dimensions [3]. The inverse screening length κ governs the range of the interaction and can be tuned, e.g., by the concentration of added salt in the colloidal solution.

The dynamics of the colloids is assumed to be completely overdamped Brownian motion with hydrodynamic interactions neglected, which is a safe approximation if the colloidal volume fraction is small. The friction constant $\xi = 3\pi\eta\sigma$ (with η denoting the shear viscosity of the solvent) is assumed to be the same for both A and B particles. The external constant or oscillatory force acting on the ith particle is different for the both constituents of the binary mixture. It is

$$\vec{F}_i(t) = \vec{F}^{(A)}\, \mathrm{rect}(\omega t) \quad \text{for } A \text{ particles} \tag{4.2}$$

and

$$\vec{F}_i(t) = \vec{F}^{(B)}\, \mathrm{rect}(\omega t) \quad \text{for } B \text{ particles.} \tag{4.3}$$

ω is the external frequency (with $\omega \equiv 0$ leading to the constant-field case). $\vec{F}^{(A)}$ and $\vec{F}^{(B)}$ are arbitrary constant vectors of the external field. With rect(ωt) we apply a rectangular oscillation switching from 1 to -1 defined via:

$$\mathrm{rect}(x) = \begin{cases} 1, & n \leq x \leq (2n+1)/2 \\ -1 & (2n+1)/2 < x < n+1 \end{cases} \tag{4.4}$$

with $n = 0..\infty$.

The stochastic Langevin equations for the colloidal trajectories $\vec{r}_i(t)$ $(i = 1, ..., 2N)$ read as

$$\xi \frac{d\vec{r}_i}{dt} = -\vec{\nabla}_{\vec{r}_i} \sum_{j \neq i} V(\mid \vec{r}_i - \vec{r}_j \mid) + \vec{F}_i(t) + \vec{F}_i^{(\mathrm{R})}(t). \tag{4.5}$$

There are different forces acting onto the colloidal particles: first there is the force attributed to interparticle interactions, then there is the external shaking or constant ($\omega = 0$) field and finally the random forces $\vec{F}_i^{(\mathrm{R})}$ describe the kicks of the solvent molecules acting onto the ith colloidal particle. These kicks are Gaussian random numbers with zero mean, $\overline{\vec{F}_i^{(\mathrm{R})}} = 0$, and variance

$$\overline{(\vec{F}_i^{(\mathrm{R})})_\alpha(t)(\vec{F}_j^{(\mathrm{R})})_\beta(t')} = 2k_BT\xi\delta_{\alpha\beta}\delta_{ij}\delta(t-t'). \tag{4.6}$$

The subscripts α and β stand for the $d = 2$ or $d = 3$ Cartesian components and k_BT is the thermal energy.

In equilibrium (i.e., in the absence of any external field, such that $\vec{F}^{(A)} = F^{(B)} = 0$) the model reduces to a Brownian Yukawa fluid , which has been extensively investigated as far as structural and dynamical equilibrium correlations and freezing transitions are concerned, both in three [135, 136, 137] and two [134, 138, 139] spatial dimensions. Our model is specified by various input parameters, namely the total particle density ρ, the thermal energy k_BT, the inverse screening length κ, the dimensionless quantities $U_0 = V_0/k_BT$, and $\omega\tau_{\mathrm{B}}$, where $\tau_{\mathrm{B}} = \xi\sigma^2/V_0$ is a suitable Brownian time scale.

Our Brownian dynamics (BD) code is similar to the one used in nonequilibrium simulations of charge-polydisperse colloids [131, 140, 141]. For $d = 2$, we put $N = 250$ A and $N = 250$ B particles into a square cell of length ℓ with periodic boundary conditions. The total colloidal number density is $\rho = 2N/\ell^2$. Likewise, in three dimensions, $N = 500$ A and B particles are in a cubic box of length ℓ such that $\rho = 2N/\ell^3$. For the snapshots of the $d = 3$ system (Figs. 4.3 and 4.13) we increased the number to $2N = 8000$ particles for a better resolution of the structure. We checked that the results are not dependent of the number of simulated particles, except for small numbers, for which we found the usual finite-size effects. We tried different starting configurations. The system was observed to run into a nonequilibrium steady-state independent of the initial configuration. The Langevin equations of motion including the shaking external field were numerically solved using a finite time step Δt and the technique of Ermak [33, 142]. The typical size of the time step was $\Delta t = 0.003\tau_{\mathrm{B}}$. We simulated typically 2×10^4 time steps which corresponds to a simulation time of $60\tau_{\mathrm{B}}$. After an initial relaxation period of $20\tau_{\mathrm{B}}$, statistics was gathered.

4.2 Parallel external forces

Let us first consider the case of parallel external forces. For simplicity we assume the symmetric case $\vec{F}^{(A)} = -\vec{F}^{(B)} = f\vec{e}_y$, where $\vec{e}_y$ is the unit vector along the y direction. This is not any restriction. In fact, the asymmetric case of parallel forces $\vec{F}^{(A)} + \vec{F}^{(B)} \neq 0$ can directly be mapped onto the symmetric case by subtracting the overall dynamical mode

$$\vec{r}_0(t) = \frac{\vec{F}^{(A)} + \vec{F}^{(B)}}{2\xi} \int_0^t \mathrm{rect}(\omega t')\mathrm{d}t'. \tag{4.7}$$

The Langevin equations (4.5) can be rewritten in terms of new reduced trajectories $\tilde{\vec{r}}_i(t) \equiv \vec{r}_i(t) - \vec{r}_0(t)$ such that the transformed equations have the same form as in the symmetric case with $f\vec{e}_y = (\vec{F}^{(A)} - \vec{F}^{(B)})/2$. This implies that a binary charged suspension with charges of equal sign is also a good realization of our model: it only matters that the external field acts differently for both species. After a Galilei transformation the symmetric case is realized. For further considerations we define the dimensionless field strength $f^* = f\sigma/k_BT$.

4.2.1 Order parameter

Static order parameter

In order to detect the transition towards lane formation a sensitive order parameter is needed. A suitable order parameter could probe particle density inhomogeneities along the field in y direction which vanish in an ideal lane configuration. Therefore, we assign to every particle i an order parameter ϕ_i, which is chosen to be 1 when the lateral distance $r_\mathrm{l} = |x_i - x_j|$ ($r_\mathrm{l} = \sqrt{(x_i - x_j)^2 + (z_i - z_j)^2}$ in three dimensions) to all particles j of the other type is larger than a suitable length scale, say $r_\mathrm{l} > \rho^{-1/d}/2$. Otherwise, ϕ_i is set to zero. A global dimensionless order parameter ϕ can now be defined as

$$\phi = \frac{1}{N} < \sum_{i=1}^{N} \phi_i >, \tag{4.8}$$

where the brackets denote a time average. In a completely mixed state, ϕ vanishes while for ideal AB separation, $\phi = 1$. A typical result for ϕ as a function of field strength f is shown for $d = 2$ and a constant field ($\omega = 0$) in Fig. 4.1. While ϕ is small for a small constant field, it grows when a critical field strength f_c is approached. Further increasing of the external field yields values close to unity. The transition towards lane formation is reversible but exhibits a significant hysteresis. This can be deduced from Fig. 4.1(b) where the external field strength was slowly decreased. Hence we conclude that lane formation is a nonequilibrium first-order transition. As can be deduced from Fig. 4.1, the critical field strength f_c increases with increasing κ. More results for the location of the nonequilibrium phase transition will be presented in Sec. 4.2.3.

Simulation snapshots associated with a situation without a field as well as with a field below and above the critical field strength are shown in Fig. 4.2(a)-4.2(c). One clearly sees

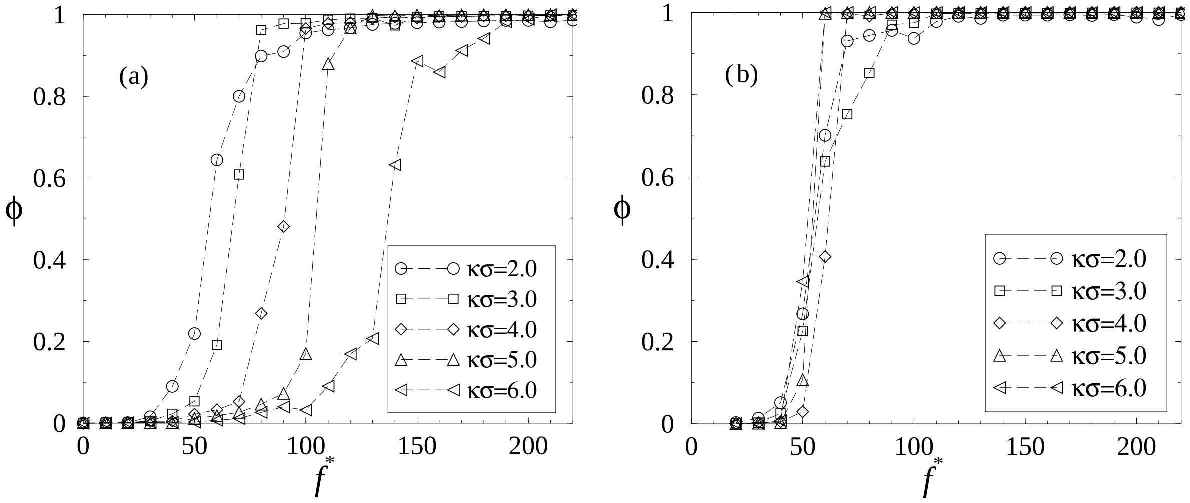

Figure 4.1: Dimensionless order parameter ϕ as a function of field strength f^* for $d = 2$ and different inverse screening lengths $\kappa\sigma$. In (a) the field is increased starting from a randomly mixed configuration, while in (b) the initial configuration is completely demixed (two lanes) and the field is decreased. The density is $\rho\sigma^2 = 1.0$ and $U_0 = 2.5$, $\omega = 0$.

lane formation parallel to the external field. A characteristic length scale corresponding to lane formation is the average thickness of the lanes. In the snapshots, this thickness of the lanes is about several interparticle spacings. It may be conjectured, however, in analogy with lattice models [38], that the finite width of the lanes is due to a lack of relaxation into the final steady state, which is a fully phase-separated situation.

We have, furthermore, considered situations with nonvanishing field frequencies ω. If an oscillatory field with amplitude $f > f_c$ is present and the frequency ω is increased, the order parameter ϕ decreases with increasing ω. For low frequencies the system remains in the lane state, $\phi \approx 1$, while above a critical frequency, the system gets back to disorder and ϕ fades to zero.

All these considerations are the same for a three-dimensional system. Corresponding snapshots with lane configurations are shown in Fig. 4.3(a), 4.3(b). Of course, due to the presence of an additional dimension, the lane structure is more complicated in three dimensions (3D) than in 2D. A cut through a plane perpendicular to the field is shown in Fig. 4.3(b) demonstrating that the in-plane-structure is reminiscent of a two-dimensional phase separation or a percolating network.

Dynamical diagnostics

For a constant field ($\omega = 0$), we have also computed dynamical correlations in the nonequilibrium steady state focusing on particle transport properties parallel and perpendicular to

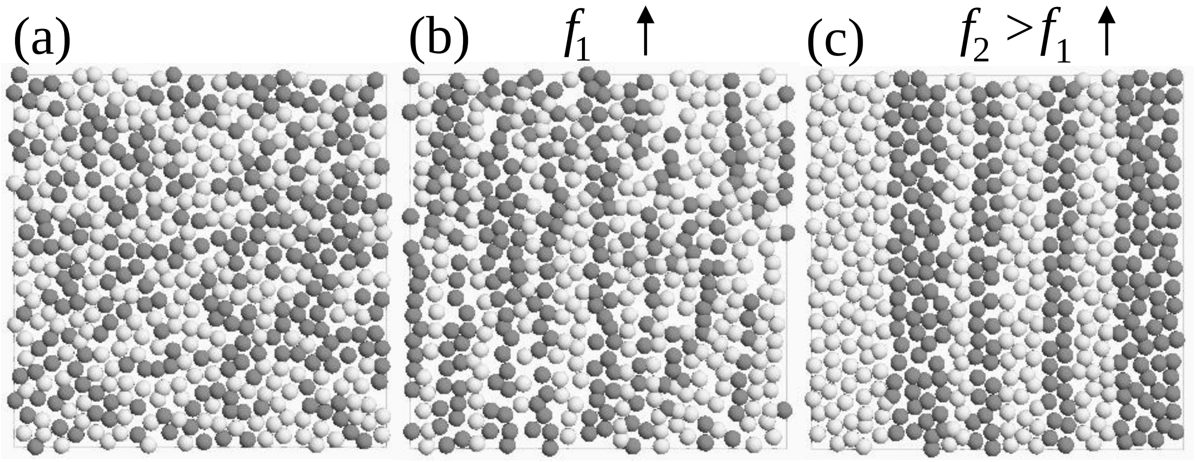

Figure 4.2: Typical simulation snapshots of the two-dimensional system: (a) disordered state without field ($\phi = 0$), (b) disordered state with field $f = f_1 \approx f_c$ ($\phi \approx 0.45$), (c) lane formation with field $f = f_2 > f_1$ ($\phi \approx 0.99$). The particles are depicted as spheres with diameter σ. A light sphere is an A-particle while a gray sphere is a B-particle. The parameters are $\kappa\sigma = 4.0$, $\rho\sigma^2 = 1.0$, $U_0 = 2.5$, and $\omega = 0$.

the external field. In fact, as expected, the particle transport in field direction is enhanced once lanes have been formed. In detail, for a constant field, we define the averaged drift velocity v_D along the field for each particle species by measuring the mean-square displacement in y direction in the nonequilibrium steady state by

$$v_D^2 := \lim_{t\to\infty} \frac{< [(\vec{r}_i(t) - \vec{r}_i(0)) \cdot \vec{e}_y]^2 >}{t^2}. \tag{4.9}$$

Clearly, as the long-time dynamics is diffusive in equilibrium, $v_D = 0$ for $f = 0$. In the mixed state v_D is small as the external field enforces a transport, which is, however, still hindered by the presence of different particle species. Once lanes are formed, v_D increases as the obstacles made up by different particle species are not any longer present signaling an efficient particle transport along the lanes in directions parallel to the field. An example of v_D versus increasing field strength f for $d = 2$ is shown in Fig. 4.4(a) These results are compared to the drift velocity of a one-component Brownian system in an external field, where

$$v_D \equiv v_0 = f/\xi, \tag{4.10}$$

corresponding to a trivial overall dynamical mode of all the particles. Indeed during lane formation, as probed by the order parameter ϕ, the drift velocity practically equals v_0. For small fields, on the other hand, v_D is significantly smaller than v_0. Hence lane formation manifests itself in a dynamical anomaly in the drift velocity, which can be used as a dynamical diagnostics to detect such a dynamical phase change.

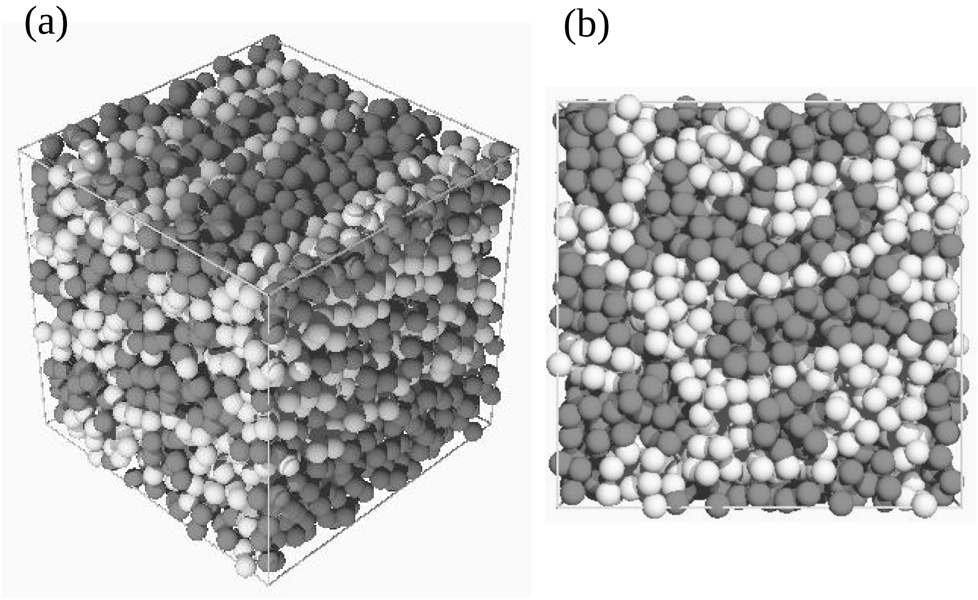

Figure 4.3: Typical snapshots of the three-dimensional system with external field $f > f_\mathrm{c}$ and lanes parallel to the field: (a) three-dimensional view, (b) look on the (x, z) plane perpendicular to the field direction y. The particles are rendered as spheres with diameter σ. For these snapshots we simulated $2N = 8000$ particles. The parameters are $\kappa\sigma = 2.0$, $U_0 = 2.5$, $\rho\sigma^3 = 1.0$, and $\omega = 0$.

A more dramatic effect is observed for the long time diffusion coefficient perpendicular to the field direction as defined via

$$D_\mathrm{L} := \lim_{t\to\infty} \frac{< [(\vec{r}_i(t) - \vec{r}_i(0)) \cdot \vec{e}_x]^2 >}{2t}. \tag{4.11}$$

For a vanishing external field in equilibrium, the long-time self-diffusion coefficient D_L has been the subject of intense recent research, in particular, for Brownian Yukawa systems as studied here [143, 144, 145, 146, 147, 148, 149, 150]. Turning on the external field strength f, particles of different types can only follow the external field by eluding each other, so that the diffusion perpendicular to the external field has to increase with f. This effect grows until the critical field strength is reached and the system begins to form lanes. Now the particles are confined to lanes with thickness of some interparticle spacings which reduces the perpendicular diffusion again. Results for D_L versus f are shown in Fig. 4.4(b) for $d = 2$, together with the corresponding order parameter ϕ, and confirm these qualitative considerations. The spectacular decrease of D_L versus f strongly correlates with the location of the lane formation as indicated by a strongly increasing parameter ϕ. This drastic decrease can be exploited as a sensitive dynamical diagnostics to locate lane formation. We remark that after a very long time, lanes may fuse towards big nonstructured regions. In this case, the final fall-off of D_L for $f > f_c$ can be slightly shifted upwards to the equilibrium diffusion coefficient at $f = 0$.

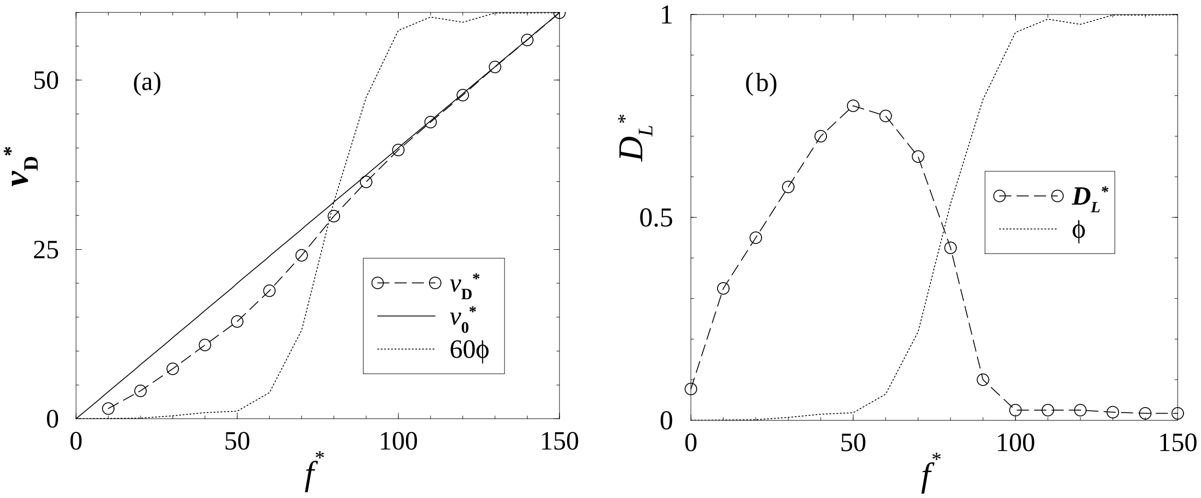

Figure 4.4: (a) Averaged dimensionless drift velocity $v_{\mathrm{D}}^* = v_{\mathrm{D}}\tau_{\mathrm{B}}/\sigma$ in y direction versus the external field f^* compared to the dimensionless drift velocity $v_0^* = v_0\tau_{\mathrm{B}}/\sigma$ of a one-component Brownian system and to the order parameter ϕ. (b) Dimensionless long-time diffusion coefficient $D_{\mathrm{L}}^* = D_{\mathrm{L}}\tau_{\mathrm{B}}/\sigma^2$ in $x-$direction versus f^* also compared to ϕ. In (a) the ϕ-curve is inflated to the maximal shown ordinate-value for better comparison. The parameters are $d = 2$, $\kappa\sigma = 4.0$, $U_0 = 2.5$, $\rho\sigma^2 = 1.0$, and $\omega = 0$.

4.2.2 Simple Theory

Constant field

We are aiming at a rough theoretical estimation of the boundaries of the laning transition with constant external field f in two or three dimensions. We assume that the system goes into the stratified state when the external field is larger than the typical average force between two particles of opposite type. The latter depends both on density and on the external field itself. We estimate a typical average force between two opposite particles by considering different “effective” interparticle spacings. The first typical interparticle spacing is set by the density alone, $a = \rho^{-1/d}$. Including fluctuations in the interparticle distance induced by a finite temperature results in a further smaller effective average distance $\tilde{a}$ as obtained by setting a typical interparticle energy equal to $V(a) + k_BT$. Hence $\tilde{a} = V^{-1}\left[V(a) + k_BT\right]$ where V^{-1} is the inverse function of the interaction potential $V(r)$. Finally the presence of an external field enforces an even smaller averaged distance a' between colliding opposite particles, which can be estimated via

$$a' = F^{-1}\left[f + F(\tilde{a})\right], \tag{4.12}$$

where F^{-1} is the inverse function of $F(r) = -\nabla V(r)$. In general, a pair of opposite particles will not collide centrally such that the actual average distance is between a' and $\tilde{a}$. Hence the averaged force $\overline{f}$ between an A and a B particle is roughly

$$\overline{f} = \frac{1}{\tilde{a} - a'}[V(a') - V(\tilde{a})]. \tag{4.13}$$

The critical force f_c is reached when the external force becomes of the order of the mean force $\overline{f}$,

$$f_c = \alpha \overline{f}. \tag{4.14}$$

α is a yet not known dimensionless prefactor of the order of unity, which should depend, in general, on the dimensionality d. It will be determined later by an optimal fit with our simulation results, see Sec. 4.2.3.

Oscillatory field

We now focus on time-dependent external fields (4.2)-(4.3) with nonvanishing frequency. We propose a simple theory that predicts the critical frequency $\omega \equiv \omega_c$ upon which a transition back to the disordered state occurs. Let the field amplitude f be such that $f > f_c$ holds. In the segregated mixture the particles are moving collectively with the external field. Their velocity in field direction changes sign but roughly has the modulus of the drift velocity v_0, (4.10). At the interfaces between two lanes, there is an additional friction due to the oppositely moving particles of the other type. This additional friction should scale with the range $1/\kappa$ of the interparticle interaction in terms of a typical microscopic spacing σ. Hence the drift velocity $\tilde{v}_0$ near an interface is

$$\tilde{v}_0 \approx \frac{f}{\xi(1 + 1/(\kappa\sigma))}, \tag{4.15}$$

which changes, however, its sign periodically according to the shaking external field. Now we consider the stability of two lanes at their interface. The field frequency has to be small enough in order to provide a sufficiently long time period in which the two lanes can slide against each other avoiding a mixing of different particle species. If this time is getting very small, diffusion perpendicular to the field direction will dominate and destroy the sharp interface. Lane stability is lost when a particle has roughly reached a typical interparticle spacing $a = \rho^{-1/d}$ during half a period $1/2\omega$ of the external field. Thermal fluctuations can be neglected compared to the high critical force. This yields for the critical frequency

$$\tilde{v}_0 / 2\omega_c \approx \rho^{-1/d} \tag{4.16}$$

or

$$\omega_c \approx \frac{f \rho^{1/d}}{2\xi(1 + 1/(\kappa\sigma))}. \tag{4.17}$$

This result can be understood both in a more qualitative and more quantitative way. Qualitatively, it can be interpreted as a scaling law predicting different exponents for the

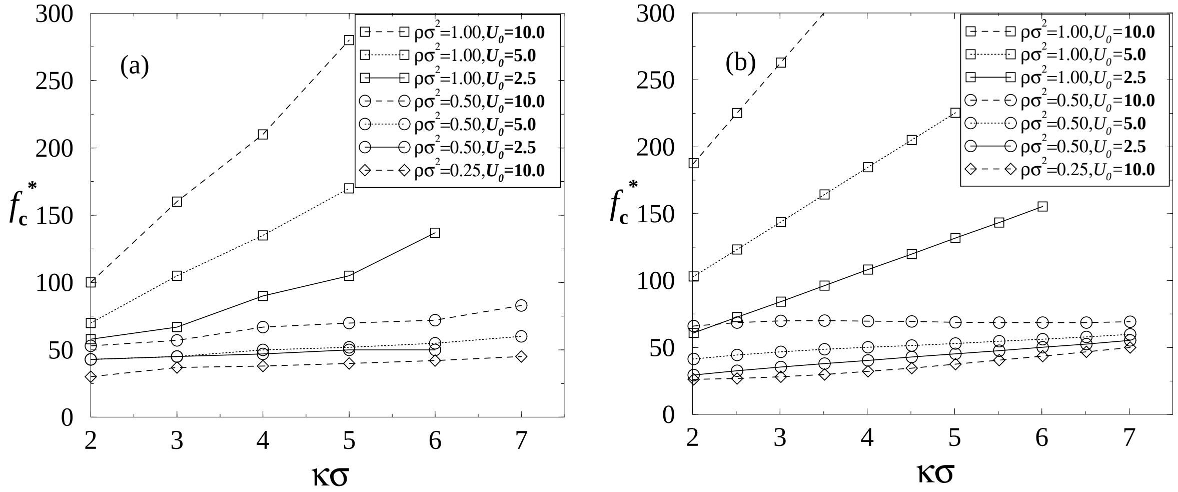

Figure 4.5: Critical field strength f_c^* for the 2d-system versus $\kappa\sigma$ for different U_0 and $\rho\sigma^2$ as obtained from Brownian dynamics simulation (a) and theory (b). By increasing the field strength f^* the system shows a phase transition from a disordered state to a state characterized by lane formation. The transition is indicated by the symbols, the lines are a guide to the eye.

transition frequency for varying field strength, friction coefficient, screening length, and particle density. Note that in our theory the transition frequencies are independent of temperature. Furthermore, Eq. (4.17) is a full quantitative prediction, which we shall test against our computer simulation data in Sec. 4.2.3.

4.2.3 Results for the nonequilibrium phase diagram

Constant field

The dynamical phase diagram for a constant ($\omega = 0$) external force obtained from computer simulations is shown in Fig. 4.5(a). The location of the phase transition is estimated via the behavior of the order parameter ϕ: the critical field strength f_c^* is obtained by setting $\phi = 0.5$ for a set of runs with increasing field strengths f^*. The plots clearly show that for increasing density ρ or increasing interaction energy U_0, an enhanced critical force f_c is necessary to drive a transition towards lane formation. By increasing one of these two parameters the correlation between the particles is getting stronger, so as a conclusive result we can state that whenever the correlation is increased the critical force is getting higher. A bit more subtle is the dependence on κ, which is the inverse range of the interaction potential and controls the "softness"of the interaction. By watching, e.g., pair correlation function in equilibrium, one observes an increase in correlation for increasing κ. This explains why the

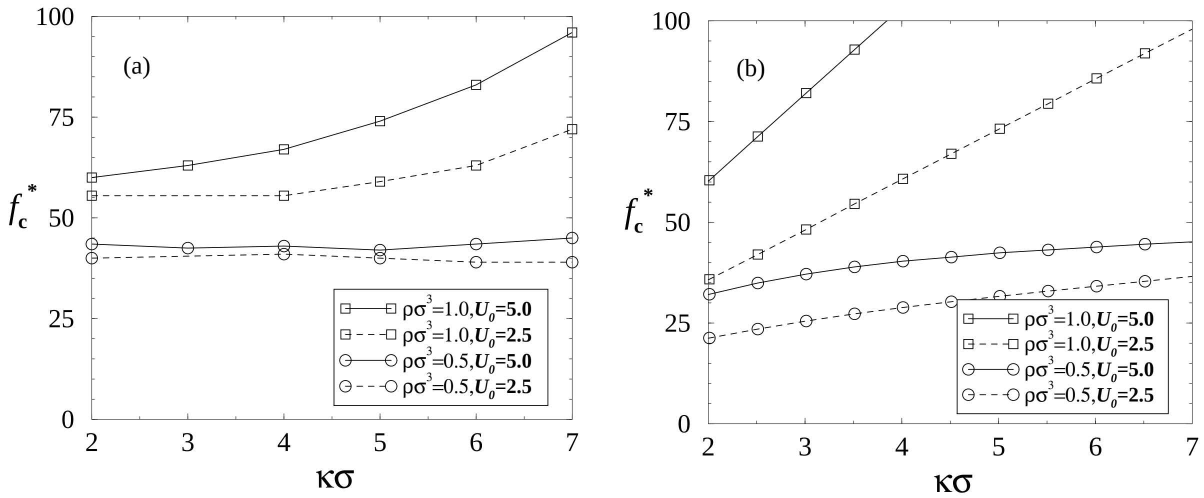

Figure 4.6: Same as Fig. 4.5 for the three dimensional system: (a) simulation results, (b) theory.

critical field strength f_c^* is increasing with κ, although this increase is practically marginal for small densities. We also remark that, for densities $\rho\sigma^2 = 1.0$ or $\rho\sigma^3 = 1.0$ in three dimensions and high $\kappa\sigma \approx 5, 6$, the system is slightly below the equilibrium bulk freezing transition [135, 139]. The particles are highly correlated and the external force has to be strongly enhanced to enforce stratification.

In Fig. 4.5(b) we plot the results of our simple theory as described in Sec. 4.2.2 for the same parameter combinations as chosen for the simulations in Fig. 4.5(a). Comparing theory and simulation we see that the theory reproduces all trends correctly. In particular, f_c^* grows with increasing ρ, U_0, and κ as obtained in the simulations. By assigning to α in Eq. (4.29) a value $\alpha = 2.0$ the theory even brings about quantitative agreement, in particular for the low density cases ($\rho = 0.25, 0.5$) and can thus be used for a simple estimate for the location of the transition towards lane formation. Furthermore the assumption implicit in our theory that the transition is modified by particle correlations is justified.

Similar results for the nonequilibrium phase transition in *three* spatial dimensions are presented in Fig. 4.6. We have observed the same trends as in two dimensions. Again the theory is in semi-quantitative agreement with our simulation data though the curvature of the f_c versus $\kappa\sigma$ data are slightly different. Here the optimal fit is $\alpha = 1.5$.

Oscillating field

For an oscillating external field, data for the critical frequencies ω_c upon which the system goes back into a disordered state are given in Fig. 4.7. They are shown versus the field amplitude for different particle densities ρ (Fig. 4.7(a)) and for different particle interaction

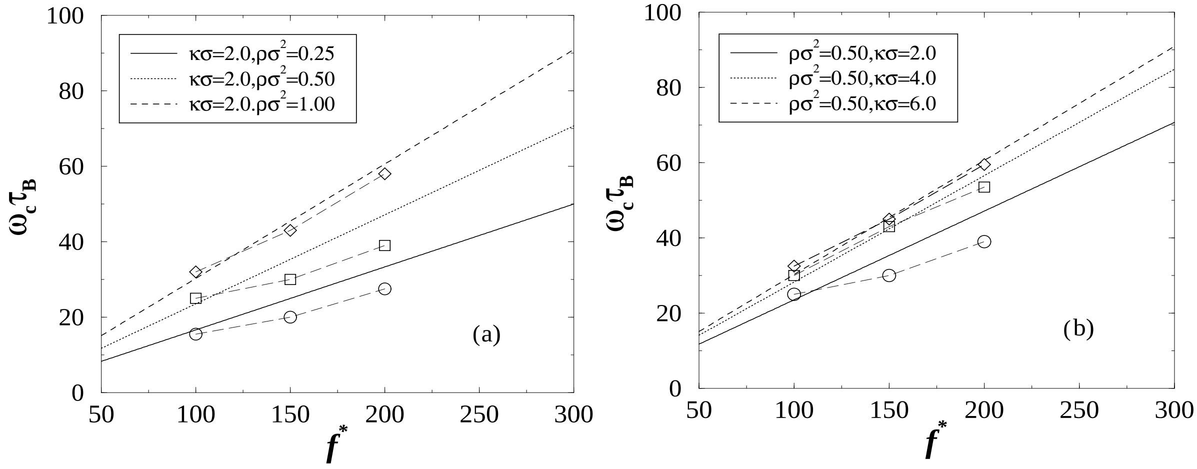

Figure 4.7: Nonequilibrium phase diagram for the two dimensional system with oscillatory external field for $U_0 = 5.0$. The critical field frequency ω_c in units of $1/\tau_\mathrm{B}$ is plotted versus the field amplitude f^* for different densities (a), and for different screening lengths (b). For low frequencies the system stays in the stratified state, while for increasing frequency there is a transition back to disorder. Lines are theoretical estimations, symbols are the corresponding simulation results. The long dashed lines connecting equal symbols are a guide to the eye. In (a) the boundary moves up with increasing density, in (b) the boundary moves up with increasing decay length.

ranges $1/\kappa$ (Fig. 4.7(b)). The trends are as follows: ω_c increases for increasing amplitude, increasing density and increasing κ. In our considered parameter range no obvious U_0 dependence was found in the simulation. All these trends are in accordance with our simple theory which is also plotted in Fig. 4.7. The theory is even confirmed quantitatively by our simulation data. The discrepancy between theory and simulation is always smaller than 20% at least in the parameter range where simulations were performed.

4.3 Nonparallel external forces

We now proceed with the generalization of our considerations to the case of nonparallel external forces $\vec{F}^{(A)}$ and $\vec{F}^{(B)}$ [151]. We will see that the results for oscillatory forces remain the same as for the case of parallel forces so that we only consider constant external forces $\omega = 0$.

4.3.1 Tilted lane formation

Let us first recapitulate what is known for *parallel* external forces $\vec{F}^{(A)}$ and $\vec{F}^{(B)}$: in the previous section it was shown that lane formation occurs involving either A or B particles which are sliding against each other in the field direction. In the lane involving A particles only, all these particle are drifting with an global velocity $\vec{F}^{(A)}/\xi$ while opposite regions which involve B particles are streaming with the overall velocity $\vec{F}^{(B)}/\xi$. By subtracting the overall velocity using a Galilei transformation one readily sees that within the completely separated lanes, equilibrium Boltzmann statistics is realized. The system just separates into two different equilibrium states which are drifting relative to each other. Physically, the formation of lanes is generated by collisions of A against B particles pushed by the external force which dynamically separates A and B particles until completely demixed lanes are formed. A similar lane formation for sheared granular matter was found via molecular dynamics simulation in [152]. The formation of lanes is a sharp first-order nonequilibrium phase transition occurring if the external field difference $|\vec{F}^{(A)} - \vec{F}^{(B)}|$ exceeds a critical value. A Galilei transformation also proves that only the relative velocity of A and B regions is relevant. Hence, without loss of generality, it is sufficient to study the special case $\vec{F}^{(A)} = -\vec{F}^{(B)}$.

For *nonparallel* external forces, the collisions between A and B particles are not any longer central and the phase separated structure will be different, in general. In order to get insight into the location of an interface between two completely demixed regions involving A and B particles only, we first do a simple continuum argument: consider a (one-dimensional) interface between an A and B region with a direction described by a two-dimensional vector $\vec{d}$, see Fig. 4.8. The full interface position can be parameterized by a set of vectors

$$\vec{r}(s) = \vec{R}_0 + s\vec{d}, \tag{4.18}$$

where s is a real parameter and $\vec{R}_0$ is a vector describing a point on the interface. After a time Δt, the A particles have moved on average a distance $\vec{F}^{(A)}\Delta t/\xi$, while the B particles have been displaced by a distance $\vec{F}^{(B)}\Delta t/\xi$. Neglecting any collisions, the A particles near the interface will move towards a new interface which is described by the set of vectors

$$\vec{r}^{(A)}(s) = \vec{R}_0 + s\vec{d} + \vec{F}^{(A)}\Delta t/\xi, \tag{4.19}$$

while the B particles near the interface will drift to

$$\vec{r}^{(B)}(s') = \vec{R}_0 + s'\vec{d} + \vec{F}^{(B)}\Delta t/\xi \tag{4.20}$$

with another real parameter s'. The interface can only be stable if these two interfaces coincide. In case they do not, there is either empty space which will be filled by neighboring particles or A and B particles will collide which will destroy the interface as well. Hence, the stability criterion is that for any s there is an s' such that $\vec{r}^{(A)}(s) = \vec{r}^{(B)}(s')$ which simply yields the condition

$$\vec{d} = \frac{\Delta t}{\xi(s - s')}[\vec{F}^{(B)} - \vec{F}^{(A)}]. \tag{4.21}$$

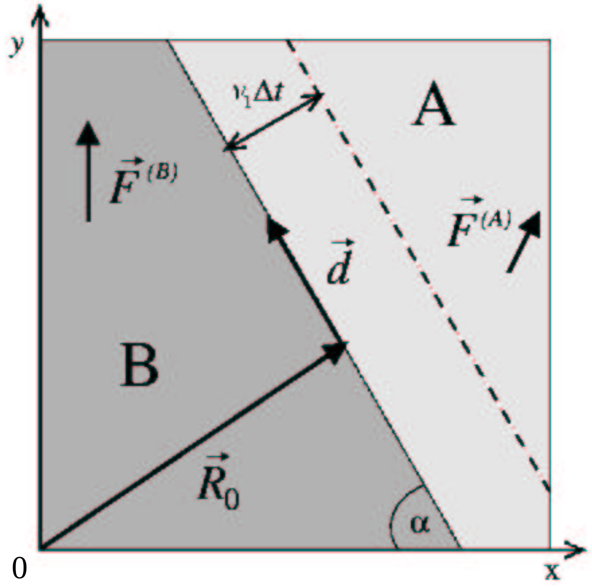

Figure 4.8: One-dimensional interface separating a region containing A particles (light gray) and B particles only (dark gray). The direction of the interface is $\vec d$. The vector $\vec R_0$ points to the interface. The new interface after a time Δt at distance $v_{\mathrm{I}}\Delta t$ from the original one is shown as a dashed line.

This implies that for an interface to be stable, its direction has to be collinear with the force difference

$$\Delta\vec F = \vec F^{(B)} - \vec F^{(A)}. \tag{4.22}$$

Hence, the angle α describing the interface orientation (see Fig. 4.8) is

$$\alpha = \arcsin\frac{\Delta\vec F\cdot\vec F^{(B)}}{|\Delta\vec F||\vec F^{(B)}|}. \tag{4.23}$$

Clearly, contrarily to the case of parallel forces, the interface position will move in space. The interface velocity v_{I} normal to its position can be calculated as

$$v_{\mathrm{I}} = \frac{|\vec F^{(A)}\times\vec F^{(B)}|}{\xi|\Delta\vec F|}. \tag{4.24}$$

Obviously, the same argument can be repeated with exchanged roles of A and B showing that stable parallel lanes with the direction $\Delta\vec F$ are expected which move with the interface velocity v_I given by Eq. (4.24). Furthermore, the same argument applied for a small Δt shows that *a curved interface* is unstable such that a stable interface has to be straight.

Let us finally discuss two special cases: first returning to parallel forces, indeed the interface direction is parallel to the field direction, the angle α is $\pi/2$, and the interface velocity vanishes as follows directly from Eq. (4.24). Second the case of perpendicular forces deserves some particular attention. Here the angle α is

$$\alpha = \arctan \frac{|\vec{F}^{(B)}|}{|\vec{F}^{(A)}|} \tag{4.25}$$

and the interface velocity can be expressed as

$$v_I = \frac{|\vec{F}^{(A)}||\vec{F}^{(B)}|}{\xi|\Delta\vec{F}|}. \tag{4.26}$$

Obviously, this general argument is only a necessary condition for a stable AB interface. An alternative is a mixed situation with no interface at all driven by entropy. In analogy to the parallel case we anticipate that a critical strength of $\Delta\vec{F}$ is needed to build stable lanes. This will now be investigated by computer simulation and simple theory in more detail.

4.3.2 Simulation results compared to simple theory

In our simulation we assume - without loss of generality - the direction of $\vec{F}^{(B)}$ along the y axis of the simulation box. The model parameters are fixed to $\rho\sigma^2 = 1.0$, $\kappa\sigma = 4.0$, and $V_0 = 2.5k_BT$. Simulation snapshots for different external field strengths are shown in Fig. 4.9(a)-4.9(d). In Fig. 4.9(a), no field is applied and a homogeneous completely mixed state is visible. In Fig. 4.9(b), on the other hand, the external forces are parallel: $\vec{F}^{(A)} = -\vec{F}^{(B)}$. The magnitude $|\vec{F}^{(A)} - \vec{F}^{(B)}|$ is beyond the critical strength [153] such that lane formation parallel to the field shows up. Nonparallel forces with perpendicular directions are investigated in Figs. 4.9(c) and 4.9(d). One observes formation of tilted lanes which are indeed in the direction of the force difference vector as expected from our general argument. In following the configurations as a function of time we verified the simple formula of the interface velocity v_I as given in Eq. (4.24).

In a next step, we study perpendicular forces keeping their ratio $q = |\vec{F}^{(A)}|/|\vec{F}^{(B)}|$ fixed but increasing their magnitude. For small forces the system stays demixed. In increasing the strength of both fields, we have calculated suitable order parameters which are sensitive to tilted lane formation. These are immediate generalizations of those used in Ref. [153]. The order parameter exhibits a sharp jump indicating the critical field strength of the force difference vector upon which tilted lane formation is achieved. There is a clear hysteresis loop if the force is reduced again such that the nonequilibrium phase transition towards tilted lane formation is of first order. The critical value ΔF_c of the force difference $|\Delta\vec{F}|$ is shown versus the ratio $q = |\vec{F}^{(A)}|/|\vec{F}^{(B)}|$ in Fig. 4.10. We shall compare these data to a simple theoretical prediction in the next subsection.

A careful remark is in order for small positive q. The periodic boundary conditions used in the simulation correspond to a toroidal topology shown in Fig. 4.11. If q is getting small the boundary conditions enforce a multiple winding around the torus such that finite size effects are expected to be significant. Therefore we have not shown simulation data for small q in Fig. 4.10.

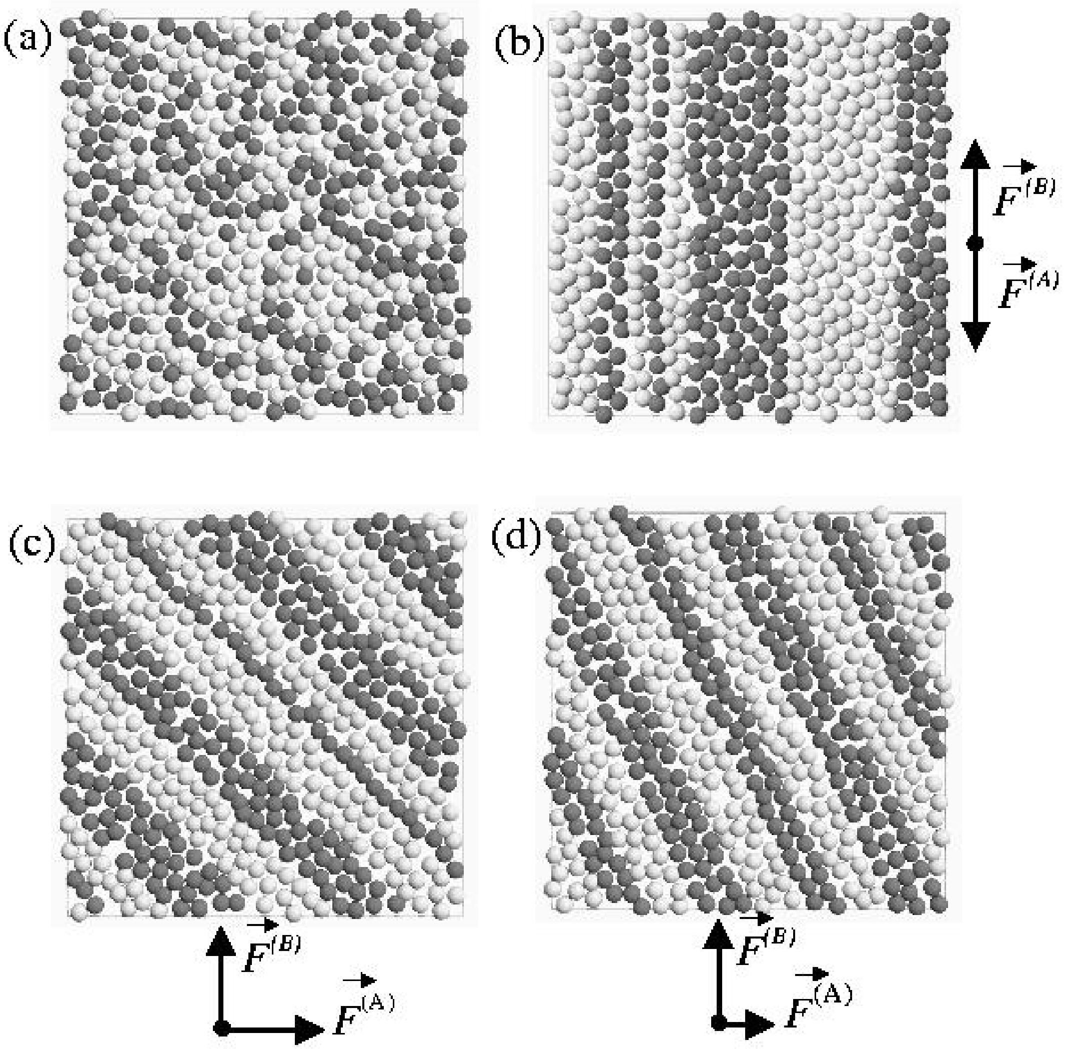

Figure 4.9: Typical simulation snapshots of the two dimensional system: (a) disordered state without field, (b) lane formation with parallel fields $\vec{F}^{(A)} = -\vec{F}^{(B)} = 180k_BT/\sigma$ in y-direction above the critical force. (c) lane formation with perpendicular fields of same magnitude $|\vec{F}^{(A)}| = |\vec{F}^{(B)}| = 180k_BT/\sigma$ above the critical force difference. (d) lane formation with perpendicular fields and $|\vec{F}^{(A)}|/|\vec{F}^{(B)}| = 1/2$ with $|\vec{F}^{(B)}| = 180k_BT/\sigma$ above the critical force difference. In (c) and (d) the A particles are drifting in x-direction, while B particles are drifting in y-direction. The lanes are moving perpendicular to $\Delta\vec{F}$. The particles are depicted as spheres with diameter σ. A light sphere is an A-particle while a gray sphere is a B-particle.

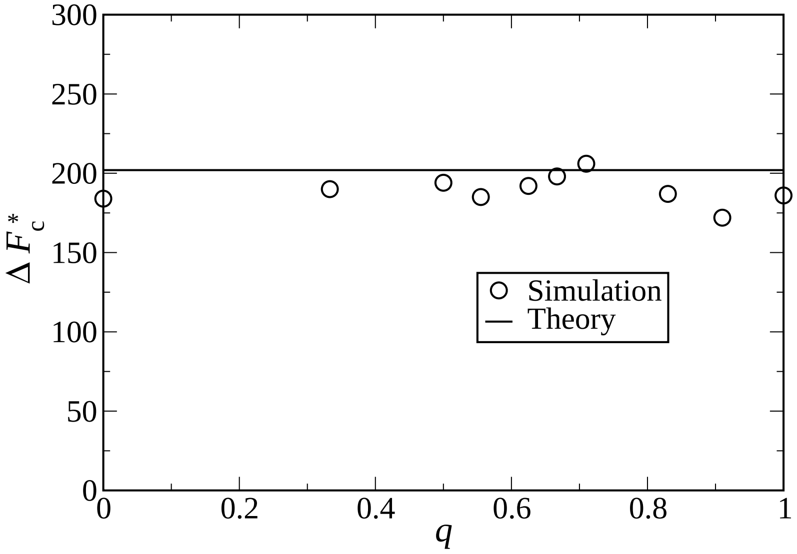

Figure 4.10: Dimensionless critical force difference $\Delta F_c^* = \Delta F_c \sigma / k_B T$ versus the ratio q between the perpendicular forces $|\vec{F}^{(A)}|$ and $|\vec{F}^{(B)}|$ for the two-dimensional system. Above the critical force the system is in the patterned state characterized by stripe formation. The circles are simulation results, while the solid line is theory. The parameters are $\kappa\sigma = 4.0$, $V_0 = 2.5 k_B T$, and $\rho\sigma^2 = 1.0$.

Theory

We are aiming at a rough theoretical estimation of the boundaries of the demixing transition with constant external fields $\vec{F}^{(A)}$ and $\vec{F}^{(B)}$. This was already put forward in the previous section for parallel forces and is generalized here to the general case of nonparallel forces. Consider first a central collision between an A and B particle pair, see Fig. 4.12. Transforming the trajectories onto one with a fixed common center of mass of the two particles, one realizes that the collision is effectively driven by half of the force difference, $\frac{1}{2}(\vec{F}^{(A)} - \vec{F}^{(B)}) = -\frac{1}{2}\Delta\vec{F}$ for A particles and $\frac{1}{2}(\vec{F}^{(B)} - \vec{F}^{(A)}) = \frac{1}{2}\Delta\vec{F}$ for B particles. A transition towards patterned lanes is expected if $|\Delta\vec{F}|/2$ is larger than a typical *average force* between A and B particles, and lane formation is induced. The latter force depends both on density and on the external fields themselves. We estimate a typical average force between two opposite particles by considering different "effective" interparticle spacings. The first typical interparticle spacing is set by the density alone, $a = \rho^{-1/2}$. Including fluctuations in the interparticle distance induced by a finite temperature results in a further smaller effective average distance $\tilde{a}$ as obtained by setting a typical interparticle energy equal to $V(a) + k_B T$. Hence $\tilde{a} = V^{-1}\left[V(a) + k_B T\right]$ where V^{-1} is the inverse function of the interaction potential

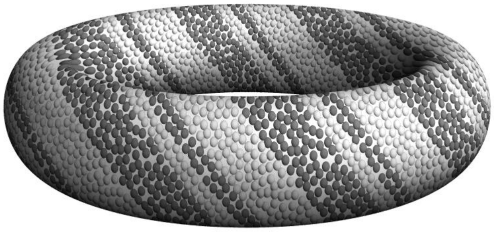

Figure 4.11: Visualization of the two-dimensional system by mapping a two-dimensional simulation snapshot onto the surface of a torus. A particles (light gray) are drifting along the torus, while B particles (dark gray) are drifting around it. The lanes are moving perpendicular to their direction.

$V(r)$. Finally the presence of the external fields enforces an even smaller averaged distance a' between two colliding opposite particles. We estimate this minimum distance a' by adding the net force per colliding particle $\Delta F/2$ to the force at distance $\tilde{a}$ via

$$a' = F^{-1}\left[\Delta F/2 + F(\tilde{a})\right], \tag{4.27}$$

where F^{-1} is the inverse function of $F(r) = -\frac{d}{dr}V(r)$. In general, an AB particle pair will not collide directly along $\Delta\vec{F}/2$ such that the actual average distance is between a' and $\tilde{a}$. Hence the averaged force $\overline{f}$ between an A and a B particle is roughly

$$\overline{f} = \frac{1}{\tilde{a} - a'}[V(a') - V(\tilde{a})]. \tag{4.28}$$

The critical force difference ΔF_{c} is reached when it becomes of the order of the mean force $\overline{f}$,

$$\Delta F_{\mathrm{c}} = 2\lambda\overline{f}. \tag{4.29}$$

$\lambda = 2$ is a dimensionless prefactor which is determined by an optimal fit to all simulation results for parallel forces in sec. 4.2.

The basic prediction of this simple theory is that the only essential parameter governing tilted lane formation is the magnitude $|\Delta\vec{F}|$. This prediction can be tested by simulation. In fact, in Fig. 4.10, the critical value of $|\Delta\vec{F}|$ is shown for different ratios $q = |\vec{F}^{(A)}|/|\vec{F}^{(B)}|$. Were the theory correct, all the simulation data should fall on a horizontal line independent

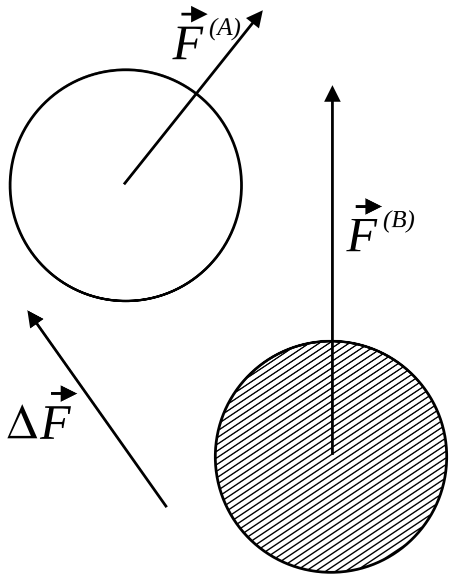

Figure 4.12: Sketch of two colloids of opposite type colliding due to the external fields $\vec{F}^{(A)}$ and $\vec{F}^{(B)}$. The A particle is white, while the B particle is gray. The particles collide effectively in direction of the difference force $\Delta\vec{F} = \vec{F}^{(B)} - \vec{F}^{(A)}$ as seen from a fixed center-of-mass.

of q. As can be deduced from Fig. 4.10, this is indeed confirmed. Furthermore, the actual magnitude predicted from the theory is in line with the simulation data. Note that - as far as the nonparallel case is concerned - there is no fit parameter involved. The global fit parameter λ is solely adjusted to the case of parallel forces.

Three-dimensional model

The model and all methods and arguments can readily be generalized to three spatial dimensions. Similar conclusions hold for the formation of tilted lanes. We have also performed computer simulations in a cubic box in three dimensions and observed tilted lane formation. Results are presented in Fig. 4.13: tilted lane formation is clearly visible in the plane spanned by the two forces $\vec{F}^{(A)}$ and $\vec{F}^{(B)}$, see Fig. 4.3(a). Perpendicular to the direction $\Delta\vec{F}$ of the lanes, the system shows a structure reminiscent of two-dimensional spinodal decomposition, see Fig. 4.13(b). The parameters are for these snapshots $\kappa = 4.0$, $V_0 = 2.5k_BT$ and $\rho\sigma^3 = 1$. In conclusion, this shows that pattern formation is a general effect which is independent of the dimensionality of the model.

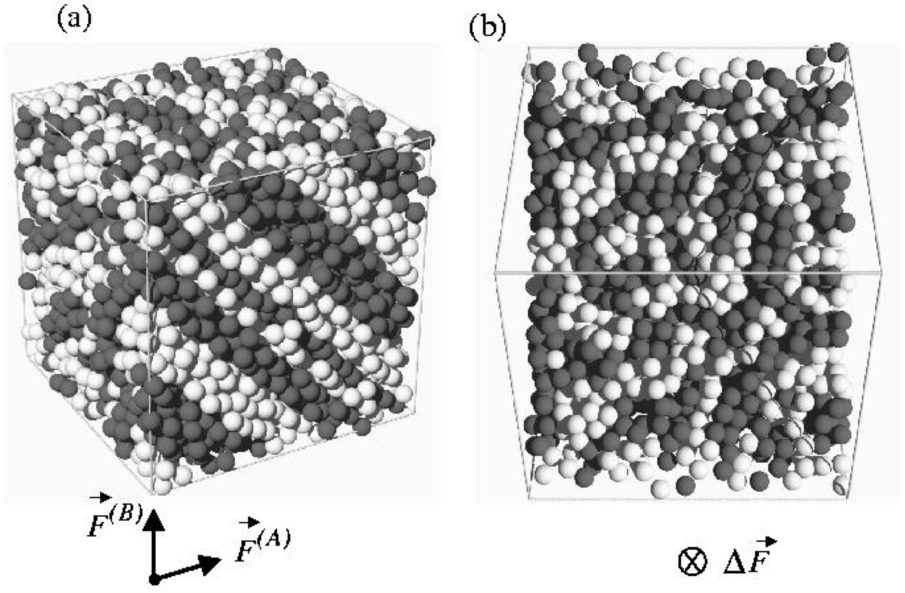

Figure 4.13: Typical snapshots of the three-dimensional system with perpendicular external fields above the critical force difference. The magnitude of the forces is $|\vec{F}^{(A)}| = |\vec{F}^{(B)}| = 150 k_B T/\sigma$. (a) Three-dimensional view, (b) look on the plane perpendicular to the $\Delta\vec{F}$ vector.

4.4 Reentrant freezing for a driven Brownian crystal

In this section we focus on a Brownian *crystal* which is driven by an external field. To this end, the external fields acting onto A and B particles are parallel ($\vec{F}^{(A)} = -\vec{F}^{(B)} = f\vec{e}_y$) but in contrast to the considerations in sec. 4.2 the field-free equilibrium initial state is a triangular crystal. The case of a fluid field-free configuration is easier as rotational symmetry with respect to the direction of the external field applied is ensured. This is no longer true for a crystal where one has to specify the field direction with respect to the crystalline orientation resulting in an anisotropy which reflects the crystalline symmetry. Clearly, in the absence of any external field, A and B particles are indistinguishable; hence the equilibrium state is randomly occupied triangular crystal. In the other limit of very strong fields, one expects again phase separation into completely demixed A and B regions. Once they are demixed, they follow Boltzmann statistics. Consequently the equilibrium state is a pure A (or B) crystal of the same lattice than the original (field free) one. What is less clear intuitively is how the system transforms from the first randomly occupied crystal into the demixed crystal if the field is turned continuously on. At least two scenarios are conceivable: either the system retains the underlying solid lattice but particle exchange hopping processes generated by the external field demix the crystalline state or the crystal first melts mechanically via the external field and then crystallizes again. In our simulations we almost exclusively observed the latter scenario.

In order to detect a triangular crystalline order we define a suitable crystallinity order parameter Ψ_6 that probes sixfold symmetry around a given particle via [154, 155]

$$\Psi_6 = \left| \left\langle \frac{1}{12N} \sum_{j=1}^{2N} \sum_{<k>} e^{6i\phi_{jk}} \right\rangle \right| . \tag{4.30}$$

Here the k-sum includes the six nearest neighbors of the given particle and the j-sum extends over $2N$ particles in the simulation box. The large angular brackets indicate a time average. ϕ_{jk} is the polar angle of the interparticle distance vector with respect to a fixed reference frame. For ideal sixfold symmetry, i.e., for a perfect triangular crystal, $\Psi_6 = 1$. Thermal fluctuations cause deviations from this ideal case but a value of $\Psi_6 > 0.8$ [154, 155] is conveniently taken to be conclusive evidence for a triangular crystal.

In Fig. 4.14 we plot Ψ_6 versus the difference external force $f^* = |\vec{F}^{(B)}|\sigma/k_BT$ for fixed parameters $\kappa = 4.0, V_0 = 15.0k_BT$, and $\rho\sigma^2 = 1$. The direction of the force is (11)-direction of the triangular crystal. Note that in contrast to the parameters used in section 4.3, the interactions energy is much larger to ensure that the equilibrium field-free state is crystalline. Indeed the crystallinity order parameter in the field-free case is around $\Psi_6 = 0.87$. Upon increasing the external field strength to $f^* \approx 10$, the crystallinity order parameter sharply drops down and stays to values close to zero indicating a melting of the crystal induced by the

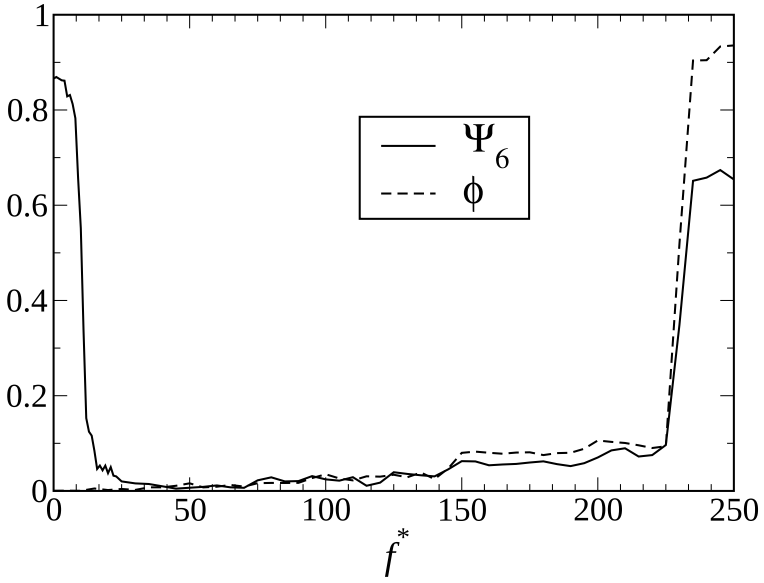

Figure 4.14: Crystallinity order parameter Ψ_6 (solid line) and lane order parameter ϕ (dashed line) plotted versus reduced external force f^* as calculated by a Brownian dynamics simulation.

external field. This melting process is mainly caused by a mechanical stress induced by the external field with respect to AB particle pairs. As the field is getting larger ($f^* \gtrsim 200$), the order parameter Ψ_6 increases again to values close to 0.7. This is accompanied with lane formation as indicated by a drastic increase of another order parameter ϕ defined in Ref. [153] which is sensitive to lane formation. The whole scenario is illustrated also by simulation snapshots shown in Fig. 4.15. While Fig. 4.15(a) corresponds to a field-free randomly mixed crystal, Fig. 4.15(b) and (c) are in the molten state while Fig. 4.15(d) represents a refrozen demixed crystal sliding against each other. In Fig. 4.15(b) and 4.15(c) worm like structures along the fields occur as a precursor to lanes formed by solids. Consequently we have shown evidence for a *reentrant freezing* behavior generated by external fields in nonequilibrium. A qualitative similar situation occurs for colloidal solids in linear shear flow [156, 157, 158]. A continuous increase of the shear rate can lead to shear-melting and subsequent recrystallization into a different solid structure [137, 159, 160]. A similar effect is shear thinning and subsequent shear thickening as observed in colloidal fluids for increasing shear rates [161].

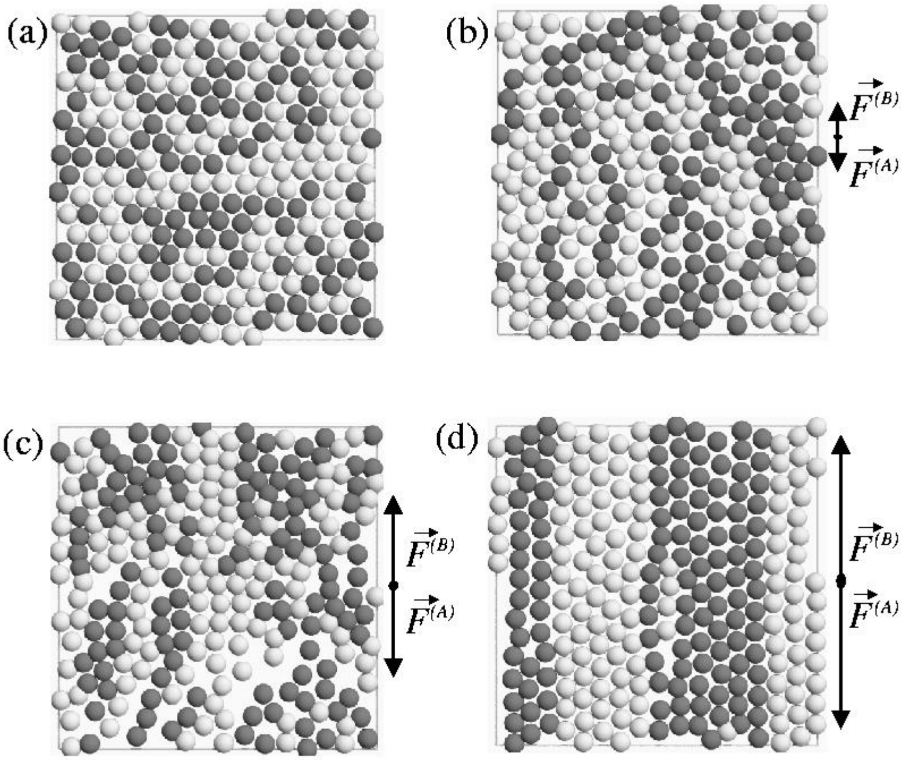

Figure 4.15: Snapshots of the two-dimensional system for different external forces, starting with a solid in the free-field state. The forces acting on the two different particle types are pointing into opposite directions. The forces are (a) $f^* = 0$, (b) $f^* = 50$, (c) $f^* = 150$, (d) $f^* = 250$. In (a) and (d), the system shows a solid structure, while in (b) and (c) the system is a homogeneously fluid. Here the total number of particles is $2N = 250$.

4.5 Summary

In conclusion we have studied the influence of an external field on a binary colloidal mixture performing Brownian dynamics in a solvent with simulation and simple theory. It was shown that oppositely driven particles avoid each other by forming different lanes due to a nonequilibrium slip-stream effect. Using a suitable order parameter this was identified as a first-order nonequilibrium phase transformation. A simple scaling theory was proposed whose predictions and trends were confirmed by our simulation data. The process of lane formation was found to be very general: it prevails for oscillating fields provided the frequency is not too small and it is present both in two and three spatial dimensions. Hence, it should be observable in real systems such as binary colloidal dispersions, e.g., driven by an oscillatory electric field. We have generalized our studies of nonequilibrium pattern formation in continuum driven diffusive mixtures to nonparallel external fields and crystalline states. As main results we found tilted lanes along the force difference vector which are moving with a constant interface velocity provided the external force difference is large enough. Furthermore, a solid melts and refreezes if the magnitude of an external field is increased.

Chapter 5

Summary and Outlook

In summary, we have examined the structure and phase behavior of binary colloidal mixtures in equilibrium and nonequilibrium. As a model for a binary colloidal system in equilibrium we investigated a mixture of star polymers and hard-sphere colloids interpolating between the well known colloid-polymer and binary hard-sphere mixtures. First of all we presented analytic results for the force between a colloid and a star polymer in a good solvent, accompanied with an analytic expression for the corresponding pair potential which is valid for size ratios $q \lesssim 0.7$. The validity of these expressions was established by direct comparison with Molecular Dynamics simulations. Our theoretical approach is in principle generalizable to arbitrary geometrical shapes for the hard particle, thus opening up the possibility for studying effective forces between stars and hard ellipsoids, platelets etc. Further, a revised form for the star-star interaction for small functionalities has been presented, while at the same time the logarithmic-Yukawa form of this interaction remains valid for functionalities $f \gtrsim 10$. Using these interactions we have traced out the phase diagram of star-polymer–colloid mixtures, establishing the limits of stability of the demixing binodals as functions of the star functionality and the size ratio, for the case in which the star-polymers are smaller than the colloids. We have demonstrated the equivalence of a two-component approach with a depletion picture, in which the stars are further traced out. Star polymers have been shown to fulfill their unique role as natural bridging systems between soft polymers (for low f) and colloidal particles (at high f). Hence, they can act as selective depletants between colloidal hard spheres. All our findings can be experimentally checked by carefully preparing mixtures of index-matched hard sphere colloids with monodisperse star-polymers in good solvents [98]. The stability of the demixing with respect to freezing has been recently studied in some generality in the framework of the model of non-additive hard spheres [17, 126, 127]. Whether the present system can also fit within this picture remains to be seen. Our work is limited to star-colloid size ratios smaller than unity, since the star-colloid interactions employed here are derived under the assumption that the star never ‘crawls over’ the colloidal hard sphere. [162] The investigation of the opposite case, in which the small colloids can fully penetrate into the corona of the star-polymers [128] is also a problem for the future.

As a nonequilibrium system we have studied the influence of an external field on a binary colloidal mixture performing Brownian Dynamics in a solvent with simulation and simple theory. It was shown that oppositely driven particles avoid each other by forming different lanes due to a non-equilibrium slip-stream effect. Using a suitable order parameter this was identified as a first-order non-equilibrium phase transformation. A simple scaling theory was proposed whose predictions and trends were confirmed by our simulation data. The process of lane formation was found to be very general: it prevails for oscillating fields provided the frequency is not too small and is present both in two and three spatial dimensions. Hence it should be observable in real systems such as binary colloidal dispersions e.g. driven by an oscillatory electric field.

We generalized our studies of non-equilibrium pattern formation in continuum driven diffusive mixtures to non-parallel external fields and crystalline states. As main results we found tilted lanes along the force difference vector which are moving with a constant interface velocity provided the external force difference is large enough. Furthermore, a solid melts and refreezes if the magnitude of an external field is increased.

Let us remark on possibilities of non-equilibrium lane formation in more complicated systems: first, our studied system was completely symmetric involving the same partial densities and the same particle-particle interactions. For experimental realizations [48, 49, 51, 50] this will not be fulfilled in general. However, the basic physics of lane formation will not change. Secondly, if ternary and further multicomponent mixture beyond binary ones are considered, we expect cascades of lane formation transitions involving the different particles species as the external field is increased.

We finally comment on possible experimental realizations of our model: There are different fields where the pattern formation we predicted within our model can be verified, namely in colloidal dynamics and in pedestrian motion. *Binary colloidal mixtures* indeed can be driven by constant external forces. Important examples for parallel forces are sedimentation where the external force is gravity [48, 49] or electrokinetic motion of charged colloids [163] where the external force is an electric field. Both the fluid and crystalline field-free state can be studied. A recent realization with mixed crystals can be found in [164]. One possible drawback is the hydrodynamic backflow [165] caused by strong hydrodynamic interactions [166, 167, 168] which were neglected in our model. An overall backflow can be avoided by a time dependent oscillatory field (e.g. AC electric field) which leads qualitatively to the same lane formation if its frequency is small enough [153]. We further think that the long-ranged hydrodynamic flow around a driven colloidal particle will favor lane formation, i.e. the critical field strength needed to generate lane formation is expected to be lower than with hydrodynamic interactions neglected. Colloids can also be exposed to external laser-optical and magnetic fields [55] which generate external forces in a controlled way coupling to the dielectricity (resp. the magnetic permeability) of the colloidal material. Nonparallel external forces in colloidal mixtures can be realized by crossing two external fields e.g. gravity with electric, laser-optical with electric, laser-optical with magnetic etc.

The two species of a colloidal mixture will in general respond differently to the two external fields such that the resulting total external force will be different in direction.

A different realization is *dynamics of pedestrians* in pedestrian zones and in lecture halls. Similar off-lattice models involving Brownian particles have been used to simulate the collective behavior of pedestrians [47, 169] including escape panic [170]. Our setup of perpendicular external fields is realized by two crossing pedestrian lanes in which pedestrians are only moving in one direction. Based on our results, we would expect tilted lane formation provided the density of the pedestrians is high enough. Finally it would be interesting to extend phenomenological hydrodynamical theories which predict lane formation for parallel forces via an instability [171, 49, 172, 173, 174, 175, 176, 129, 177] to the case of tilted forces. Even more challenging would be a full microscopic non-equilibrium theory which has been much more elaborated for second-order non-equilibrium phase transitions [38, 178]. Work along these lines is in progress.

We finish with a couple of points: first, lane formation is also expected to occur in three-component colloidal systems and - in general - for polydisperse samples. The formation of lanes could provide an efficient channel to transport specific particles into a preferred direction by driving the system via an external field. Second, one might surmise that lane formation will also occur in lattice models if other kinds than square lattices are used or if next-nearest neighbor hopping processes are allowed in the lattice model. This conjecture is based on the observation that shear forces between different lanes are driving the lane formation which are absent in a square-lattice model with nearest-neighbor hopping. Third, lane formation should also be stable with respect to a change of the particle dynamics. For instance, the transition is expected to be stable also if Fokker-Planck [140] rather than Brownian dynamics is used. The only requirement should be a parallel dynamics for all particles.

List of Abbreviations

AO	Asakura-Oosawa
BHS	Binary Hard-Sphere (mixture)
CP	Colloid-Polymer (mixture)
CS	Carnahan Starling
dcf	direct correlation function
DFT	Density Functional Theory
FENE	Finite Extensible Nonlinear Elastic
HNC	Hypernetted Chain
HS	Hard Spheres
MC	Monte Carlo
MD	Molecular Dynamics
MFA	Meanfield Approximation
OZ	Ornstein-Zernike
PB	Polybutadiene
PMMA	Polymethylmethacrylate
PY	Percus-Yevick
RY	Rogers-Young
SA	Superposition Approximation
SANS	Small Angle Neutron Scattering
SAXS	Small Angle X-ray Scattering
SLS	Static Light Scattering

Appendix A

Integral equation theories for multicomponent mixtures

Let us give a brief outline regarding integral equation theories for multicomponent mixtures. Consider, in general, a ν-component liquid mixture, consisting of $N_1, N_2, \ldots, N_\nu$ particles of species $1, 2, \ldots, \nu$, respectively, enclosed in the macroscopic volume V. The partial density ρ_i of species i, is given by $\rho_i = N_i/V$. The pair structure of the system is fully described by $\nu(\nu+1)/2$ independent correlation functions $h_{ij}(r)$, $i \leq j = 1, 2, \ldots, \nu$, because symmetry with respect to exchange of the indices dictates $h_{ij}(r) = h_{ji}(r)$. Associated with the total correlation functions are the direct correlation functions (dcf's) $c_{ij}(r)$. For the same reasons, there exist only $\nu(\nu+1)/2$ independent dcf's. The Fourier transforms of $h_{ij}(r)$ and $c_{ij}(r)$ are denoted by $\tilde{h}_{ij}(k)$ and $\tilde{c}_{ij}(k)$, respectively.

The OZ relation for one-component systems at density ρ takes in Fourier space the algebraic form

$$\tilde{h}(k) = \tilde{c}(k) + \tilde{c}(k)\; \rho\; \tilde{h}(k), \tag{A.1}$$

where $\tilde{h}(k)$ and $\tilde{c}(k)$ are the Fourier transforms of the total and direct correlation functions $h(r)$ and $c(r)$, respectively. The generalization of the OZ relation for multicomponent mixtures reads as [179]:

$$\tilde{\boldsymbol{H}}(k) = \tilde{\boldsymbol{C}}(k) + \tilde{\boldsymbol{C}}(k) \cdot \boldsymbol{D} \cdot \tilde{\boldsymbol{H}}(k), \tag{A.2}$$

where $\tilde{\boldsymbol{H}}(k)$ and $\tilde{\boldsymbol{C}}(k)$ are $\nu \times \nu$ symmetric matrices with elements:

$$[\tilde{\boldsymbol{H}}(k)]_{ij} = \tilde{h}_{ij}(k) \quad \text{and} \quad [\tilde{\boldsymbol{C}}(k)]_{ij} = \tilde{c}_{ij}(k), \tag{A.3}$$

and $\boldsymbol{D}$ is a $\nu \times \nu$ diagonal matrix of the partial densities:

$$[\tilde{\boldsymbol{D}}]_{ij} = \rho_i \delta_{ij}. \tag{A.4}$$

Eq. (A.2) above generates $\nu(\nu+1)/2$ independent algebraic equations for the $\nu(\nu+1)$ unknown functions $\tilde{h}_{ij}(k)$ and $\tilde{c}_{ij}(k)$. The system becomes in principle solvable if one provides additional $\nu(\nu+1)/2$ *closure equations* between these functions. For example, the Rogers-Young closure generalization to multicomponent mixtures reads as

$$g_{ij}(r) = \exp\left[-\beta v_{ij}(r)\right]\left[1 + \frac{\exp\left[\gamma_{ij}(r) f_{ij}(r)\right] - 1}{f_{ij}(r)}\right] \qquad (i = 1, 2, \ldots, \nu \text{ and } i \leq j), \tag{A.5}$$

where $g_{ij}(r) = h_{ij}(r) + 1$, $\gamma_{ij}(r) = h_{ij}(r) - c_{ij}(r)$ and $v_{ij}(r)$ is the pair interaction between species i and j. The 'mixing function' $f_{ij}(r)$ is given by:

$$f_{ij}(r) = 1 - \exp\left(-\alpha_{ij} r\right). \tag{A.6}$$

Usually, a *single* self-consistency parameter $\alpha_{ij} =: \alpha$ is employed for all components, so that $f_{ij}(r) = f(r)$, as there is a single thermodynamic consistency requirement to be fulfilled, i.e., the equality of the 'virial' and 'fluctuation' total compressibilities of the mixture. Yet, multi-parameter generalizations of the RY closure have also been proposed [14], invoking the partial compressibilities of the individual components. For $\alpha = 0$ one recovers the Percus-Yevick (PY) and for $\alpha = \infty$ the Hypernetted Chain (HNC) multicomponent closures [36] For a HS mixture, the PY closure is analytically solvable [180, 181, 182].

Appendix B

On the $x \to 0$ and $x \to 1$ limits of the Gibbs free energy

In this Appendix we present some technical details necessary for the solution of the second-order differential equation (3.4). With the Gibbs free energy per particle

$$g(x) = \frac{G(x, T, P)}{N}, \tag{B.1}$$

we seek to solve the equation [91]:

$$g''(x) = \frac{k_B T}{S_{\text{con}}(k=0)}, \tag{B.2}$$

where it is implied that the pressure P and the temperature T are constant.

The concentration structure factor $S_{\text{con}}(k)$ for a colloid-star mixture of partial concentrations x_{c} and x_{s} is defined as:

$$\begin{aligned} S_{\text{con}}(k) &= \frac{1}{N}\left\langle [x_{\text{s}}\rho_{\text{c}}(\boldsymbol{k}) - x_{\text{c}}\rho_{\text{s}}(\boldsymbol{k})]\,[x_{\text{s}}\rho_{\text{c}}(-\boldsymbol{k}) - x_{\text{c}}\rho_{\text{s}}(-\boldsymbol{k})]\right\rangle \\ &= x_{\text{s}}^2\frac{1}{N}\left\langle \rho_{\text{c}}(\boldsymbol{k})\rho_{\text{c}}(-\boldsymbol{k})\right\rangle + x_{\text{c}}^2\frac{1}{N}\left\langle \rho_{\text{s}}(\boldsymbol{k})\rho_{\text{s}}(-\boldsymbol{k})\right\rangle - 2x_{\text{c}}x_{\text{s}}\frac{1}{N}\left\langle \rho_{\text{c}}(\boldsymbol{k})\rho_{\text{s}}(-\boldsymbol{k})\right\rangle, \end{aligned} \tag{B.3}$$

where $\rho_{\text{c}}(\boldsymbol{k})$ is defined through Eq. (3.20) and similarly for $\rho_{\text{s}}(\boldsymbol{k})$.

We define the partial structure factors $S_{ij}(k)$ as $S_{ij}(k) = \delta_{ij} + \sqrt{\rho_i\rho_j}\tilde{h}_{ij}(k)$, $i, j = \text{c}, \text{s}$. It can be shown [36] that these $S_{ij}(k)$'s satisfy the equations:

$$x_{\text{c}}S_{\text{cc}}(k) = \frac{1}{N}\left\langle \rho_{\text{c}}(\boldsymbol{k})\rho_{\text{c}}(-\boldsymbol{k})\right\rangle; \tag{B.4}$$

$$x_{\text{s}}S_{\text{ss}}(k) = \frac{1}{N}\left\langle \rho_{\text{s}}(\boldsymbol{k})\rho_{\text{s}}(-\boldsymbol{k})\right\rangle; \tag{B.5}$$

$$\sqrt{x_{\text{c}}x_{\text{s}}}S_{\text{cs}}(k) = \frac{1}{N}\left\langle \rho_{\text{c}}(\boldsymbol{k})\rho_{\text{s}}(-\boldsymbol{k})\right\rangle. \tag{B.6}$$

From Eqs. (B.3) - (B.6) we obtain

$$S_{\rm con}(k) = x_{\rm c}x_{\rm s}^2 S_{\rm cc}(k) + x_{\rm s}x_{\rm c}^2 S_{\rm ss}(k) - 2(x_{\rm c}x_{\rm s})^{3/2} S_{\rm cs}(k). \tag{B.7}$$

We now set $x_{\rm s} = x$, $x_{\rm c} = 1 - x$ and introduce the total density ρ of the mixture, related to the partial densities through $\rho_{\rm c} = (1 - x)\rho$ and $\rho_{\rm s} = x\rho$. Using $S_{ij}(k) = \delta_{ij} + \sqrt{\rho_i\rho_j}\tilde{h}_{ij}(k)$ and Eqs. (B.2) and (B.7) above, we obtain:

$$\beta g''(x) = \left\{x^2(1-x)[1+(1-x)\rho\tilde{h}_{\rm cc}(0)] + x(1-x)^2[1+x\rho\tilde{h}_{\rm ss}(0)] - 2x^2(1-x)^2\rho\tilde{h}_{\rm cs}(0)\right\}^{-1} \tag{B.8}$$

The quantities $\tilde{h}_{ij}(0)$ are all finite and so is ρ. An analysis of the limiting behavior of the rhs of Eq. (B.8) above, shows that it diverges as $1/x$ for $x \to 0$ and as $1/(1-x)$ for $x \to 1$. In order to circumvent this technical difficulty at the two boundaries of integration and deal always with finite values, we split the Gibbs free energy per particle $g(x)$ into the ideal part, $g_{\rm id}(x)$, and the excess part, $g_{\rm ex}(x)$, as follows:

$$\begin{aligned} \beta g(x) &= \beta g_{\rm id}(x) + \beta g_{\rm ex}(x) = (1-x)\beta\mu_{\rm c,id}(x) + x\beta\mu_{\rm s,id}(x) + \beta g_{\rm ex}(x) \\ &= (1-x)\ln\left[(1-x)\rho\sigma_{\rm c}^3\right] + x\ln\left(x\rho\sigma_{\rm c}^3\right) + \beta g_{\rm ex}(x) + 3(1-x)\ln\left(\frac{\Lambda_{\rm c}}{\sigma_{\rm c}}\right) + 3x\ln\left(\frac{\Lambda_{\rm s}}{\sigma_{\rm c}}\right) \\ &= (1-x)\ln(1-x) + x\ln x + \beta g_{\rm ex}(x) + C_1 x + C_0, \end{aligned} \tag{B.9}$$

where $\Lambda_{\rm c,s}$ are the thermal de Broglie wavelengths of the colloids and stars, respectively, and in the last line we have simply introduced two constants, C_0 and C_1 for a term in $g(x)$ that is linear in x and plays no role, neither in the argument that follows nor in the determination of phase boundaries. Taking the second derivative in Eq. (B.9) above, we obtain

$$\beta g''(x) = \frac{1}{x} + \frac{1}{1-x} + g''_{\rm ex}(x). \tag{B.10}$$

Thus, the $1/x$-divergence at $x \to 0$ and the $1/(1-x)$-divergence at $x \to 1$ manifest also in Eq. (B.8) above, are seen to arise from the ideal part of the Gibbs free energy. Hence, a second-order differential equation for which all terms that appear are free of divergences can be written, which reads as

$$\beta g''_{\rm ex}(x) = \frac{1}{S_{\rm con}(k=0)} - \left(\frac{1}{x} + \frac{1}{1-x}\right). \tag{B.11}$$

We solved therefore numerically Eq. (B.11) for the determination of the function $g_{\rm ex}(x)$; addition of the analytically known term $g_{\rm id}(x)$ delivers the total Gibbs free energy per particle.

Bibliography

[1] We ignore here the possibility of formation of a quasicrystal because, in practice, quasicrystal-forming materials are usually ternary mixtures.

[2] L. D. Landau and E. M. Lifshitz, *Course of Theoretical Physics: Statistical Physics, Vol. 5, 3rd ed.* (Pergamon, Oxford, 1980).

[3] P. N. Pusey, in *Liquids, Freezing and the Glass Transition*, edited by D. L. J. P. Hansen and J. Zinn-Justin (North Holland, Amsterdam, 1991).

[4] M. Dijkstra, Curr. Opinion Colloid Interface Sci. **6**, 372 (2001).

[5] S. Asakura and F. Oosawa, J. Polymer Sci. **33**, 183 (1958).

[6] A. Vrij, Pure Appl. Chem. **48**, 471 (1976).

[7] A. P. Gast, C. K. Hall, and W. B. Russel, J. Coll. Inter. Sci. **96**, 251 (1983).

[8] H. N. W. Lekkerkerker, W. C. K. Poon, P. N. Pusey, A. Stroobants, and P. B. Warren, Europhys. Lett. **20**, 559 (1992).

[9] M. Dijkstra, J. M. Brader, and R. Evans, J. Phys.: Condens. Matter **11**, 10079 (1999).

[10] M. Schmidt, H. Löwen, J. M. Brader, and R. Evans, Phys. Rev. Lett. **85**, 1934 (2000).

[11] A. A. Louis, R. Finken, and J.-P. Hansen, Europhys. Lett. **46**, 741 (1999).

[12] S. M. Ilett, A. Orrock, W. C. K. Poon, and P. N. Pusey, Phys. Rev. E **51**, 1344 (1995).

[13] A. Moussaïd, W. C. K. Poon, P. N. Pusey, and M. F. Soliva, Phys. Rev. Lett. **82**, 225 (1999).

[14] T. Biben and J.-P. Hansen, J. Phys.: Condens. Matter **3**, F65 (1991).

[15] M. Dijkstra, R. van Roij, and R. Evans, Phys. Rev. Lett. **81**, 2268 (1998).

[16] M. Dijkstra, R. van Roij, and R. Evans, Phys. Rev. E **59**, 5744 (1999).

[17] R. Roth, R. Evans, and A. A. Louis, Phys. Rev. E **64**, 051202 (2001).

[18] S. W. Rick and A. D. J. Haymet, J. Chem. Phys. **90**, 1188 (1989).

[19] A. R. Denton and N. W. Ashcroft, Phys. Rev. A **42**, 7312 (1990).

[20] X. C. Zeng and D. Oxtoby, J. Chem. Phys. **93**, 4357 (1990).

[21] C. N. Likos, Phys. Rep. **348**, 267 (2001).

[22] B. Götzelmann, R. Roth, S. Dietrich, M. Dijkstra, and R. Evans, Europhys. Lett. **47**, 398 (1999).

[23] R. Roth, R. Evans, and S. Dietrich, Phys. Rev. E **62**, 5360 (2000).

[24] R. Seghrouchni, G. Petekidis, D. Vlassopoulos, G. Fytas, A. N. Semenov, J. Roovers, and G. Fleischer, Europhys. Lett. **42**, 271 (1998).

[25] C. N. Likos, H. Löwen, M. Watzlawek, B. Abbas, O. Jucknischke, J. Allgaier, and D. Richter, Phys. Rev. Lett. **80**, 4450 (1998).

[26] A. Jusufi, M. Watzlawek, and H. Löwen, Macromolecules **32**, 4470 (1999).

[27] C. N. Likos, H. Löwen, A. Poppe, L. Willner, J. Roovers, B. Cubitt, and D. Richter, Phys. Rev. E **58**, 6299 (1998).

[28] J. Stellbrink, B. Abbas, J. Allgaier, M. Monkenbusch, D. Richter, C. N. Likos, H. Löwen, and M. Watzlawek, Progr. Coll. Polym. Sci. **110**, 25 (1998).

[29] J. Stellbrink, J. Allgaier, M. Monkenbusch, D. Richter, A. Lang, C. N. Likos, M. Watzlawek, H. Löwen, G. Ehlers, and P. Schleger, Progr. Coll. Polym. Sci. **115**, 88 (2000).

[30] K. Shida, K. Ohno, M. Kimura, and Y. Kawazoe, Macromolecules **33**, 7655 (2000).

[31] C. von Ferber, A. Jusufi, M. Watzlawek, C. N. Likos, and H. Löwen, Phys. Rev. E **62**, 6949 (2000).

[32] C. von Ferber, A. Jusufi, C. N. Likos, H. Löwen, and M. Watzlawek, Eur. Phys. J. E **2**, 311 (2000).

[33] M. P. Allen and D. J. Tildesley, *Computer Simulations of Liquids* (Clarendon Press, Oxford, 1989).

[34] M. Baus, L. Rull, and J. Ryckaert, eds., *Observations, Prediction and Simulation of Phase Transitions in Complex Fluids*, vol. Series B: Physics (Kluwer Academic Publishers, Dordrecht, 1995).

[35] H. Löwen, Phys. Rep. **237**, 249 (1994).

[36] J. P. Hansen and I. R. McDonald, *Theory of Simple Liquids* (Academic Press, London, 1986), 2 ed.

[37] S. Katz, J. Lebowitz, and H. Spohn, Phys. Rev. B **28**, 1655 (1983).

[38] B. Schmittmann and R. K. P. Zia, in *Phase Transitions and Critical Phenomena*, vol. 17 (Academic Press, London, 1995), ed. by C. Domb and J. Lebowitz.

[39] J. Marro and R. Dickman, in *Phase Transitions and Critical Phenomena* (University Press, Cambridge, 1999), ed. by C. Godreche.

[40] S. W. Sides, P. A. Rikvold, and M. A. Novotny, Phys. Rev. Lett. **81**, 834 (1998).

[41] B. K. Chakrabarti and M. Acharyya, Rev. Mod. Phys. **71**, 847 (1999).

[42] R. A. Monetti and E. V. Albano, Physica A **280**, 382 (2000).

[43] M. Aertsensa and J. Naudts, J. Stat. Phys. **62**, 609 (1991).

[44] B. Schmittmann, K. Hwang, and R. K. P. Zia, Europhys. Lett. **19**, 19 (1992).

[45] I. Vilfan, B. Schmittmann, and R. K. P. Zia, Phys. Rev. Lett. **73**, 2071 (1994).

[46] T. Mullin, Phys. Rev. Lett. **84**, 4741 (2000).

[47] D. Helbing, I. J. Farkas, and T. Vicsek, Phys. Rev. Lett. **84**, 1240 (2000).

[48] R. H. Weiland, Y. P. Fessas, and B. V. Ramaro, J. Fluid. Mech. **142**, 383 (1984).

[49] G. K. Batchelor and R. W. J. van Rensburg, J. Fluid. Mech. **166**, 379 (1986).

[50] H. A. Nasr-El-Din, J. H. Masliyah, and K. Nandakumar, Canad. J. Chem. Engin. **11**, 1003 (1999).

[51] Y. Yan and J. H. Masliyah, Intern. J. Multiphase Flow **19**, 875 (1993).

[52] D. Helbing and P. Molnár, Phys. Rev. E **51**, 4282 (1995).

[53] H. Löwen, Physica A **235**, 129 (1997).

[54] W. Götze, J. Phys.: Condens. Matter **11**, A1 (1999).

[55] H. Löwen, J. Phys.: Condens. Matter **13**, R 415 (2001).

[56] C. A. Murray and D. H. van Winkle, Phys. Rev. Lett. **58**, 1200 (1987).

[57] G. M. K. Zahn, R. Lenke, Phys. Rev. Lett. **82**, 2721 (1999).

[58] A. H. Marcus, J. Schofield, and S. A. Rice, Phys. Rev. E **60**, 5725 (1999).

[59] P. J. Flory, J. Chem. Phys. **10**, 51 (1942).

[60] P. J. Flory, J. Chem. Phys. **17**, 303 (1949).

[61] P. J. Flory, *Principles of Polymer Chemistry* (Cornell University Press, Ithaca, 1953).

[62] S. Asakura and F. Oosawa, J. Chem. Phys. **22**, 1255 (1954).

[63] A. A. Louis, P. G. Bolhuis, J.-P. Hansen, and E. J. Meijer, Phys. Rev. Lett. **85**, 2522 (2000).

[64] M. Fuchs and K. S. Schweizer, Europhys. Lett. **51**, 621 (2000).

[65] P. G. Bolhuis, A. A. Louis, J.-P. Hansen, and E. J. Meijer, J. Chem. Phys. **114**, 4296 (2001).

[66] P. Pincus, Macromolecules **24**, 2912 (1991).

[67] M. Daoud and J. P. Cotton, J. Physique **43**, 531 (1982).

[68] P. G. de Gennes, *Scaling Concepts in Polymer Physics* (Cornell University Press, Ithaca, 1979).

[69] E. Eisenriegler, *Polymers Near Surfaces* (World Scientific, Singapore, 1993).

[70] T. Bickel, C. M. Marques, and C. Jeppesen, Phys. Rev. E **62**, 1124 (2000).

[71] T. A. Witten, P. A. Pincus, and M. E. Cates, Europhys. Lett. **2**, 137 (1986).

[72] T. A. Witten and P. A. Pincus, Macromolecules **19**, 2509 (1986).

[73] E. Eisenriegler, Phys. Rev. E **55**, 3116 (1997).

[74] R. J. Hunter, *Foundations of Colloid Science*, vol. I (Clarendon Press, Oxford, 1986).

[75] M. P. Allen and D. J. Tildesley, *Computer Simulation of Liquids* (Clarendon Press, Oxford, 1987).

[76] G. S. Grest, K. Kremer, and T. A. Witten, Macromolecules **20**, 1376 (1987).

[77] G. S. Grest, Macromolecules **27**, 3493 (1994).

[78] S. Dietrich and H. W. Diehl, Z. Phys. B **43**, 315 (1981).

[79] K. Ohno and K. Binder, J. Phys. France **49**, 1329 (1988).

[80] H. W. Diehl and M. Shpot, Nucl. Phys. B **528**, 595 (1998).

[81] R. Hegger and P. Grassberger, J. Phys. A: Math. Gen. **27**, 4069 (1994).

[82] M. Watzlawek, C. N. Likos, and H. Löwen, Phys. Rev. Lett. **82**, 5289 (1999).

[83] M. Watzlawek, H. Löwen, and C. N. Likos, J. Phys.: Condens. Matter **10**, 8189 (1998).

[84] K. Ohno, Phys. Rev. A **40**, 1524 (1989).

[85] A. Y. Grosberg, P. G. Khalatur, and A. R. Khokhlov, Makromol. Chem. Rapid Commun. **3**, 709 (1982).

[86] L. Schäfer and A. Baumgärtner, J. Phys. (Paris) **47**, 1431 (1986).

[87] B. Krüger, L. Schäfer, and A. Baumgärtner, J. Phys. (Paris) **50**, 3191 (1989).

[88] K. Ohno, K. Shida, M. Kimura, and Y. Kawazoe, Macromolecules **29**, 2269 (1996).

[89] A. M. Rubio and J. J. Freire, Comp. Theor. Polymer Sci. **10**, 89 (2000).

[90] T. Biben and J.-P. Hansen, Phys. Rev. Lett. **66**, 2215 (1991).

[91] A. B. Bhatia and D. E. Thornton, Phys. Rev. B **2**, 3004 (1970).

[92] N. F. Carnahan and K. E. Starling, J. Chem. Phys. **51**, 635 (1969).

[93] A. Lang, C. N. Likos, M. Watzlawek, and H. Löwen, J. Phys.: Condens. Matter **12**, 5087 (2000).

[94] A. A. Louis, P. G. Bolhuis, and J.-P. Hansen, Phys. Rev. E **62**, 7961 (2000).

[95] C. N. Likos, A. Lang, M. Watzlawek, and H. Löwen, Phys. Rev. E **63**, 031206 (2001).

[96] J. Dzubiella, H. M. Harreis, C. N. Likos, and H. Löwen, Phys. Rev. E **64**, 011405 (2001).

[97] C. N. Likos and H. M. Harreis, Cond. Matt. Phys. **5**, 173-200 (2002).

[98] J. Dzubiella, A. Jusufi, C. N. Likos, C. von Ferber, H. Löwen, J. Stellbrink, J. Allgaier, D. Richter, A. B. Schofield, P. A. Smith, W. C. K. Poon, and P. N. Pusey, Phys. Rev. E **64**, 010401(R) (2001).

[99] L. Antl, J. W. Goodwin, R. Hill, R. H. Ottewill, S. M. Owens, S. Papworth, and J. A. Waters, Coll. Surf. **17**, 67 (1986).

[100] J. Allgaier, R. N. Young, V. Efstratiadis, and N. Hadjichristidis, Macromolecules **29**, 1794 (1996).

[101] N. Hadjichristidis and L. J. Fetters, Macromolecules **13**, 191 (1980).

[102] G. S. Grest, L. J. Fetters, J. S. Huang, and D. Richter, Adv. Chem. Phys. **XCIV**, 67 (1996).

[103] The neutron scattering was performed in *d*-cis decalin using D11 (ILL, Grenoble, France); *see experimental report 9-11-684* (2000).

[104] J. Stellbrink, J. Allgaier, A. B. Schofield, and P. Pusey, to be published.

[105] W. C. K. Poon, A. D. Pirie, and P. N. Pusey, Faraday Discuss. **101**, 65 (1995).

[106] I. D'Amico and H. Löwen, Physica A **237**, 25 (1997).

[107] E. Allahyarov, I. D'Amico, and H. Löwen, Phys. Rev. Lett. **81**, 1334 (1998).

[108] E. Allahyarov and H. Löwen, J. Phys.: Condens. Matter **13**, L277 (2001).

[109] A. A. Louis, R. Roth, E. Allahyarov, and H. Löwen, Phys. Rev. E **65**, 061407 (2002).

[110] R. Dickman, P. Attard, and V. Simonian, J. Chem. Phys. **107**, 205 ((1997).

[111] J. M. Méndez-Alcaraz and R. Klein, Phys. Rev. E **61**, 4095 (2000).

[112] A. König and N. W. Ashcroft, Phys. Rev. E **63**, 041203 (2001).

[113] J. Dzubiella, C. N. Likos, and H. Löwen, Europhys. Lett. **58**, 133-139 (2002).

[114] J. Dzubiella, C. N. Likos, and H. Löwen, J. Chem. Phys. **116**, 9518 (2002).

[115] P. Attard, J. Chem. Phys. **91**, 3083 (1989).

[116] K. R. Hall, J. Chem. Phys. **57**, 2252 (1972).

[117] J. A. Barker and D. Henderson, J. Chem. Phys. **47**, 4714 (1967).

[118] L. Verlet and J. J. Weis, Phys. Rev. A **5**, 939 (1972).

[119] J. M. Kincaid and J. J. Weis, Mol. Phys. **34**, 931 (1977).

[120] M. H. J. Hagen and D. Frenkel, J. Chem. Phys. **101**, 4093 (1994).

[121] L. Mederos and G. Navascués, J. Chem. Phys. **101**, 9841 (1994).

[122] T. Coussaert and M. Baus, Phys. Rev. E **52**, 862 (1995).

[123] A. Lang, G. Kahl, C. N. Likos, H. Löwen, and M. Watzlawek, J. Phys.: Condens. Matter **11**, 10143 (1999).

[124] S. Melchionna and J. P. Hansen, Phys. Chem. Chem. Phys. **2**, 3465 (2000).

[125] D. Goulding and S. Melchionna, Phys. Rev. E **64**, 011403 (2001).

[126] R. Roth and R. Evans, Europhys. Lett. **53**, 271 (2001).

[127] A. A. Louis and R. Roth, J. Phys.: Condens. Matter **13**, L777 (2001).

[128] A. Johner, J. F. Joanny, S. D. Orrite, and J. B. Avalos, Europhys. Lett. **56**, 549 (2001).

[129] M. C. Cross and P. C. Hohenberg, Rev. Mod. Phys. **65**, 851 (1993).

[130] W. van Saarloos, Phys. Rep. **301**, 9 (1998).

[131] G. P. Hoffmann and H. Löwen, Phys. Rev. E **60**, 3009 (1999).

[132] G. P. Hoffmann and H. Löwen, J. Phys.: Condens. Matter **13**, 9197 (2001).

[133] D. H. Rothman and S. Zaleski, Rev. Mod. Phys. **66**, 1417 (1994).

[134] H. Löwen, J. Phys.: Condens. Matter **4**, 10105 (1992).

[135] M. O. Robbins, K. Kremer, and G. S. Grest, J. Chem. Phys. **88**, 3286 (1988).

[136] E. J. Meijer and D. Frenkel, J. Chem. Phys. **94**, 2269 (1991).

[137] M. J. Stevens and M. O. Robbins, J. Chem. Phys. **98**, 2319 (1993).

[138] B. Löhle and R. Klein, Physica A **235**, 224 (1997).

[139] K. J. Naidoo and J. Schnitker, J. Chem. Phys. **100**, 3114 (1994).

[140] G. P. Hoffmann and H. Löwen, J. Phys.: Condens. Matter **12**, 7359 (2000).

[141] H. Löwen, J. P. Hansen, and J. N. Roux, Phys. Rev. A **44**, 1169 (1991).

[142] D. L. Ermak, J. Chem. Phys **62**, 4189 (1975).

[143] H. Löwen and G. Szamel, J. Phys. Condens. Matter **5**, 2295 (1993).

[144] H. Löwen, T. Palberg, and R. Simon, Phys. Rev. Lett. **70**, 1577 (1993).

[145] F. Bitzera, T. Palberg, H. Löwen, R. Simon, and P. Leiderer, Phys. Rev. E **50**, 2821 (1994).

[146] D. M. Heyes and A. C. Branka, Phys. Rev. E **50**, 2377 (1994).

[147] S. R. Rastogi, N. J. Wagner, and S. R. Lustig, J. Chem. Phys. **104**, 9234 (1996).

[148] J. Bergenholtz and N. J. Wagner, Physica A **235**, 34 (1997).

[149] W. Härtl, J. Wagner, C. Beck, F. Gierschner, and R. Hempelmann, J. Phys.: Condens. Matter **12**, A287 (2000).

[150] A. J. Banchio, G. Nägele, and J. Bergenholtz, J. Chem. Phys. **113**, 3381 (2000).

[151] J. Dzubiella and H. Löwen, J. Phys.: Condens. Matter **14**, 9383-9395 (2002).

[152] S. B. Santra, S. Schwarzer, and H. Herrmann, Phys. Rev. E **54**, 5066 (1996).

[153] J. Dzubiella, G. P. Hoffmann, and H. Löwen, Phys. Rev. E **65**, 021402 (2002).

[154] M. Heni and H. Löwen, Phys. Rev. Lett. **85**, 3668 (2000).

[155] M. Heni and H. Löwen, J. Phys.: Condens. Matter **13**, 4675 (2001).

[156] A. Imhof, A. van Blaaderen, and J. K. G. Dhont, Langmuir **10**, 3477 (1994).

[157] T. Palberg and M. Würth, J. Phys. I (France) **6**, 237 (1996).

[158] A. Onuki, J. Phys.: Condens. Matter **9**, 6119 (1997).

[159] R. Lahiri and S. Ramaswamy, Phys. Rev. Lett. **73**, 1043 (1994).

[160] R. Lahiri and S. Ramaswamy, Physica A **224**, 84 (1996).

[161] M. C. Newstein, H. Wang, N. P. Balsara, A. A. Lefebvre, Y. Shnidman, H. Watanabe, K. Osaki, T. Shikita, H. Niwa, and Y. Morishima, J. Chem. Phys. **111**, 4827 (1999).

[162] A. Jusufi, J. Dzubiella, C. N. Likos, C. von Ferber, and H. Löwen, J. Phys.: Condens. Matt. **13**, 6177 (2001).

[163] F. Mantegazza, V. Degiorgio, A. V. Delgado, and F. J. Arroyo, J. Chem. Phys. **109**, 6905 (1998).

[164] P. Wette, H. J. Schope, R. Biehl, and T. Palberg, J. Chem. Phys. **114**, 7556 (2001).

[165] P. N. Segre, F. Liu, P. Umbanhowar, and D. A. Weitz, Nature **409**, 594 (2001).

[166] G. Nägele, Physics Reports **272**, 215 (1996).

[167] J. K. G. Dhont, *An Introduction to Dynamics of Colloids* (Elsevier, Amsterdam, 1996).

[168] A. J. C. Ladd, Physics of Fluids A **5**, 299 (1993).

[169] D. Helbing, P. Molnár, I. J. Farkas, and K. Bolay, Environment and Planning B: Planning and Design **28**, 361 (2001).

[170] D. Helbing, I. J. Farkas, and T. Vicsek, Nature **407**, 487 (2000).

[171] G. J. Kynch, Trans. Faraday Soc. **48**, 166 (1952).

[172] P. Valiveti and D. L. Koch, Applied Scientific Research **58**, 275 (1998).

[173] P. Valiveti and D. L. Koch, Physics of Fluids **11**, 3283 (1999).

[174] R. Burger, F. Concha, K. K. Fjelde, and K. H. Karlsen, Powder Technology **113**, 30 (2000).

[175] P. M. Biesheuvel, H. Verweij, and V. Breedveld, Aiche Journal **47**, 45 (2001).

[176] J. Chakrabarti, J. Dzubiella, and H. Löwen (2002), to be published.

[177] J. Zhou and M. Z. Podowski, Nuclear Engineering and Design **204**, 129 (2001).

[178] K. Oerding and H. K. Janssen, J. Phys. A **28**, 4271 (1995).

[179] J. L. Lebowitz and J. S. Rowlinson, J. Chem. Phys. **41**, 133 (1964).

[180] J. L. Lebowitz, Phys. Rev. **133**, A895 (1964).

[181] N. W. Ashcroft and D. Langreth, Phys. Rev. **156**, 685 (1967), erratum, *ibid.* **166**, 934 (1968).

[182] R. J. Baxter, J. Chem. Phys. **52**, 4559 (1970).

Acknowledgement

First, I would like to express my gratitude to Hartmut Löwen for giving me the opportunity to perform this work and for all his great support and the motivating discussions during the last years.

I am deeply grateful to Christos N. Likos for his excellent guidance, tireless patience and all the things I have been able to learn from him. Not to forget the fun we had together.

I thank Jean-Pierre Hansen for acting as the third referee of this work.

Special thanks go to my longtime officemates Holger M. Harreis and Arben Jusufi for discussions, breaks, entertainment and the best time one could have in an office.

Many thanks to all former and current members of the Theoretical Physics II in Düsseldorf for the nice and stimulating environment and many helpful discussions. Special thanks go to Ansgar Esztermann, Cord Kielhorn and Alexander Schlensog for maintaining the computer systems, in particular our cluster Blob.

I thank Jörg Stellbrink for the nice collaboration and insights to experimental soft matter physics.

Lovingly thanks are dedicated to my girlfriend Kristin for her understanding, help and bringing me back to earth after hours of working. Also many thanks to her parents for their interest and support.

My sincere thanks to my Mother Helga for all her generous support and for the best sunday lunches a mother can cook.

I thank my family and my friends for the good times in-between.

I gratefully acknowledge financial grant from the DFG within the Sonderforschungsbereich 237 and the DAAD within the Doktorandenstipendium.